DESIGN OF DUPLEX LOW CARBON STEELS FOR IMPROVED STRENGTH: WEIGHT APPLICATIONS

Jayoung Koo
(Ph. D. thesis)

August 1977

Prepared for the U. S. Department of Energy
under Contract W-7405-ENG-48

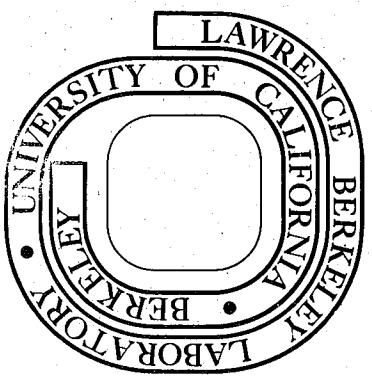

TABLE OF CONTENTS

DESIGN OF DUPLEX LOW CARBON STEELS FOR IMPROVED STRENGTH: WEIGHT APPLICATIONS

Jayoung Koo

Materials and Molecular Research Division, Lawrence Berkeley Laboratory,
and Department of Materials Science and Mineral Engineering
University of California, Berkeley, California 94720

ABSTRACT

Duplex ferrite-martensite (DFM) steels with excellent combinations of strength and formability have been selected from first principles, and their microstructure–property relationships established through a systematic investigation of a series of ternary Fe/X/0.1 C steels (X being varying amount of Cr and Si). Duplex processing consists of initial austenitization and quenching to form 100% martensite, followed by annealing in the $(\alpha+\gamma)$ range and subsequent quenching. The resultant DFM morphology is controlled by the type and amount of alloying element X.

The DFM alloy, of composition Fe/2% Si/0.1% C, which has been developed according to the selection principles showed superior tensile properties to a series of Cr and Mn DFM steels, and to some selective commercial HSLA steels including Van 80. Stress-strain behavior of this new DFM steel include high work hardening rate, smooth transition from elastic to plastic deformation, and high ratio of tensile/yield strength and good elongation to necking. These characteristics are indicative of excellent formability in combination with high strength. The superior

properties found in the 2% Si DFM steel are attributed to the following features; fine, fibrous and discontinuous distribution of martensite particles in a ferrite matrix, optimizing the properties of the constituent phases, and maintaining a high degree of coherency at the α/martensite interfaces.

It is found that the impact properties of the various DFM steels (Fe/X/0.1 C) are strongly influenced by the connectivity, carbon concentration, and volume fraction of martensite. Yield strength is determined by the flow stress of the ferrite, and is not affected by the strength of martensite while ultimate strength is sensitive to the martensite strength.

The effects of the structural parameters on controlling the strength-ductility balance are described, and their role during the deformation process characterized. From this study the origin of the desirable properties found generally in DFM steels is suggested to depend on the following: i) high purity of the ferrite matrix, ii) Both strong and tough martensite as a second phase constituent, iii) Equal elastic constants, and iv) good coherency at the α/martensite interface. Finally, high resolution electron microscopy is presented in the last section, and demonstrates that lattice imaging technique can be successfully applied to phase transformation studies in steels.

I. GENERAL INTRODUCTION

A number of factors have triggered intensive development programs resulting in the introduction of new steel compositions and processing techniques. The need for higher strength steels with good formability in transportation industries to achieve weight reductions and fuel savings as well as today's energy and resource conservation requirements are among the factors generating strong incentives to produce better steels than those in general use at minimum cost penalty.

Pursuant to these increased requirements, the alloy design trends for structural applications have focussed attention on the detailed physical metallurgy of low-carbon, low-alloy steels,[1-3] thus enabling exploitation of their potential strength with adequate ductility. As an outgrowth of this movement, for example, the hot rolled low carbon steels which, in the past, have been able to fill the material requirements for the majority of structural applications are progressively being replaced by high strength, low-alloy (HSLA) steels. The principal strengthening of these HSLA steels is derived from precipitation of finely dispersed alloy carbides and grain refinement.[4] The manufacture of such HSLA steels are, however, associated with some economical problems discussed elsewhere (e.g., ref. 5). Further, their overall mechanical properties are not always satisfactory for many applications (e.g., formability).

The search for an alternative has spurred the recent development of duplex ferritic-martensitic (DFM) steels.[6-14] These are a new class of HSLA steels whose approach to strengthening contrasts markedly

with microalloyed HSLA steels in chemistry as well as processing technique. Interest in the DFM steels has arisen since:

(1). The required composite microstructure can be produced solely by simple heat treatment.

(2) A wide range of attractive strength and ductility combinations are obtainable.

(3) Carbide forming elements as in commercial HSLA steels are not required.

The major source of strengthening in the DFM structure arises from the incorporation of inheritantly strong martensite as a load carrying constituent in a soft ferrite matrix which supplies the system with the essential element of ductility.

Undoubtedly, the occurrence of DFM aggregates is one of the oldest phenomena in the history of martensitic transformation in steels since these mixed microstructures are produced as an unavoidable consequence of incomplete austenitization and/or lack of sufficient hardenability. In this regard, earlier investigators, Carpenter and Robertson[15] (1939), and Herres and Lorig[16] (1945) considered the two phase aggregates to be undersirable microstructural features rather than potential strengthening devices in low carbon steels. The idea of the DFM structures as possible materials of technological interest was first recognized by Cairns and Charles[17] (1967) who produced controlled microstructures of elongated regions of martensite in a ferrite matrix either synthetically or by a combination of cold deformation and rapid reheating. However, this technique suffers from various disadvantages[17] and the resultant

mechanical properties were no better than could be obtained from suitably heat-treated alloy steels. In contrast, Grange[18] utilized the phase transformation occurring in the two phase ($\alpha+\gamma$) range in Fe - C phase diagram to obtain fibrous mixtures of martensite and ferrite in various carbon steels by thermomechanical treatments. Again, the processing technique is complex and only limited success in improving mechanical properties was achieved.

The most attractive aspect of DFM structures that have very recently been developed is the capability of optimizing the ever conflicting property requirements of strength and ductility, contingent upon a favorable choice of alloy composition and processing.[10,19] Apart from these interesting mechanical properties, however, there is a general lack of fundamental understanding of their origin and characteristic behavior of the DFM system. For instance, papers reporting the results of mechanical property tests generally made little direct connection with duplex microstructures, except with the occasional inclusion of an optical micrograph of the DFM alloys.[116,117] This lack of a coherent microstructure–property relationship is due in part to the complexities of the mechanical behavior of the two phase materials as well as the intricate interactions of parameters such as the size, shape, distribution, and volume fraction of martensite particles. These and the other important metallurgical factors must be characterized and controlled in designing improved DFM alloys such that they favorably contribute in concert to the overall mechanical properties.

Therefore, this investigation was undertaken to provide physical insight to the design and characterization of DFM alloys as well as an understanding of the principal strengthening mechanisms involved. The first two parts will be primarily concerned with the selection considerations utilizing the first principles of the microstructure-property relationships. This is aimed to obtain desirable duplex microstructural characteristics that produce improved mechanical properties by simple heat treatment alone. The last part will deal with high resolution electron microscopy (lattice imaging) which was used, in conjunction with conventional TEM, to assist the characterization of the duplex microstructural constituents at the atomic level, and to estimate solute concentration from precise lattice parameter measurements.

II. FUNDAMENTAL CONSIDERATIONS OF THE SELECTION OF TWO PHASE MATERIALS

A. Nature of Two Phase Materials

Most of the modern engineering materials of technological importance are two phase aggregates of great variety. Restricting to the materials relevant to physical metallurgy, i.e., metals, metal composites, and ionic solids, these composite materials can be divided into two categories in terms of the strengthening mechanisms involved and associated manufacturing techniques. One is the fiber reinforced composites and the other is dispersion strengthened materials, both of these containing a second phase which is harder than the matrix.

In the former case, two physically separable materials, i.e., particles or fibers and metal matrix are compounded into an aggregate. Its strengthening mechanism is principally governed by the well established fiber-loading concept.[20,21] On the other hand, the latter alloy is a type of composites in which the second phase particles and matrix are, in most cases, phases of the same component system, and the Orowan mechanism[22] for yielding is operative when the particle size is less than several microns. However, when the size of the second phase is in the range of 1 $\mu \sim 50\mu$, which corresponds to the transition between fiber reinforced strengthening and dispersion hardening, there exists no simple model for a strengthening mechanism that governs the flow property of the alloy.[23,24] This situation involves extreme complications in theoretical analysis such as the particle/particle interactions[25] and stress concentration effects caused by the discontinuity at the particle end.[26] Therefore,

the specific strengthening mechanism governing a two phase material is determined by the size and morphology of the second phase. However, one thing that is common in the nature of two phase materials is the way in which the second phase particles enhance the strength of the composite system, i.e. they exert constraints upon the matrix. Accordingly, upon deformation, the material in their neighborhood is restricted from elongating freely, resulting in an increase in shear stresses to proceed further deformation. Thus the characteristic mechanical behavior of the composite include early and fairly extreme work hardening rates which suppress mechanical instability as well as a considerably greater flow stress than that of the pure matrix. While the better engineering properties of the strong particles are utilized in this way, the effect of some of their less desirable features, such as brittleness, is simultaneously mitigated by the presence of a ductile matrix that binds the particles together.

It is important to emphasize that the strengthening mechanisms by which plastic deformation of a composite occurs, and the way in which its special features are exploited to achieve the best balance of strength and ductibility, depend on the specific system under consideration. In what follows, we will consider the two phase mixture rule and selection guidelines for a two-phase system with particular reference to DFM steels.

B. Two Phase Mixture Rule

Most experiments and theoretical analyses have been performed in composites containing either unidirectionally aligned fibers or very finely dispersed particles. Thus the understanding of the principles and practical utilizations of these two well defined composites have been fairly well established, and comprehensive reviews on the subject appear in the literature.[20,23,27-29] In the case of randomly oriented coarse two phase structures, however, current understanding of their mechanical behavior is far from complete.[30] Duplex structures of this kind occur in many technologically important alloys, and thus have received much attention in the past. As a result, much data concerning their mechanical properties has been reported in the literature.[6,10,24,31-33] Much of the empirical evidence accumulated to date suggests that, in spite of the absence of an exact theoretical explanation, the strengthening of the duplex alloys can be predicted with reasonable accuracy by the mixture rule of the form[6,10,31-33]

$$\sigma_c = \sigma_f V_f + \sigma_m (1-V_f) \qquad (1)$$

where the subscripts c, f, m refer to composite, second phase particles and matrix, V_f is the particle volume fraction, σ_f is the ultimate tensile strength of the particles, and σ_m is the stress carried by the matrix when the composite is strained to its ultimate tensile stress. In a strict sense, the equation (1) holds only for describing the mechanical behavior of unidirectionally aligned, continuous fiber composites assuming that the fibers and matrix are well bonded and the fiber strain,

matrix strain and composite strain are all equal.

C. Selection Principles

In adding second phase particles to ductile matrices, ductility is usually sacrificed for strength. The implication of the mixture rule is that the loss of ductility is proportional to the volume fraction (V_f). However, one can imagine many duplex distribution of martensite particles that, when properly spaced in the DFM alloys, will result in not only strengthening but also leading to minimizing loss in ductility. This goal can be achieved by proper control of parameters such as the size, shape, and distribution of the martensite particles, and the properties of the individual phases. The following guidelines for developing desirable DFM structures are thus suggested:

(1) Optimum volume fraction: The volume fraction (V_f) of the martensite particles plays a major role in the control of mechanical properties of DFM alloys. V_f must exceed the lower limit below which substantial contribution to strengthening does not occur. At the same time V_f must be less than the upper limit beyond which the failure of the particles immediately leads to the failure of the duplex structure. In other words, if the fracture of one particle occurs at some weak point, it will cause stress to be transferred back to the matrix near the particle break. This local stress intensification will cause other particles to fracture in the same cross section.[34] This process may be eliminated if V_f is in the optimum range so that the matrix can work harden locally and carries

the transferred load. In addition, the alloy system must be chosen such that a slight temperature variation during heat treatment should not significantly alter V_f so as to ensure reproducibility of the materials.

(2) Size and shape factors: Finer scale of the substructure and fibrous particles are desirable. If martensite particles are sufficiently small (on the order of a μ or less), and if the spacing of the particles is such that the yield of the matrix is controlled by the micromechanistic model instead of a fiber loading concept, then an increased yield stress of the matrix coupled with an increased rate of work hardening is expected to be observed.[35-36] With regard to shape factors, load transfer is most efficient when particles are present in the form of fibers rather than spheres. This is primarily because the transfer of load occurs by shear action along the particle/matrix interfaces[34] and, for a given volume fraction and the same number of particles, more interfacial area is available in the case of a fibrous morphology.

(3) Distribution: Discontinuous particles in a continuous matrix. Practical considerations argue that unidirectionally aligned martnesite particles throughout a ferrite matrix can not be produced by simple heat treatment alone. It is more likely that a mixture of macroscopically randomly oriented DFM structure will be obtained, thus resulting in isotropic mechanical properties. This is desirable in a sense that for most engineering materials at least partial isotropy will be required. DFM structures where the particles are connected throughout the matrix should be avoided since they will be directly loaded at their ends. This will

cause the particles to break in the early stage of plastic deformation and prevent the ferrite from contributing its full ductility.

(4) Carbon content: Must be kept sufficiently low. Inherently strong martensite is a diffusionless transformation product of carbon enriched austenite. Hence, the average carbon content in the initial alloy should be kept sufficiently low to maintain a carbon level of about 0.3 pct. in austensite, resulting in dislocated martensite. The higher carbon content can drastically deteriorate the toughness of martensite.[37]

(5) Microstructural features: Undersirable carbides should be avoided. As aforementioned, stress in the continuous matrix is transferred to strong particles by the shear action at the particle/matrix interface. As a consequence, the nature of the interface and nearby microstructural features are of critical importance.[38] Since the composition of DFM alloy under consideration is essentially low carbon and low alloy, the resultant lack of sufficient hardenability may cause a pearlitic reaction with Fe_3C formed during quenching from γ to martensite. These carbides, if any, will be located near the interface where stress concentrations can originate formation of cracks within the carbides, eventually leading to complete failure of the specimen.

(6) Nature of interfaces: High degree of coherency. A high energy interface is more likely to fail under stress than a low energy one, since the interfacial energy can supply some of the work of separation of particle from the matrix. Ideally, therefore, the martensite/ferrite interface should have good atomic fit.

D. Processing and Choice of Alloying Elements

The considerations above suggest desirable microstructural characteristics of a DFM steel that is both strong and ductile. The most difficult challenge will be to produce DFM steels with these considerations for a sufficiently small cost premium to make them economically competitive. As is quite common practice in designing alloys, we start with simple ternary Fe/X/C alloys prior to advancing to a more complex system. The success achieved will then depend largely on a favorable choice of an substitutional alloying element, X, and processing.

Processing:

The production of the controlled amount of martensite in a ferrite matrix can be done using many different heat treatments (e.g., Fig. 1), all of which involve phase transformation in the $(\alpha+\gamma)$ region. Choice of the specific heat treatment will be dependent on the alloy composition, property requirements, and production capabilities.

Of particular interest is the intermediate quenching treatment (Fig. 1a) of which details are described in section III-B-2. The treatment was developed so as to fully exploit the characteristic nature of the initial martensite structure prior to subsequent annealing in the $(\alpha+\gamma)$ range: i.e., (i) it provides sufficient heterogeneous nucleation sites for austenite (martensite at room temperature) during two phase annealing, and (ii) parallel laths of extremely small width within a prior austenite grain can be utilized to produce a fine, fibrous distribution of martensite in a ferrite matrix. Moreover, these advantages allow ease of control of the size, distribution, and shape of the martensite particles depending

on the amount of type of the alloying element X.

Alloying Elements

Metallurgical knowledge accumulated to date on the behavior of alloying elements suggest that silicon is one of those which most favorably controls the design parameters of interest here, e.g.,

(1) Silicon broadens the $(\alpha+\gamma)$ range[39] when added to Fe-C system, thereby facilitating practical control of the martensite volume fraction.

(2) Promotion of a fine, fibrous distribution of martensite in a continuous ferrite matrix.[40]

(3) Improvement of the α/martensite interface by inhibiting the formation of coarse carbides during the final quench.[41]

(4) Provision of very effective solid solution strengthening in the ferrite.

(5) Low cost and availability.

In addition to the choice of silicon as an substitutional alloying element, toughness of martensite requires that carbon content of a Fe/X/C alloy be about 0.1 wt. pct. so as to produce dislocated martensite in the DFM alloys with 20 ~ 60 pct. volume fraction of martensite.

III. STRUCTURE AND MECHANICAL PROPERTIES OF DUPLEX Fe/X/0.1 C ALLOYS

A. INTRODUCTION

The selection considerations in the preceding section outline the principles involved in the development of DFM steels. The composition, Fe/Si/0.1 C, and duplex treatment were chosen so as to produce desirable DFM structures which in turn will result in desirable mechanical properties. The DFM Fe/Si/C alloys have also been studied independently by Nakaoka et al.[117,118] However, the published works do not appear to take into account the desirable macro- and microstructural morphologies. This section will establish the duplex microstructure-property relationships with particular emphasis on a fundamental understanding of its mechanical behavior. For this purpose and also to assist in testing the validity of the design principles, a series of Fe/Cr/0.1 C steels were also investigated for comparison with the structure and mechanical properties of silicon containing DFM steels.

B. EXPERIMENTAL PROCEDURE

1. Material Preparation

The materials used in this investigation were received in the forms of hot forged round bars and plates. The composition of alloys are listed in Table I. The steel alloys were prepared and provided by Daido Steel Company, courtesy of Dr. Asada. The alloys were melted in a vacuum

induction furnace. The ingots were then forged at 1000 ~ 1100° C into 15 mm diam. rods and 25 mm × 65 mm plates. They were sand-blasted, homogenized at 1200° C in vacuum for 20 hours and subsequently furnace-cooled. Chemical analysis was done for several elements before and after homogenization. Except some loss in carbon (of about 0.05 wt. pct.), there was no loss of any other elements. The carbon contents given in Table I were measured after homogenization. Otherwise, the results of the chemical analysis were virtually the same as those given by the supplier. Round tensile and Charpy impact specimens were obtained from the homogenized rods and plates, respectively. The orientation of the Charpy impact specimens with respect to the long direction of the plate is shown in Fig. 2a.

2. Heat Treatment

The heat treatment to produce controlled DFM structures consists of austenitizing and quenching to 100 pct. martensite, followed by annealing in the ($\alpha + \gamma$) range as shown in Fig. 3. By holding in the two phase range, martensite transforms partially to austenite and the residual martensite becomes ferrite as the two phases attain the composition specified by the tie line corresponding to the holding temperature. The alloy will then consists of low carbon ferrite (α) and higher carbon austenite (γ). Upon quenching, the austenite transform to martensite (strong phase), and the ferrite becomes heavily dislocated due to plastic deformation as a result of the austenite → martensite transformation strain. This structure has been confirmed by transmission electron microscopy (see Fig. 19).

The heat treatment was done so as to control the morphology of the duplex microstructural constituent, which is strongly influenced by the substitutional solute (X), as will be shown later. The heat treatment, hereforth described as "intermediate quenching treatment" or "duplex treatment", offers a wide range of possible martensite volume fractions depending on the annealing temperature and time in the ($\alpha + \gamma$) range, for a given alloy composition.

Austenitization and two phase annealing of round tensile blanks, oversize Charpy impact specimens and TEM specimens were done under an argon atmosphere. Austenitizing treatments for Cr and Si steels were performed at 1100° C and 1150° C for 1 hour respectively, and suitable holding time in the ($\alpha + \gamma$) range was determined to be 20 min. for all the specimens. After heat treatment in each step, the specimens were quenched into agitated iced brine or, in a few instances, they were water quenched. Tempering of fully martensitic, and selective duplex alloys was accomplished by immersion in a neutral salt bath kept at a desired temperature, i.e., 200° C, 400° C, and 600° C. The temperature was controlled within ±5° C. All specimens were directly water quenced from the tempering temperature.

3. Mechanical Testing

(i) Tensile Tests

Tensile properties were determined using the 1 in. gage round tensile specimens, following ASTM specification.[113] Two inch gage round specimens were also used only when comparison with the tensile properties of commercial steels was made. Tensile tests were performed at room

temperature in an Instron machine with a cross-head speed of 0.05 cm/min and full scale load of 1000 Kg. During testing, uniform elongation was continuously monitored by measuring the distance between two fixed points using an optical magnifier. This method has proven to be more accurate than that using the extensometer whose output is fed into the chart drive system of the Instron control console. Measurements of each gage section before and after testing were accurately determined using an optical microscope equipped with a Vernier translating stage calibrated to 0.001 in. The values of tensile properties reported are averages of at least three tests.

(ii) Charpy Impact Testing

The standard and 3/4 subsize Charpy V-notch specimens[114] were used for the Charpy tests. The impact tests were conducted on a Universal Impact Machine with a 120 ft-lb capacity. Low temperature tests were performed following the ASTM-23-72 specifications.[114] Zero and sub-zero temperatures were controlled within ±3° C using mixtrues of ethyl alchol and dry ice.

4. Phase Transformation Measurements

To roughly assess the ranges of the $(\alpha+\gamma)$ and γ phase fields, dilatometric methods were used, and γ start temperature, A_s and γ finish temperature, A_f, were determined. A sketch of the specimens used is given in Fig. 2b. The heating rate employed in this study was approximately 10° C/sec and was controlled using a programmable temperature controller.

The specimen's quenching rate was controlled using a Datatrek program whereby the M_s and M_f temperatures were thus determined.

5. Microscopy

(i) Optical Metallography

Samples for optical metallography were cut from tested tensile and impact specimens. They were mounted in coldmount and ground on successively finer papers 0 to 600 grit and then polished on a one micron diamond abrasive wheel lubricated with kerosene. In these metallogrphic investigations the standard etchants, 2% nital and 5% nital, were used to reveal the duplex microstructural constituents. The volume percent of martensite particles was determined by standard quantitative metallography using the linear intercept method.[115]

(ii) Transmission Electron Microscopy

The alloys used in this investigation have limited hardenability due to the low carbon content. Consequently, samples of different thickness may result in different microstructures, particularly in the amount of diffusional products that could be produced during the final quenching operation. In order to characterize the true microstructure in the test specimens, precaution was taken to ensure that the samples for the thin foils had the same thickness as the round tensile and impact specimens, and were subjected simultaneously to the same heat treatment.

Slices about 0.025 in. thick were cut from the heat treated samples. Flood cooling was employed to minimize specimen heating during cutting. The specimens were then chemically thinned to about 5 mils thick in H_2O_2 containing 2% HF at room temperature. Final thinning was done in a twin-jet polishing apparatus using a chromic-acetic acid solution (75 C_rO_3 + 400 ml CH_2COOH + 21 ml H_2O). The resultant foils were examined in a Siemens Elmiskop IA and a Phillips 301 transmission electron microscope at an acceleration voltage of 100 KV.

(iii) Scanning Electron Microscopy

The fracture morphology of tensile and Charpy specimens was thoroughly documented using an AMR-1000 scanning electron microscope operated at 20 KV. Fracture surfaces selected for examination were taped to prevent any mechanical damage and contamination by foreign particles, then stored in dessicators until examined in the SEM.

C. RESULTS

1. Transformation Temperatures

Table I lists the measured A_s, A_f, M_s, and M_f. The temperature intervals between A_s and A_f allow a rough assessment of the phase range in the $(\alpha+\gamma)$ field. Consequently, the results of the transformation temperature show that Si opens up the $(\alpha+\gamma)$ range while Cr contracts it. These findings are in agreement with the pseudo binary Fe/Si/C[39,42] and Fe/Cr/C[43] phase diagrams reported in the literature.

Extensive isothermal experiments were conducted to determine the A_3 temperature, solution treatment temperature, and the two phase annealing temperatures for each alloy. Based on optical metallography, the austenization temperature was determined to be 1150° C for Si containing steels and 1100° C for Cr bearing steels to attain similar initial γ grain sizes. Table II shows the results of the annealing temperatures in the $(\alpha + \gamma)$ range corresponding to the respective volume fraction of martensite. The annealing time in the two phase range was determined to be 20 minutes. This time reflects the efforts of optimizing reproducibility and minimizing grain growth.

2. Characterization of Duplex Ferritic-Martensitic Structures

Extensive metallographic examinations of duplex treated steels have been conducted to determine whether any rationale can be developed in order to characterize the duplex microstructures, correlate the duplex structure with mechanical properties, and to explain the influence of alloying elements on the morphology of the duplex constituents. The results of the metallographic studies are summarized in this section.

(i) Optical metallography

Marked differences are developed in the morphology of the DFM structures depending on the amount and type of alloying element X present in the Fe/X/0.1 C ternary system. (Hereafter, "0.1 C" represents the carbon content in each alloy). These are illustrated in the optical micrographs Figs. 4 through 7.

Fe/Cr/0.1 C steels

The initial martensite structure obtained by quenching after solution treatment is shown in Fig. 4a. It is evident that no other decomposed products of austenite are present in the microstructure. The average grain size of all the Cr steels is about 410 μ. Upon annealing of the initial microstructure in the ($\alpha + \gamma$) region, the Cr content present begins to effect the phase transformation behavior significantly.

Figure 5 shows the DFM structures developed in a 0.5 Cr steel. The areas of grey contrast correspond to martensite embedded in a light background which is ferrite. As can be seen in the figure, martensite particles exhibit a continuous network along the prior γ grain boundaries with an acicular morphology in the interior of the prior γ grains. This clearly indicates that during annealing in the ($\alpha + \gamma$) region, formation of austenite from the initial martensitic structure begins at the prior γ grain boundaries and, also, at the martensite lath boundaries. The austenite* formed at prior γ grain boundaries adopted a mixture of grain boundary allotriomorphs and idiomorphs. Allotriomorphs are particles which nucleate at the grain boundary in the matrix phase and grow preferentially and more or less smoothly along them.[44] Idiomorphs are particles which nucleate at the grain boundary in the matrix phase and grow randomly with no preference in specific direction. In contrast, the interiors of the γ grains were predominantly martensite lath boundary allotriomorphs mixed with a few scattered intragranular idiomorphs.

*The austenite formed from the initial martensite structure during two phase annealing will, of course, transform to martensite again upon quenching. For the convenience of presentation, the transformation product is described as "austenite".

However, as the Cr content was raised a remarkable difference in the morphology of γ formed from martensite was observed. This is shown in Fig. 6 obtained from the 4% Cr duplex alloy. Here, the globular shape of martensite particles not only delineates the prior γ grain boundary, but displays the principal morphology in the interior of the γ grains as well. The intragranular austenite particles develop in such a manner that once they nucleate and grow to a critical size along the martensite lath boundaries they rapidly spherodize to form globular shapes.

The intermediate nature of the above two distinct DFM morphologies was observed in the duplex 2% Cr steels. The common feature of all Cr containing DFM structures is the decorated appearance of the connected martensite particles at the prior austenite grain boundaries. This feature is not present in the case of Si DFM steel as described below.

Fe/Si/0.1 C steels

Figure 4b portrays the as-quenched initial martensitic structure obtained from Si bearing alloy. Again, the microstructure was completely martensitic without any evidence of proeutectoid ferrite which may have been produced during quenching. The average grain size was about 270 μ, slightly smaller than that of the Fe/Cr/C steels. The general features observed in this steel were similar to those observed in the Cr containing alloys. Upon subjecting to annealing in the $(\alpha+\gamma)$ region, however a completely needle-like morphology was adopted for the formation of γ from the martensitic structure. Direct quenching to room temperature transformed the γ to martensite resulting in the fibrous DFM structure as shown in Fig. 7. It is seen that the influence of the

initial martensitic structure is still clearly reflected in the fine, acicular morphology of the martensite particles. Evidently, these needle-like particles nucleate and grow along martensite lath boundaries.

An important observation is that the nucleation and growth of γ particles are absent along the prior austenite grain boundaries. This is rather surprising from the view point of classical nucleation and growth theory[45] through which preferential nucleation process at the grain boundary is recognized. A plausible explanation for this unusual situation will be presented in the discussion section.

Unlike the case with Cr steels, the geometrical features of the Si DFM structure remain largely unchanged as the Si content is varied, except for the presence of coarse carbides which can only be resolved in transmission electron microscopy as will be shown later.

(ii) Transmission Electron Microscopy

The various ferrite, martensite and carbide morphologies together with their substructural features and interface characteristics encountered with duplex processing were examined using transmission electron microscopy. Unfortunately, there presently exists little information in the literature on the microstructural detail of DFM steels. Therefore, the characterization of the duplex microstructural constitutuents by TEM is needed and is carefully documented in this section.

a. Initial Martensite Structures

The morphology and substructures of the various low carbon steels in this investigation with 100% martensite are shown in Figs. 8-13. The microstructure consisted of almost entirely of dislocated laths of the

order of 0.1 μ ~ 1μ wide with an extremely small amount of transformation twinning present; typical of low carbon martensitic steels. A prominent feature of the martensite in all the alloys was the existence of retained austenite that was trapped between the growing martensite laths in the form of narrow thin films. The morphology of the high temperature phase that has been stabilized at room temperature is illustrated in Figs. 8-10. There was no observable difference in the extent and distribution of the retained austenite in all the specimens observed. In order to unambiguously identify the presence of retained austenite, appropriate precaution[37] has been taken and the possible complexities that may arise from such intervening factors as double diffraction, carbide, twinning and their combinations were fully accounted for. Figure 8d shows the crystallographic relation between austenite and martensite, which exhibits the Kurdjumov-Sachs orientation relationship, $\langle 111 \rangle_\alpha / \langle 110 \rangle_\gamma$. In most cases the K-S relationship dominated the crystallographic orientation relationship between BCC and FCC in this study, which confirms the previous observations that have been made on various carbon steels.[37,46] Occasionally, however, another orientation relationship, shown in Fig. 10, was observed. Indexing of the selected area diffraction pattern (Fig. 10d) indicates that the crystallographic relation is close to the N-W relationship which is 9° away from the K-S.[47]

Another characteristic feature of the fully martensitic structures was the occurrence of extensive autotempering. Such autotempered carbides were present in all the alloys except alloy 4, and are shown in Figs. 11-13. Most of the carbides were cementite in a typical {110}

Widmanstatten orientation. The density of the autotempered carbides was much reduced in the alloy 4 (Fig. 13) presumably due to the role of Si on inhibiting the precipitation of carbides—especially cementite.[48]

It should be emphasized that the type of initial microstructure prior to duplex processing is of prime importance in determining the morphology of DFM structures since, upon reheating to the two phase region, the nucleation and growth of austenite from the initial structure is strongly influenced by their microstructural details. Therefore, the foregoing characterization of the initial martensitic structures will be useful as it is related to the subsequent transformation behavior during duplex treatement. This will be shown later in the discussion.

b. Morphology of Duplex Microstructural Constituents

Upon subjecting to annealing in the ($\alpha + \gamma$) range, the initially homogeneous distribution of carbon atoms in the martensite segregates into carbon enriched particles (γ) leaving carbon depleted regions (α) behind. The relative proportion of each phase depends on the tie line specified by the annealing temperature. Individual components of the final product after quenching from the two phase region underwent complicated transformation processes which are separately described below.

Morphology of Martensite

The morphology of the martensite in all the DFM structures was similar to the corresponding fully martensitic structures, while its substructure exhibited a higher density of twinning compared to that in the initial martensite. Although quantitative measurements regarding the amount of transformation twinning was not attempted, it was noted that

the amount of twinning increased with a decreasing volume fraction of martensite for a given annealing time in the ($\alpha+\gamma$) region. Of course this result is to be expected since the lower the volume fraction of martensite, the higher the carbon content in the martensite according to the tie line in the phase diagram. In addition, it is well established that the carbon plays the key role in determining the type of martensite substructure (dislocated or twinned martensite).

Figure 14a shows the typical twinned area in the Cr DFM steels with about 20% martensite. Dark field imaging of a twin spot superimposed with a matrix spot is shown in Fig. 14b. The increased twinning tendency with decreased volume fraction of martensite was also observed in Si DFM steels. Figure 15a illustrates the microtwins at relatively high magnification obtained from the 2% Si DFM steel having approximately 20% martensite. The imaging of a twin reflection reversed the contrast in the dark field (Fig. 15b). In most cases, they were internal microtwins embedded in the dislocated martensite.

Apart from the varying quantity of transformation twinning, the other significant features of the martensite were similar to those observed in the fully martensitic structures. For instance, there was no observable difference in the extent and distribution of the stabilized phase among the alloys. A general feature the retained austenite portrayed was a non-uniform distribution throughout the microstructures; in some areas, no evidence of retained austenite was present even with extensive tilting and favorable orientations. The retained austenite, even in extremely small quantities, may be favorable to prevent transfer of cracks from one particle to another.

Autotempering was another prominent feature of the martensite in all DFM alloys except alloy 4. Figure 16a shows the example of the autotempered carbides obtained from DFM alloy 2. The corresponding dark field image of the carbides is shown in Fig. 16b, where the matrix is also shown since a superimposed spot was imaged. The other areas showing extensive autotempered carbides are illustrated in Fig. 17. The carbides were identified as cementite.

In summary, the morphology and substructure of the martensite as a constituent of DFM structures are similar to those of fully martensitic structures, except for the extent of transformation twinning which increased with decreasing volume fraction of martensite. Twinning, extensive autotempering, and small quantity of retained austenite were the main substructural features in the predominantly dislocated martensite.

Morphology of Ferrite

The morphology of the ferrite was similar in all the DFM structures, and its significant features were associated with fine subgrain size and high dislocation density, as shown in Figs. 18-19.

The ferrite is the matrix phase which does not undergo structural transformation during heat treatment in the $(\alpha + \gamma)$ region. During the annealing process, a high density of dislocations (order of 10^{12}) is inherited from the initial martensitic structure which undergoes recovery, recrystallization and grain growth. The result is a fine subgrain distribution in the ferrite areas. In addition subsequent quenching from the two phase field results in the generation of a high density of fresh dislocations in the ferrite region due to the accommodation strain caused by

the $\gamma \rightarrow$ martensite transformation. The above observations were evidenced by the isolated experiments on the air cooled structures. The ferrite grain size varied from $\sim 1\,\mu$ to $\sim 5\,\mu$ in all the duplex systems observed. According to the Fe-C phase diagram,[43] the solubility of carbon in the proeutectoid ferrite at 850°C ($\sim$ 50% martensite) is approximately 100 times greater than that at room temperature. Therefore, quenching from the two phase annealing temperature results in the high supersaturation of carbon atoms in the ferrite. Nevertheless, the ferrite region was very clean and free from any detectable precipitation except for extremely limited areas. This observation indicates that the excess carbon in the ferrite at room temperature was probably segregated to lattice defects since most of these sites have a lower energy than those available at the precipitates.[50-52] Consequently there is little driving force for precipitation in the ferrite.

Nature of Interfaces

Since the alloys used in this investigation are primarily low carbon, low-alloy steels, the pearlitic hardenability in particular will be poor. As a consequence, it is likely that in some alloys the precipitation of (α + carbides) according to the $\gamma \rightarrow \alpha$ + carbides reaction can take place during the final quench. In this way these carbides will be located only in the immediate vicinity of the α/martensite interfaces. The morphology of the carbides is shown in Figs. 20, 21. This type of structure was only observed in the alloys 2 and 5, and was similar to that previously observed in 1010 steel.[9] Therefore, for convenience of representation, it is reproduced in Fig. 20. The carbides adopted both

a fibrous morphology in which the prior γ/α interfaces (Fig. 20d) are heavily faceted, and an interface precipitation morphology (Fig. 20C) where the interfaces are largely smooth. These types of carbides have been recognized as a new eutectoid transformation product in a variety of steels.[53-56] Due to the complexities of the carbide diffraction spots, the carbides could not be uniquely identified. Most likely, however, they are of M_7C_6 type according to the suggestion reported by Campbell and Honeycombe.[54]

It was interesting to note that the amount of such carbides decreased with increasing volume fraction of martensite, eventually leading to their absence in the 100% martensitic structure.

There was no indication of such carbide precipitation in alloys 1, 4 and 5, as is seen in Figs. 17 and 19. Their absence in the alloys 1 and 5 is due to the sufficient hardenability for the thickness of the specimens (0.4") used in this investigation. However, in the case of alloy 4 the role of Si as a carbide precipitation inhibitor is more likely responsible for the result rather than through hardenability since Si has only a mild effect on increasing hardenability.[57]

Of particular interest is the nature of the interfaces: whether they are high energy boundary or low energy boundary. Lattice fringe imaging revealed the atomic environments across the interface (Fig. 57) and illustrated good coherency.

c. Tempering of DFM Structures

TEM studies of the tempered DFM structures were mainly concentrated on alloys 2 and 4 since these two DFM alloys are considered to represent the Cr and Si steels, respectively, in view of their documented transformation behavior noted thus far. For both steels, a martensite volume fraction of about 30% was chosen, (i) for convenience of carrying out TEM experiment, and (ii) because the specific volume fraction falls within the range of interest in terms of mechanical properties.

DFM Structures Tempered at 200° C

Tempering at 200° C for an hour resulted in remarkedly different responses in the ferrite and martensite. The ferrite regions which were free from any precipitation in the as-quenched conditions are now associated with carbide precipitation, while the martensite component retained essentially the same morphology as it had before tempering. Such changes encountered in each phases are illustrated in Figs. 22 through 26. As is seen in Figs. 22 and 23 obtained from the 0.5% Cr and 2% Si DFM steels respectively, the coarse carbides, ~ 170 Å wide and ~ 1500 Å long, precipitated in the ferrite were identified as cementite (Fe_3C) by means of indexing diffraction patterns as well as trace analysis. These carbides were not very dense and showed fairly uneven distribution. The other areas in the ferrite where these coarse carbides were not present showed finely dispersed precipitation on dislocation networks, at the nodes of intersecting dislocations and at sub-boundaries, as displayed in Fig. 24 and 25 taken from the 0.5% Cr and 2% Si DFM steels, respectively. The bright field images (Figs. 24a and 25a) of the areas of interest do not

clearly resolve the fine precipitates on dislocations due to the over-spreading dislocation image width.

However, weak beam images of the same area results in greatly improved resolution of heterogeneous precipitates on dislocations, demonstrating the great advantage of weak-beam-technique[58,59] over conventional bright field imaging in this particular application. These are shown in Figs. 24b and 25b taken by using (g, 3g) weak beam imaging condition.

On the other hand, martensite regions remained largely unchanged at this stage as shown in Fig. 26 obtained from the 2% Si DFM steel. It seems that the cementite precipitates observed in the specimens after 200° C tempering were those autotempered carbides that persisted to this temperature without apparent coarsening or shrinking. This is because there was no observable difference in the average size and density of the precipitates as well as no indication of ε carbide precipitation after tempering at 200° C.

DFM Structures Tempered at 400° C

Tempering at 400° C was accompanied by significant changes in both constituent phases, as shown in Figs. 27-29. At this higher tempering temperature, the ferrite matrix was entirely free from the coarse carbides that were present after 200° C tempering, while still showing a fine scale precipitation on those heterogeneous nucleation sites (Fig. 27). However, the dislocation density was not much reduced. Again, weak beam image in Fig. 27b yields better resolution of the fine precipitates on dislocations as compared to the corresponding b.f. image (Fig. 27a). Figure 28 is a transmission electron micrograph obtained from steel 2 at 400° C,

showing tempered martensite in contact with the matrix ferrite along the interfaces. A dark field image obtained by using a carbide reflection in selected area diffraction reversed carbide contrast, and is shown in Fig. 28b. The indexed diffraction pattern identifies the carbides as cementite. The rod-like autotempered carbides that existed in the martensite tempered at 200°C disappeared.

Recovery, carbide growth, and agglomeration have reduced some of the internal strains, resulting in somewhat decreased dislocation density. The first evidence of spheroidal carbide precipitate is also seen at this point. A similar morphology of carbides was observed in steel 4 subjected to 400°C tempering, as shown in Fig. 29. In both steels, the carbides were preferentially distributed along the martensite/ferrite interfaces and lath boundaries. Evidently, precipitation and coarsening of the cementite begins with attendant dissolving of the coarse carbides present in the ferrite. In summary, reduced dislocation density in both phases, resolution of coarse cementite in the ferrite, and precipitation and coarsening of cementite in the martensite characterize the 400°C tempered structures of both steels.

DFM Structures Tempered at 600°C

After tempering at 600°C for an hour, martensite regions transformed to a completely recrystallized ferrite structure with irregularly spaced globules of cementite, while ferrite regions further reduced their dislocation density. Typical micrographs are shown in Figs. 30 and 31.

Figures 30a and 31a are the bright field micrographs obtained from steels 2 and 4 respectively, and the corresponding dark field images of the carbides taken from a carbide reflection are shown in Figs. 30b and 31b. It is seen that the coarsened and spheroidized carbides are located preferentially along α/previous martensite interfaces with some of them along the recrystallized subgrain boundaries within the prior martensite islands.

The large globular carbides of ~0.1μ in diameter were found to be cementite as evidenced by analysis of the electron diffraction patterns (Fig. 30d). The possibilities of the presence of other types of carbides e.g., M_7C_3 and $M_{23}C_6$ was precluded by means of indexing many SAD patterns obtained from the areas containing carbide particles. At this stage of tempering, the tempering process in the ferrite regions involves annealing out of dislocations resulting in extremely low density of dislocations, and coalescence of subboundaries causing large subgrain sizes, as seen in Fig. 32. It is apparent from the figures that the dislocations either at the subboundaries or at the interiors of the subgrains are no longer associated with the fine dispersion of particles that have been present in the structures up to 400°C tempering.

An important observation was that there was no observable difference in the kinetics of tempering processes between two steels in the temperature range of 200°C ~ 600°C. Moreover, of special interest was precipitation of cementite in Si steels even at the 200°C tempering temperature.

3. Mechanical Properties

(a) Tensile Properties

As already mentioned, tensile properties were tested using 1 in. and 2 in. gauge length on round tensile specimens, the latter only for comparison with property specifications of selective commercial HSLA steels. For the 1 in. gauge length specimens, the total elongation was measured on a 1-1/4" gauge length in order to obtain as many data points as possible.

The room temperature tensile test data of the as-quenched DFM steels are summarized in Table III, and are plotted in Figs. 33 through 37. Figure 33 shows the variation of yield and tensile strengths of the steels as a function of martensite volume fraction. The general trend shown in the figure is that the composite strength obeys the rule of two phase mixtures in the range of 15~80 pct. volume fraction of martensite, irregardless of its composition and morphology. The variations of uniform and total elongations with respect to pct. martensite are plotted in Fig. 34, demonstrating the validity of the two phase mixture rule for elongation[60] in the range of 10~80% martensite.

From these plots of strengths and elongation vs pct. martensite, one notes that Si-containing DFM steels show better tensile properties than Cr-bearing DFM steels. In particular, the 2% Si DFM steels exhibit a superior combination of strength and elongation over a wide range of pct. martensite. This is best illustrated in the plot of strength against uniform elongation as shown in Fig. 35, where the tensile properties of commercial Van 80 and 1010 steels are also shown for comparison. The 0.2 pct. offset yield and ultimate strengths of the duplex 2% Si steel

with respect to total elongation are shown in Fig. 36, compared with some of those selective commercial HSLA steels including Van 80 which is considered one of the best available HSLA steels. It is noted from this plot that the values of the corresponding yield strength in the duplex 2% Si steel show better than or at least comparable to the ultimate strengths of the commercial HSLA steels at the given total elongation. Of special interest is that the duplex 2 pct. Si steel shows notably high uniform elongation and extremely high ultimate strength which presumably are the consequences of its morphological features, which will be discussed later.

In Fig. 37 is shown the variation in reduction in area, a measure of ductility, as a function of pct. martensite of the as-quenched DFM steels. The DFM alloys 2 and 6 show a gradual increase in the reduction in area from about 15% up to 60% martensite followed by a progressive decrease up to 100% martensite, while the reverse behavior is observed in the DFM alloys 1 and 5. However, the values of the reduction in area in the duplex 2% Si steel (DFM alloy 4) remain relatively unchanged over a far-ranging volume fraction of martensite.

The room temperature tensile properties of the fully martensitic and DFM steels tempered at the predetermined temperatures are listed in Tables IV and V respectively. Figures 38 and 39 plot the variations in strengths and elongations, respectively, with tempering temperature for the fully martensitic steels. The modulations of yield and tensile strengths of the DFM steels as a function of tempering temperature are illustrated in Fig. 40, and those of elongation in Fig. 41. It should be noted that the as-quenched properties are not comparable since the alloys

differ in the volume fraction of martensite, as can be seen in Table V.

Figure 40 shows that ultimate strength of the tempered DFM alloys 2 and 4 (~ 30% MS) decreases very slowly with increasing tempering temperature up to 400°C followed by rapid drop up to 600° tempering, while yield strength remains almost constant at least up to 400°C. In the case of alloy 6 having 70% martensite, both of yield and ultimate strengths decreases continuously with increasing tempering temperature. This indicates that tempering behavior of DFM steel is significantly influenced by the amount of martensite volume fraction. On the other hand, the plot of elongation against tempering temperature (Fig. 41) for the alloys 2 and 4 shows that the uniform and total elongations increase initially up to 200°C tempering followed by a gradual decrease up to 400°C, and then rise again up to 600°C tempering temperature. Somewhat abnormal tempering behaviors are found in the alloy 5, compared to those of the rest of the tempered DFM steels. In Fig. 42 is shown the variations of reduction in area with tempering temperature for the tempered DFM steels 2, 4, and 5 containing 30~40% martensite.

(b) Impact Properties

Charpy V-notch impact tests were conducted at room temperature and subzero temperatures down to -75°C to evaluate the room temperature impact toughness of the as-quenched DFM steels 2, 6 and 4, to determine the influence of pct. martensite on the ductile to brittle transition temperature (DBTT), and to assess the DBTT characteristics of the DFM alloys. Except for a few charpy tests conducted at room temperature using the standard Charpy V-notch specimen, all impact tests were carried

out using the subsize impact specimens due to the limitation of the materials available. The results of the impact study are summarized in Table VI, and are presented graphically in Figs. 43 through 45. The data reported represent an average of at least two tests. In the data is also indicated the scatter of the impact energy values for each testing temperature.

Figure 43 shows the impact energy curves of the as-quenched 0.5 Cr DFM steels with two different martensite volume fractions. The curve with 35% martensite does not exhibit a definite DBTT, while the one with 90% martensite apparently does. The DBTT of the latter case was determined to be about -10° C, based on the measurement of the point of inflection in the energy curve, i.e., the temperature at which the materials capacity for plastic deformation changes rapidly.

Figure 44 shows similar variations of DBTT with pct. martensite in Si DFM steels. The apparent transition temperature was lowered by increasing the martensite volume fraction from 30% to 60% in the case of 0.5 Si steel, whereas 2% Si DFM steel showed no apparent DBTT and no significant difference in the impact energy as pct. martensite varied. Also included as a reference in Fig. 44 is the room temperature impact energy value of the 0.5 Si DFM steel (60% martensite) obtained from a standard impact specimen.

Figure 45 compares the impact energy curves of the DFM alloys 2 and 4, both of them having 35% martensite.

4. Fractography

The fracture morphology of the broken tensile specimens and Charpy impact specimens was examined in a scanning electron microscope.

The general fracture appearances of the fractured tensile specimens for all the as-quenched DFM steels were remarkably similar; at low magnification, the inner zone of the tensile fracture surface was randomly fibrous, which is indicative of stable, subcritical crack extension requiring relatively high energy, and at high magnification, crack propagation occurred by fracture predominantly from microvoid coalescence (Figs. 46a and b). On the other hand, the fracture surfaces of all the notched impact specimens were mostly associated with a large proportion of quasi-cleavage produced by a high deformation rate due to impact loading, as illustrated in Fig. 46c through 51.

All the initial martensitic steels showed primarily quasi-cleavage like fracture with a small proportion of dimpled rupture as shown in Fig. 46c. It is noted from the figure that the fracture plane changes orientations, resulting in the large quasi-cleavage facets whose average sizes was essentially identical with that of a division of the prior γ grain size by the groups of the same orientation of martensite laths. A magnified view of the facets, Fig. 46d, suggests that a group of fine, parallel tear ridges may be related to the martensite substructures since their common direction and spacings bear the resemblance of the pattern of martensite laths.

The mode of fracture changed significantly with the size of the impact specimens. In the case of DFM steels, standard specimens resulted

in a mixture of quasi-cleavage and dimpled rupture of which proportion depended on the relative amount of each constituent in the DFM structure. On the other hand, all the subsize specimens, regardless of alloy composition and martensite volume fraction, exhibited mainly quasi-cleavage like fracture without an appreciable quantity of ductile rupture at all testing temperatures used in this investigation. These are illustrated in Figs. 47-51. In Fig. 47 are shown optical micrographs and corresponding fracture surfaces taken from the fractured standard specimen of 4 Cr DFM steel ($\sim$20% martensite). Viewing the low magnification fractograph (Fig. 47b), the quasi-cleavage areas (marked with "A") appear to correspond to martensite particles since their morphology is similar to that of initial martensitic structure (Fig. 46c and d) and the volume fraction of the areas is also similar to the martensite volume fraction shown in the optical micrograph (Fig. 47a). Thus it appears that the predominantly dimpled rupture revealed in Fig. 47b was associated with the soft ferrite matrix. The higher magnification views of the quasi-cleavage and dimpled rupture areas are shown in Fig. 47c and d. A similar mixed mode of failure was observed in the other DFM steels except Si containing DFM steels which showed a higher proportion of quasi-cleavage than predicted by the volume fraction of martensite. This is shown in Fig. 48.

Am important observation was that the fracture surfaces of the DFM alloys 2 and 6 were associated with small particles on the bottom of the dimples as is seen in Fig. 49. The presence of the particles may be related to the cracking or decohesion of the coarse carbides which were observed by TEM in the above two DFM steels. This can be substantiated

by the similar size of the particles observed in SEM and TEM, and also by the fact that they were not present in the fracture surfaces of the other DFM alloys.

In Fig. 50 is shown the fracture features of the subsize impact speciments obtained from 0.5 Cr DFM steel (~ 60% martensite). It is noted that quasi-cleavage with no appreciable evidence of dimpled rupture dominated the mode of fracture in all the fractured specimens tested at 0°C (Fig. 50a), -20°C (Fig. 50b), or lower temperature. No apparent change in the fracture appearances was noted as the pct. martensite was decreased to ~30%. It appears from the above observations that the specimen's size effect overrides the microstructural effects on the fracture mode in this investigation. Similar fracture morphology was observed for the Si DFM steels where the impact specimens were subsized, as is seen in Fig. 51. The small cleavage facets contain river patterns, cleavage tongue, and are separated by tear ridges. A few shallow dimples are also visible. In all cases, the fracture surfaces revealed some evidence of secondary cracks, indicating the presence of cracking normal to the main fracture plane.

D. DISCUSSION

1. Influence of Alloying Elements Upon the Morphology of Duplex Microstructural Constituents.

The decomposition of austenite has long been a major subject of physical metallurgy[44,61] while much less attention has been directed to the formation of austenite.[62] Unlike the case of austenite decomposition, the formation of austenite involves further complications by the type of initial microstructures which play a key role in understanding the mechanisms, kinetics, and morphology of growth. Among the few systematic studies of austenite formation, most of the early works were concerned with the formation of austenite from ferrite-carbide aggregates,[63-65] but the formation of austenite from martensite as an initial microstructure has been studied in much less detail.[40,66].

The formation of austenite from martensitic structure may occur either by classical heterogeneous nucleations[63] at such lattice imperfections as prior austenite grain boundary, lath boundary, matrix/carbide interface, etc., or by a shear mechanism on a specific habit plane.[67,68] In the present study, however, the preferential precipitation of austenite along prior austenite grain boundaries (except with Si steel) and martensite lath boundaries, coupled with the gradual evolution of austenite particles with annealing time in the $(\alpha+\gamma)$ region, precludes the possibility of the transformation by a diffusionless shear reaction. The dominating influence of the boundaries in the austenite nucleation process arises from the additional surface energy available at the interfaces, as given by classical nucleation theory.[45] However, some attention should be given to the role of substructural features of

martensite in order to fully establish the mechanism by which this preferential nucleation event occurs in martensitic structures. First of all, concerning the presence of retained austenite that was trapped between lath boundaries in the as-quenched martensitic structure (Figs. 8–10), the preference for the martensite lath boundaries in the austenite nucleation event may be further enhanced by the decomposition product of retained austenite along the boundaries. That is, during heating of the martensitic structure in the two phase region, the retained austenite decomposes into ferrite and carbides. Thus formed carbides situated at the lath boundaries can provide active sides for austenite nucleation, but the relative significance of this process in controlling the number of nucleation events at the lath boundaries remains unanwered. Similarly, the potential effect of the auto-tempered cementite that was present in the fully martensitic structures (Fig. 11) may also have to be taken into account in the austenite nucleation process upon reheating to the $(\alpha+\gamma)$ region. However, careful observations made on many optical and transmission electron micrographs of DFM structures, in particular those of early stages of transformation, indicate that the autotempered carbides situated in the matrix (not at the boundaries) apparently did not provide sufficient nucleation sites to compete with the other favorable sites for austenite nucleation. This result is in agreement with that of Speich et al.[63] who observed preferential austenite nucleation at the carbides located at grain boundary, but not at the carbides present in the matrix.

The foregoing considerations lead to the understanding of the observed precipitation of austenite preferentially at grain and lath

boundaries of the initial martensite. The absence of austenite precipitation along prior grain boundary in Si-DFM steels will be discussed later. At late reaction times, however, marked differences developed in the morphology of austenite growth depending on the type and amount of alloying element, as has been demonstrated in Figs. 5 through 7. At this point, the pronounced differences in the pattern of austenite growth only in the interiors of the prior austenite grains will be discussed and the heterogeneities along the previous austenite grain boundaries will be considered separately later on. Figure 6 shows that the austenite in 4 Cr DFM steel appears to grow more less freely in every direction which results in equiaxed particles. On the other hand, when the Cr contents was lowered to 0.5 Cr (Fig. 5), the austenite exhibits marked directional growth with the result that predominantly acicular particles are formed. In Si DFM steels, however, two different Si concentrations resulted in essentially the same acicular growth of austenite as has been described before. This type of austenite growth in both of the 0.5 Cr and Si DFM steels is shown to exhibit the same general mechanism, the only differences being that the austenite particles are finer and more acicular in the case of the Si DFM steels.

The alloying element effects on the growth pattern of austenite from the initial martensitic structure have been observed by other investigators.[40,66,69] However, understanding of the mechanisms by which this occurs is not clear as yet, and no systematic work has been done in the past. Perhaps a unique and most useful study on this matter appears in the recent publication by Plichta and Aaronson.[40] They classified many ternary Fe/X/C systems (X being substitutional alloying element) into

three groups according to the observed morphology of DFM structures. In their work, the view is expressed that competitive processes between the nucleation and growth of austenite at lath boundaries and migration of these boundaries determine the final product shape. More specifically, according to their phenomenological explanation, rapid migration of the boundaries compared to the kinetics of austenite formation results in the austenite particles free from contact with the boundaries, thus allowing rapid spheroidization of the austenite crystals as in the case of Cr DFM steels. On the other hand, a high rate of austenite nucleation in Si DFM steels results in the restriction of the lath boundary migration, thereby ensuring the growth of the new austenite along the retained boundaries. They further argue that the globular shape of the austenite particles in Cr DFM steels is attributed to the solute drag effect upon growth. Acicular shapes in Si and Mn DFM steels respectively are a result of the decrease in the interfacial free energy for austenite nucleation and the lower temperature range of the no-partition Ae_3 — the $\gamma/(\alpha+\gamma)$ phase boundary when the alloying element concentration is the same in austenite and in ferrite.[61] However, the following experimental evidence exemplifies that their observation and explanations are inconclusive, and are not entirely consistent with the results of this investigation.

i) Evidently, they have not recognized the drastic change in the DFM morphology that occurs depending on the amount of alloying element. For instance, it turned out that an acicular shape of martensite particles was observed in 0.5 Cr and 4 Mn[40] DFM steels whereas a globular morphology was attained in 4 Cr and 0.5 Mn[70] DFM steels.

ii) As indicated in Fig. 6a obtained from 4 Cr DFM steel, the ferrite boundaries still subsist in the specific crystallographic directions maintaining original lath boundary morphology which may enable the austenite particles to grow in an acicular manner. Nevertheless, the austenite particles at the boundaries are shown to exhibit globular growth instead of an acicular growth pattern.

iii) It was thus found that their proposed mechanisms, viz. solute drag effect, interfacial free energy and no-partition Ae_3 temperature concepts could not explain satisfactorily the alloy element effect observed in this investigation.

Therefore, an plausible explanation for the influence of Cr and Si on the morphology of austenite from martensite is suggested as follows. Even in the absence of bulk partition of the element between the two phases, Cr and Si atoms may be required to diffuse for short distances along the austenite/ferrite boundaries before completing their transfer to the austenite phase, provided local equilibrium concentration of the alloying elements are obtained at the boundaries during growth.[71-73] This idea basically leads to the presence of a narrow concentration "spike" just ahead of and in contact with the advancing boundary. The existence of such a narrow concentration "spike" has been postulated by Kirkaldy[73] in his study of austenite decomposition. However, this is debatable[49] since its presence is indetectable due to the limits of resolution of the electron probe (the lattice image technique may reveal the extremely narrow, localized "spike", if any).

Assuming the presence of the concentration "spike", it becomes obvious that the kinetics of γ/α boundary migration should be strongly influenced by the type of alloying element present in the DFM steels. This is because the alloy "spike" will surround the growing austenite particles so that it controls the diffusion of carbon across the α/γ interfaces. In the case of Si steels, the Si concentration "spike" will act as a barrier to carbon diffusion from ferrite to austenite because of the repellent interaction between silicon and carbon atoms.[74,75] As a result, the lateral thickening of the austenite particles at the lath boundaries will be restricted. On the other hand, austenite can grow more rapidly along the lath boundaries where diffusion of carbon, viz growth of austenite is enhanced by the lath boundary diffusion. This process can more than overcome the carbon diffusion barrier due to the "spike" in the direction of the lath boundaries. As a result, austenite produced in such structures grows in an acicular manner along the lath boundaries, clearly reflecting the matrix structure existing at the time of austenite formation.

In the case of Cr DFM steels, however the Cr concentration "spike" is no longer a barrier to carbon diffusion as in the case of Si steels, but promotes the diffusion of carbon by means of the attractive interaction between Cr and C.[76] Thus it appears that the austenite growth morphology is determined by the kinetic balance between the carbon diffusion assisted by lath boundary and the concentration "spike".

In 0.5 Cr DFM steel, the influence of the boundary diffusion process may overwhelm the effect due to the concentration "spike" with a result that austenite particles grow predominantly along the lath

boundary. This situation is entirely changed as the concentration "spike" becomes higher, and hence more influential with increased Cr content, as in 4 Cr DFM steel. The dominating effect of the spike on carbon diffusion reduces two-dimentional and encourages three-dimensional growth, resulting in the globular shape of austenite particles. Even though the above rationalization based on the postulation of a concentration spike is capable of explaining the observed alloy element effect, fundamental studies are undoubtedly needed to clarify the proposed mechanism.

Turning now to the absence of austenite precipitation along the previous austenite grain boundaries observed in Si DFM steels, one can think of two possibilities that can account for this. Firstly, it is likely that the prior austenite grain boundary can be decorated by the formation of ferrite allotriomorphs during quenching from solution treatment. This occurs since Si is one of the most potent alloying elements which increase the rates of nucleation and growth of proeutectoid ferrite allotriomorphs.[77] In other words, the initial martensite structures may be associated with a thin layer of ferrite allotriomorph along the prior γ grain boundary. As a consequence, upon subsequent annealing in the two phase region, this ferrite phase inherited from the initial martensite structure may prevent the nucleation and growth of austenite along the otherwise preferred sites. This possibility however is excluded in this investigation after careful examination of the morphology of prior γ grain boundaries in many optical and transmission electron micrographs (e.g. Fig. 4).

The second possibility is related to Si segregation along the boundaries during solution treatmemt in the austenite field. Although positive proof of the grain boundary segregation was not attempted, the occurrence of Si segregation is expected since the observation has already been made that the as-quenched martensitic steels after quenching from 1100° C revealed substantial grain boundary segregation of the elements such as phosphorus, bismuth, and antimony.[78,79] If it occurs, austenite nucleation at the prior austenite grain boundaries will be prevented by the repellent interaction between carbon and the preoccupied silicon atoms at the boundaries.

Hence, it appears reasonable to conclude that silicon segregation is responsible for the absence of austenite precipitation at the prior austenite grain boundaries.

2. Tempering Behavior

Tempering of fully martensite steels is a common practice of physical metallurgy to impart a degree of ductility. This process involves various stages of complex reactions; segregation of carbon, precipitation and coarsening of carbides, decomposition of retained austenite, secondary hardening in the presence of carbide forming elements, and recovery and recrystallization. The mechanism and kinetics are significantly influenced by the type of alloying elements present in Fe-C systems.[80,81] Because of its technological significance and scientific interest in phase transformations, the tempering process of fully martensitic steels has been the subjects of numerous investigations,[51,80-83] and is fairly well documented and characterized.

With the present knowledge of the structures of tempered 100% martensite, tempering of DFM steels is of great interest in several respects. Firstly, it involves various stages of complex reactions in the ferrite matrix as well as in the martensite islands. The competitive process in both phases upon tempering leads to an interesting type of two phase aggregate. Secondly, and more importantly in this study, tempering at a specific temperature will change the mechanical properties of the individual phases. The resultant mechanical properties of the composite are not only noteworthy in view of its thermal stability but also will assist the understanding of deformation behavior of DFM steels, as discussed in a later section.

It was noted that the tempering behavior of the constituent phases present in the DFM steels was substantially different from what it would be in the absence of the other phase. At the tempering of 200° C for 1 hour, absence of appreciable carbide precipitation (except autotempered carbides) in the martensite suggests that most of carbon in the martensite is present either in the autotempered carbides or segregated to lattice imperfections such as lath boundaries and dislocations since the carbon segregated to defects is believed to occupy lower energy sites than are available in the carbides at this stage of tempering.[50-52] In contrast, a much lower defect density in the ferrite relative to that in the martensite results in large cementite precipitates in the areas where the dislocation density is very low, and very fine precipitates on dislocations of relatively high density, as may be seen in Figs. 22-25. Therefore it appears that defect density is the controlling factor in determining the presence of carbide precipitation in both phases up to

200° C tempering.

AT 400° C, coarsening of cementite in the ferrite and martensite undergoes a competitive process. The growth of cementite in ferrite is limited by its kinetics since it involves carbon diffusion over a greater distance relative to that in the martensite. On the other hand, cementite in the martensite is closely surrounded by an abundant supply of carbon. As a consequence, the competitive process results in the resolution of carbides in the ferrite with attendant precipitation and coarsening of cementite in the martensite, as demonstrated in Figs. 27 through 29. At this stage, it is evident that the ferrite regions still show finely dispersed precipitates on dislocations. At 600° C, however, excess carbon is entirely drained from the ferrite as the carbides present in the martensite regions coarsen further and spheroidize. Thus there is no indication of carbide precipitates in the ferrite, as is seen in Fig. 32.

The general features of the structural changes observed in tempered DFM steels have been described. Special attention will now be directed to the presence of coarse cementite precipitaiton in the Si DFM steels tempered at 200° C for 1 hour. A number of studies[48,84-87] have been made on the influence of Si in retarding softening during tempering in the temperature range of 150° ~ 400° C. Altstetter et al.[86] found the first indication of cementite on tempering at 270° C in steels with 0.26 Si, at 370° C with 1.6 Si, and at 455° C with 3.2% Si. This indicates that the tempering temperature for appreciable cementite formation increases with at. % Si -- a result shared by many investigators in a variety of steels containing Si as an alloying element.[48,87,88] Mechanisms suggested to explain this phenomenon by various investigators are at variance with

each other. Whatever the mechanisms are, the experimentally observed results on this subject in the literature suggested with about equal fervour two possible effects of Si on tempering.

(1) Nucleation of cementite is delayed by the presence of Si.

(2) ε carbide is stabilized to a much higher temperature than in a comparable steel without silicon.

In view of these effects of Si on the tempering behavior of steels, the results of the present investigation are surprising from the evidence that the precipitation of large particles of cementite was observed in the 2% Si steel tempered as low as 200°C, as shown in Fig. 23. This observation is consistent with the earlier work by Leak[89] who finds that the bulk diffusion of carbon in ferrite is not affected by Si up to 3 wt. pct.— a view which has not received general support.

It should be noted, however, that this cementite was present only in the ferrite constituent, but not in the martensite regions.

This leads to the speculation that the influence of Si in retarding softening may be controlled by specific substructural features, instead of general Si—C interactions that have been suggested by Owen[80] and many others.[48,86]

Further study is of course needed to substantiate this point of view.

3. Strengthening Mechanisms

It will be of some interest to examine the factors governing flow properties of DFM alloys and related strengthening mechanisms in similar systems. Any two phase material in which one component plastically deforms less than the other results in a very non-homogeneous stress and strain distribution upon deformation.[90] Theoretical explanations of the strain inhomogeneity in terms of dislocation theory involve the motion of dislocations impeded by a microstructural barrier. Thus the mechanical behavior of two phase materials depends on a specific mechanism by which slip can be transmitted across the barriers (i.e., strengthening microstructures); this in turn, is governed by the nature of the barriers.

When the barriers are point obstacles, such as in dispersion strengthened alloys, the dislocation encounter the obstacles and try to bypass them by the Orowan mechanism.[22] The resulting flow stress required to achieve the bypass process is given by

$$\tau = \tau_0 + \alpha \frac{Gb}{\lambda_p} \qquad (2)$$

where τ_0 = flow stress of the single phase matrix

α = geometrical constant depending on the particle shape and distribution

G = Shear modulus of the alloy

b = Burgers vector of the glide dislocations

λ_p = average interparticle spacing.

Orowan strengthening becomes appreciable for two phase materials in which the average interparticle spacing is less than a few microns.[23] On the other hand, in the extreme case where the particles are continuous and unidirectionally aligned in the direction of applied stress, which is the case in a fiber reinforced composite, the resulting flow stress of the system is governed by Eq. (1). The derivation of Eq. (1) is based solely on the fiber loading concept, and not on an actual dislocation mechanism. It is well established that the Egns. (1) and (2) can provide the quantitative predictions of strengthening for the respective systems. However, much less is known about the mechanism which governs the flow property of the transition two phase material between the aforementioned two extreme cases. The transition case includes such technically important duplex alloys as ferrite-pearlite, spheroidite and DFM structures. The majority of the studies on their plastic deformation rely on experimental observations due to the difficulty in theoretical analysis arising from their geometrical complexities.[25,26,30]

In such two phase materials containing the second phase constituent of $1 \sim 50\ \mu m$ in size, the major microstructural barriers which are more likely to be surfaces can not be bypassed by dislocations. Nor can they be treated simply on the bais of fiber strengthening models. In other words, Eqns. (1) and (2) may be related to, but are not directly applicable to the strengthening mechanism in this situation.

Earlier experimental studies on pearlitic and spherodized carbon steels showed that the flow stress of the ferrite in these structures is controlled by the mean free path in the ferrite according to the

Hall-Petch equation,[24,60,91-92] while others preferred the Orowan relations[23,74] or still other mechanisms. In spite of these inconsistences, the conclusion common to all these studies is that the available slip distance in the ferrite is the most important variable in determining strength. This, in turn, is determined by the size, shape and distribution of the second phase constituent in a matrix. Therefore, in cases where the second phase particles are spaced at distances less than the mean dislocation slip length (in a metallic matrix, $1 \sim 50\,\mu$ in most cases), enhanced strengthening of the matrix will result and its property will be no longer those of the single phase matrix. However, if the interparticle spacing is larger than $50\,\mu$ or so, the contribution from either Orowan strengthening or Hall-Petch strengthening[35,36] to the matrix flow stress will be very small.

The flow stress of such two phase alloys in which the matrix constituent is continuous has also been analyzed by Ashby.[94] According to his micromechanistic model the density of "geometrically necessary" dislocations which are formed to allow the two phases to deform in a compatible way is expressed as follows:

$$\rho_G = \left(\frac{1}{\lambda_G}\right) \frac{4\gamma}{b} \qquad (3)$$

where b is the Burgers vector and γ the shear strain. For alloys containing spherical particles, $\lambda_G = r/f$ where r is the particle radius and f the volume fraction. For alloys containing needle or plate-like particles, λ_G = the surface to surface separation of the particles. The flow stress is then given by

$$\tau = \tau_0 + KGb\sqrt{\rho_G} \qquad (4)$$

where K is a constant.

Equations (3) and (4) predict that flow strength should be enhanced as the volume fraction of the hard phase increases since thereupon λ_G decreases, and that the effect should diminish at large strains. The equations reduce to the Hall-Petch relation with interparticle spacing λ_G. The serious drawback of the Eqns. (3) and (4) is that they do not take into account the fiber loading mechanism which may be simultaneously operative for the flow property of the transition duplex materials under consideration. In fact there is good experimental evident that both microscopic (dislocation) and macroscopic (fiber load) mechanisms are necessary in order to explain the plastic deformation in the ferrite-carbide aggregates.[60,95] Wilson[96] showed that the non-deforming particles contribute to the load carrying capacity of the specimen as elastically-stressed inclusions in addition to acting as barriers to dislocation motion.

In view of crack propagation through localized stress regions in the soft matrix, if a continuous path exists in the matrix the crack may grow without traversing the harder phase. For the duplex alloy in which the hard phase occurs as needles or plates, this path will be more tortuous and the crack must either traverse the fibrous particles resulting in some dissipation of crack propagation energy or stop growing altogether.[21] Kelly[97] concludes that the only way to ensure that the strong phase particles contribute their maximum load carrying capacity to the

duplex material is to be arranged as either fibrous or plate-like shape.

In summary, it appears that the mechanical behavior of the transition duplex alloys including DFM steels is believed to be controlled by both microscopic and macroscopic mechanisms. These, in turn, are determined by the size, shape and distribution of the second phase constituent. At this time, it is reasonable to arrive at a general conclusion that, for a given volume fraction and number of particles in a soft matrix, fibrous particles are preferred to spherical ones so as to achieve more effective strengthening of the composite.

4. Stress-Strain Characteristics

Having considered the strengthening mechanisms of the DFM alloys, a study of the characteristic stress-strain behavior will be useful in providing direct information on the process of plastic deformation of the composite.

The detailed load-elongation response of the DFM alloys is illustrated in Figs. 52 and 53. The relatively low yield strength, coupled with extremely high rate of work hardening, in the early stage of plastic defomration of the 2% Si DFM alloys (4S1, 4S2, and 4S3) results in a high tensile/yield strength ratio and good elongation to necking, as is shown in Fig. 52. Also shown in Fig. 52 for comparison is the engineering stress-engineering strain curves for fully martensitic structure (4A) and a commercial HSLA steel, Van 80.[11] Figure 53 reveals the variation of the curves with respect to the different volume fraction and morhpology of martensite particles.

Referring to Fig. 52, it appears that the yield strengths of the 2% Si DFM steels increase with increasing volume fraction of martensite particles. In view of the fiber loading concept alone, this is not to be expected since the elastic constants of ferrite and martensite are equal[98,99] and hence there is no stress concentration in the elastic range, and therefore yielding starts simultaneously at all points in the matrix, independently of volume fraction of the martensite.[99] The micromechanistic model, however enables the increase in yield strength to be explained according to Eqns. (3) and (4), viz, as volume concentration of the martensite particles increases the effective interparticle spacing (λ_G) decreases, giving an increase in flow stress.

In the early stage of plastic deformation of the composite, strong phase particles (martensite) do not deform with soft phase matrix[31] (ferrite). Mobile dislocations are impeded by the particles. The dislocation density increases rapidly as further deformation proceeds, resulting in an increase in effective size of the particles. In this way, stresses are built up, in and around the particles. The resultant stress-strain features include early and farily extreme work hardening rates which do suppress mechanical instabilities. As a consequence, the transition from elastic to plastic deformation is smooth without showing yield point phenomena that have been observed in a number of metals and alloys both in the single and polycrystalline state, e.g., note the yield point elongation in the load-elongation curve for Van 80. This mode of behavior continues until the yield stress of the martensite particle is reached at about 3% deformation. Here the dislocation will start to cut

through the semi-coherent martensite particles on the slip systems that are common to ferrite and martensite. As deformation proceeds the load required for further deformation increases. However, after the onset of large scale yielding the work hardening rate of the DFM alloys decreases and becomes virtually equal to that of Van 80, regardless of the martensite volume fraction, as shown in Fig. 52.

The gradual equalization of work hardening rates at high strains is in agreement with the calculations of the finite element method,[99] which indicated that when the hard phase (martensite or carbide) yields, the work hardening rate of the composite becomes equal to that of ferrite but at a higher flow stress level.

As is displayed in Fig. 52, another characteristic feature of the stress-strain behavior for the duplex 4S alloys is the large elongation to necking and relatively small strain to fracture after the onset of plastic instability (indicated by the arrow marks). This phenomenon is believed to be in part due to the good coherency across the ferrite/martensite interfaces as is evidenced by the continuous lattice fringe images (Fig. 57). That is, strong particles that do not have good atomic fit with the matrix are known to act as sites for failure by decohesion or to encourage the formation of interfacial micro-cracks at the weak interface between particles and matrix.[38] Therefore, a good bond is necessary to prevent interface failure, and to enable the full toughness of the ferrite to be realized. On the other hand, if the coherency is too good an approaching crack is less likely to be deflected from its path resulting in the less energy consumption for crack propagation across the interface. This, in turn, can result in ease of crack propagation with a small elongation

to final fracture after the initiation of a crack. However, most workers agree that a good coherency is essential for effective load transfer.

The effect of the martensite volume fraction on the tensile behavior is clearly reflected in the curves in Fig. 52. As the volume fraction increases:

i) the initial rate of work hardening appears to be increasing.

ii) at high strains, the work hardening rates are virtually the same, but at a higher flow stress level.

iii) uniform and total elongation decrease in a linear fashion, accompanied by a corresponding increase in yield and ultimate tensile strength.

A similar trend is observed in the load-elongation curves (Fig. 53) for the 2S and 5S alloys containing a different shape and distribution of martensite relative to that of the 4S alloy. However, it is clear from Figs. 52 and 53 that the tensile curves for the 4S alloy show superiority to those of Van 80, 2S, and 5S alloys, as was previously shown in the various plots of their properties.

5. Correlation of Duplex Microstructure with Mechanical Properties

Many factors affect the mechanical properties of a simple ternary Fe/X/0.1 C alloy with DFM structures, among which are, (1) size, shape, distribution and volume fraction of martensite in the ferrite matrix, (2) properties of the constituent phases, and (3) microstructural features, such as the presence of coarse carbides. The alloying addition X and the exact heat treating conditions control these main structural features which are closely related to the corresponding mechanical property in this section.

(a) Tensile Properties

Strength and Elongation

Figure 35 reflects the way in which the tensile properties of the various DFM steels vary as the major structural parameters are changed. Due to a mutual interaction of above mentioned factors, it is difficult to evaluate their individual effects in fundamental terms. However, an attempt is made here, with the aid of Figs. 33 and 34, to gain some qualitative understanding of the duplex structure-property relations.

The addition of silicon tends to confine dislocations to the {110} planes,[81] i.e., hinders cross slip. As a result, it has been shown that tensile ductility decrease slightly with increasing silicon content.[100,101] Nevertheless the duplex 2% Si steel reveals higher values of elongations, if the martensite content is below 60%, than those of the duplex 0.5 Si steel. This must be related to the presence of coarse carbides in the immediate vicinity of α/martensite interface observed in the 0.5 Si DFM steel since otherwise the metallurgical variables in the two steel were virtually identical. These pearlite type of carbides, shown in Fig. 20, can be very susceptible to cracking upon deformation since their locations are distributed near the interface where localized stress concentration takes place.[20,34] Under a sufficient applied stress, a such formed crack within a carbide can lead to an interpacticle microcrack in the ferrite and premature failure of the specimen. This results in the reduction of full ductility of the ferrite in the 0.5 Si DFM composite. This situation is analogous to that of a grain boundary cementite film which has an important influence on the cleavage fracture strength of

low-carvon steels.[102,103] As is seen in Fig. 34, the difference in the values of elongation for the two steels is gradually diminishing as the volume fraction of martensite increases. Furthermore, the relative levels of the total elongation become equal at about 50% martensite. Incidentally this point of pct. martensite was observed to be the approximate transition from heavy to much reduced precipitation of the carbides in the 0.5 Si SFM steel. Consequently, beyond this point, the elongation values of the 0.5 Si DFM steel are not significantly reduced by the carbides. Hence the trend for the lower values of elongation beyond 50% martensite in 2% Si DFM steel compared to 0.5% Si DFM steel may be due to the predominantly harmful influence of the higher amount of Si on tensile ductility. These observations provide a good indication of the role of the brittle carbides in the tensile behavior of the DFM steels, as evidenced by the presence of small particles on the fracture surfaces (Fig. 49).

The data in Fig. 34 also indicates that, for a given volume fraction of martensite, the values of elongation in silicon-bearing DFM steels are higher than those in chromium-containing alloys. The major reason for this is attributed to the difference in the connectivity of the martensite in the ferrite matrix. As noted in Figs. 5 and 6, while the martensite particles in Si containing DFM steels were discontinuous throughout the matrix, those of Cr containing DFM steels formed a continuous network along the prior austenite grain boundaries as an inevitable product of the phase transformations in the system. The continuous second phase particles will be directly loaded at their ends so that plastic deformation will involve breaking of the martensite particles in a

relatively early stage prior to appreciable plastic deformation of the ductile ferrite matrix. Contrarily, the deformation process in the DFM steels with discontinuous particles (discontinuous DFM steels) is such that the continuous soft phase ferrite will accomodate the plastic flow with the result that cracking of the martensite particles, if any, will occur at a later stage relative to the case of continuous second phase. Therefore, the initiation of a crack will occur most easily in DFM steels with continuous networks (continuous DFM). Concerning the propagation of a such nucleated crack though the composite, Kunio et al.[104] observed that the connected DFM steels deform in such a manner that the slip system was confined to {110} ⟨111⟩, hence the incipient crack triggers cleavage cracks in the ferrite regions, while the propagation of the crack in the discontinuous DFM steels was impeded by the plastic blunting at the crack tip due to the multiple slip systems available. The foregoing discussion on the crack initiation and propagation suggests that the discontinuous DFM steels have a preferred microstructure to those of continuous DFM steels in terms of improved elongation at a given volume fraction of martensite. In addition to the difference in the martensite connectivity along the prior austenite grain boundary the term connectivity of martensite will also include a contribution resulting from the size and distribution of the martensite particles within the prior γ grain. For instance, the larger particle size observed in Cr containing DFM steels will be more connected with respect to the crack propagation through the particles than the fine scale particles produced in Si bearing DFM steels.

Considering the aspects of crack initiation and propagation in the DFM steel, the connectivity of the strong phase martensite appears to

play an important role in determining tensile ductility. At a given volume fraction the superior values of elongation of silicon bearing DFM steel to those of Cr-bearing steels are presumably the consequence of the above reasoning.

Although it has been possible to isolate the effects of martensite geometry and microstructural features (carbides), the other controlling parameters mentioned earlier are difficult to single out. Certainly, the property data in Fig. 35 are the net result of the combined effect of the important structural parameters. Thus, from the proceeding discussion on the structure-property relations and strengthening mechamisms, the superior tensile property found in the duplex 2% Si steel are attributed to its favorable microstructural features which were produced according to the design principles:

It consists of predominantly dislocated martensite in a fine, fibrous distribution, provides strong solid solution strengthening in ferrite through the effect of silicon, and improves the ferrite/martensite interface by inhibiting the formation of coarse carbides during the final quench. As discussed earlier, the strengthening components from a fine, fibrous martensite morphology appear to be two-fold; it offers more effective barriers to the motion of dislocations, and simultaneously provides more efficient composite strengthening.

In addition to the beneficial effect of Si on the production of DFM structures, silicon is a valuable alloying element since it opens up the $(\alpha+\gamma)$ range when added to Fe-C system, as in Fig. 54. As a result small variations in annealing temperature in the $(\alpha+\gamma)$ range do not

change composition significantly, thereby assuring reproducibility of the material. Thus Fe/Si/0.1 C steels appear to be very promising for duplex treatments as noted also in Japan.[116-118] However, the published work on these steels does not appear to take into account the desirable marco- and microstructural morphologies which are obtainable under the limitation of practical feasibility. The desirable features have been illustrated in the present work in the duplex Fe/2 Si/0.1 C pct steel which exhibits better tensile properties than those of Van 80 which is considered to be one of the best commercial HSLA steels. The possibility of using these DFM steels for automotive applications e.g. to replace conventional 1010 steels is apparent. The data in Table VII indicate that the tensile properties achieved in this new steel already exceeds the industrial goals for HSLA steels for the automobile industry.

Thermal Stability

In this section concerning tempered DFM structure-property relations only two alloys (2 and 4) of which microstructural changes have been characterized will be considered in the discussion. The tempering response of the DFM steels as a measure of their thermal stability is shown in Figs. 40 and 41. Since tempering treatments result in the microstructural changes in both at the matrix (ferrite) and second phase (martensite), the final mechanical properties of the DFM steels will be determined according to the corresponding property changes in the individual constituents.

Up to 400° C tempering, the strength of the ferrite is expected to remain nearly constant. This is because i) the carbon was not fully drained from the ferrite, ii) the dislocation density was not dramatically reduced, and iii) the solid solution strengthening due to carbon can be counterbalanced by the precipitation strengthening resulting from the dispersion of Fe_3C particles. On the other hand, strength of the martensite is likely to show a decreasing trend following those for the fully martensite structure as shown in Fig. 38. Nevertheless, Fig. 40 shows non-varying yield strength of the two alloys with respect to the tempering temperature up to 400° C. This suggests that the yield strengths of the alloys are not affected by the variation of martensite strength, i.e., yield strength is insensitive to the strength or hardness of the second phase, and is only determined by the flow properties of the ferrite. This result is in agreement with the earlier observation.[60,70,99]

While the yield strength of the composite is related only to the strength of the ferrite matrix, variations of tensile strength as a function of tempering temperature seems to be associated with the softening of the martensite. This can be readily understood with the aid of Fig. 40 and Eq. 1. In Eq. 1 V_f, V_α, and σ_α are constants in this case, hence the composite strength (σ_c) is a function of σ_m (martensite strength). Upon tempering, therefore, variations of σ_c will show the patterns of the behavior of σ_m. Evidently, this is shown in the tensile curves for the two alloys in Fig. 40. It should be noted, however, that as tempering temperature increased, the composite tensile strength decreases with a much slower rate than that of 100% martensite due to the non-varying strength contribution from the ferrite. The foregoing discussion will be valid only if the

ferrite constituent occupies sufficient volume fraction. For instance, the 0.5% Si DFM steel contains approximately 70% martensite (30% ferrite) and thus its yield and tensile strength variations are strongly influenced by the martensite properties as indicated in Fig. 40.

Contrary to the strength variaitions upon tempering, the tempering response of the tensile ductility appears to be very sensitive to the microstructural changes occurring both in the ferrite and martensite. This can be seen in Figs. 39 and 41. After tempering at 200° C, negligible martensite softening as evidenced by the microstructure characterization, coupled with the segregation of carbon atoms to lattice defects, apparently resulted in a slight decrease in the elongation of alloy 4 which is 100% martensite, as shown in Fig. 39. Nevertheless, the values of elongation, especially total elongation of the composite, shows a sharp initial increase in Fig. 41. Therefore, this increase must be related to the change in ductility of the ferrite after 200°C caused by a partial depletion of carbon atoms from the solution as well as defects to form coarse cementite. Evidently, this resulted in improved ductility of the ferrite matrix and eventually of the composite. It is interesting to note that the improvement of composite ductility (after 200° C) is achieved without a significant sacrifice in strength. This result can make use of the paint baking process if the material is applied to the automobile industry.

After 400° C tempering, the strength of the fully martensitic structures decreased with an attendant increase in elongation, as shown in Figs. 38-39. At the same time, the ductility of the ferrite constituent is expected to be somewhat improved since the coarse widmanstatten cementite was not present, and is probably transferred to the martensite regions, as

discussed earlier. Nevertheless, the DFM composite consisting of the martensite and ferrite, with improved ductility, showed a decrease in elongation, as seen in Fig. 41. This is probably due to the significant morphological changes in the martensite particles which were heavily associated with coarsened and spheroidized cementite, particularly along the ferrite/martensite interfaces. These carbides which were situated at the regions where stress concentrations occur can cause premature failure by means of interface decohesion or carbide cracking.

At 600° C tempering, the composite is no more a DFM structure, but a ferrite-carbide aggregate. Both of the ferrite and former martensite regions become completely ductile, away from the presence of the spherical carbides. Thus, there is a small increase in the elongation, but this is accompanied by a significant decrease in strength. Comparing the tensile properties of 2% Si composite structure tempered at 200° C (which is a DFM structure) and at 600° C (which is a ferrite-carbide aggregate), one notes that DFM structure offers superior properties.

The following is a summary of the discussion in this section:

(1) The yield strength of the two DFM structures (~25% martensite) was determined by the flow stress of the ferrite, and was not affected by the strength of the martensite.

(2) The as-quenched yield strength was maintained up to 400° C tempering for 1 hour. The tensile strength of the composite, however, showed a gradual decrease with increasing temperature, but with a much slower rate than that of 100% martensite.

(3) Tempering at 200°C for 1 hour resulted in improvement of tensile ductility without significant loss in strength. A higher tempering temperature resulted in no further improvement in tensile properties.

(4) The DFM structures showed superior tensile properties than the ferrite-carbide aggregate with otherwise similar metallurgical variables.

The above conclusions could be established from a fundamental understanding of the tempered duplex microstructure—property relations.

Reduction in Area

The advent of techniques such as TEM led to numerous excellent papers devoted to structure—property relations. Unfortunately, however, reduction in area is one of the mechanical properties whose correlation with microstructural features has not been completely established. The general lack of data in the literature concerning the influence of the microstructural variable on reduction in area may be due to the complexity of analysis and inconsistent results depending upon the systems studied.

It has been known that the most important structural factors affecting reduction in area is the volume fraction of the second phase particles.[105] However, this conclusion is not consistent with the results obtained in the present investigation. For instance, the values of reduction in area for the DFM alloy 4 remain almost unchanged over a wide range of martensite volume fractions, while those of the other alloys show various responses, as shown in Fig. 37. It appears from Fig. 37 that 60%

volume fraction corresponds to the maxima or minima of the curves. It is not certain, however, what structural factors are affecting the shapes of the curves.

For a fixed percent of martensite, the variations of the reduction in area with respect to tempering temperature (Fig. 42) show similar patterns of behavior as those of elongation (Fig. 41), but with different magnitudes.

Thus, the influence of the tempered microstructure on the reduction in area may be explained as before. However, this investigation does not include an attempt to establish correlations of the duplex microstructure with reduction in area.

(b) Impact Properties

From Figs. 43-45, one notes that the impact properties of the DFM steels are strongly affected by the three major structural factors: morphology (shape, size and distribution) of DFM structure, volume fraction of martensite, and toughness (carbon content) of the martensite particles. The last two factors are correlated to each other since the carbon content is a linear function of the volume fraction of martensite.

As the volume fraction decreases it is expected:

(1) The connectivity of martensite will decrease, thus resulting in better impact properties.

(2) Concurrently, toughness of the martensite will decrease due to increased carbon enrichment, thereby decreasing impact properties since the carbon level has a drastic effect on reducing notched impact energy and DBTT.[4]

Therefore, for a given morphology of DFM structure, the observed effect of volume fraction on the impact properties will be determined by the balance between the two opposing factors.

For the 0.5 Cr DFM structure tested up to room temperature, the energy curve with higher volume fraction (90% Ms) exhibited better impact energy, and showed an apparent DBTT, (Fractography study indicated that fracture surfaces corresponding to the apparent upper and lower shelves showed all quasi-cleavage without any evidence of the change in the fracture mode. It should be noted,therefore, that the transition temperature does not represent the true DBTT that is measured from the standard speimen, since the DBTT is greatly sensitive to the triaxiality of the stress around a notch caused by different specimen geometry.) while no DBTT was present in the one with the lower volume fraction (35% Ms). This result may be due to the fact that the toughness factor has an overwhelming influence on the notched impact toughness compared to the connectivity (as determined by volume fraction) factors.

In contrast, the 2% Si DFM structure yielded essentially identical energy curves for two different volume fractions of martensite, as is seen from Fig. 44. This means that toughness and connectivity factors counterbalanced each other to result in no variations in the curves. The presence of the apparent DBTT at 60% martensite of 0.5% Si DFM steel indicates that some adjacent needle-like martensite particles joined together at this high volume fraction, and thus resulted in the similar behavior as that of 0.5% Cr steel. On the other hand, as for 2% Si DFM, the individual martensite particles are still separated and surrounded by the ferrite matrix at 60% martensite, maintaining the same fibrous morphology

as that of 30% martensite, thereby resulting in identical energy curves for the two volume fractions.

The above observations indicate the significant role of the duplex structural features in determining impact properties with respect to the volume fraction of martensite. Figure 43 compares the impact properties for alloys 2 and 4 at the same volume fraction (35% Ms), showing that fine, fibrous DFM structures are preferred to the other microstructures (Fig. 5) in terms of the improved notched impact energy.

(c) Origin of the Superior Tensile Properties

DFM structure is a composite consisting of a ductile matrix (ferrite) and a strong second phase (martensite) of the same component system. As in many other composites, the martensite constituent carries the major portion of the applied load; and the role of the ferrite matrix will be as follows:

(1) The matrix binds the martensite particles together, and provides the means through which the applied load is effectively transferred into the strong particles.

(2) It will separate them so that cracks are isolated and contained within the individual particles rather than propagating continuously and catastrophically through the composite.

(3) It will provide a mechanism for slowing down cracks that might have originated at the martensite particles.

In the last two years, a number of investigators have reported the extremely attractive features of DFM structures, leading to an intensive

development program.[6-14] Questions have arisen as to what makes the DFM structure so superior. Unfortunately, no fundamental understanding of the origin of the superior properties appears so far in the literature.

Therefore, based on the present investigation, the following features are suggested as the origin:

1) high purity of ferrite;
2) strong and tough martensite;
3) equal elastic constants;
4) good coherency at the ferrite/martensite interface.

The important role of these factors in determining tensile behavior has been discussed in the preceding sections, but is briefly summarized here.

The nature of the phase transformations occurring in the ($\alpha + \gamma$) range produces ferrite, free from any coarse precipitation, with an extremely low quantity of interstitial elements. Such pure ferrite will maximize its functions during composite action. Indirect evidence for this was that further improvement of the ferrite ductility after 200° C tempering resulted in the enhanced tensile ductility of the composite as discussed before.

With regard to the toughness of martensite, the total alloy composition in the γ during two phase annealing is controlled so as to produce both strong and tough martensite after quenching. Therefore, unlike the other composites in which the strong second phase is brittle in most cases, the strong and tough martensite particles in DFM steels will allow the full exploitation of the ferrite ductility to be realized.

Equality of the elastic modulus between the martensite and the ferrite will also play an important role in suppressing early yielding. This is accomplished by eliminating stress concentration, as described before. Good coherency will prevent interface decohesion. In addition, since the nature of the ferrite/martensite interface showed a high degree of coherency, the coherency strain can also contribute to strengthening, essentially by increasing the interaction distance between dislocations and the martensite particles. This will lead to additional contributions to the flow stress of the composite.

The factors listed above describe the general attractive features of all DFM structures. Superior tensile properties among the other DFM alloys have been achieved with the new 2% Si DFM steel through the consideration of desirable micro- and macrostructural features on top of the four factors listed.

IV. LATTICE IMAGING OF CARBON STEELS

A. INTRODUCTION

High resolution electron microscopy has been shown to give new information on defects[106] and phase transformations in solids.[107-109] In a continuing program of lattice fringe imaging of alloys, we have applied this technique to the martensitic transformation in steels in order to characterize the atomic environments near twin, lath and α/martensite boundaries. This section describes current progress in this program.

B. EXPERIMENTAL

TEM specimens used for this study were cut from the 2% Si DFM steels containing about 20% martensite. Thin foils were prepared by the same techniques described in section III-B-5. Lattice images and the corresponding electron diffraction patterns were taken using a Philips EM 301 transmission electron microscope. Optical diffraction patterns were obtained using a standard optical diffractometer with a He-Ne laser illumination source. Orientation of the foil was chosen such that $\{110\}_\alpha$ fringes could be imaged since $\{110\}_\alpha$ planes have the largest d spacing ($d_{110} \simeq 2.03$Å). Detailed experimental procedures for lattice fringe imaging and interpretation of the fringes are described elsewhere.[110]

C. RESULTS AND DISCUSSION

1. Lattice Fringe Images of Twin, Lath and α/Martensite Boundaries

Figure 55 A and B show lattice image and conventional bright field image of the same area of a duplex Fe/2Si/0.1C steel described before. The microstructure consists of internally twinned martensite (M) embedded in a ferrite matrix (F). Use of the 2-beam tilted illumination technique incorporating a twin reflection produced {110} fringes across the microtwins. A group of microtwins thus obtained are illustrated in Fig. 55 A with the corresponding selected area diffraction pattern. The $(0\bar{1}\bar{1})_M$ and $(0\bar{1}1)_T$ fringes make an angle of 73° with the $(\bar{1}21)$ twin interface which appears to be perfectly coherent and shows classical mirror reflection. The fringes running in the direction of the twin interface with larger periodicity than that of {110} planes are Moiré fringes. The fringe spacing, λ, for two crystals which differ in orientation is given by[111]

$$\lambda = \frac{d}{\eta}$$

where $d \simeq 2.03$ Å, the spacing between two adjacent (110) planes, and η the angle between two orientation with respect to the incident beam, is

~34°. Substitution of these values to the above equation yields $\lambda \simeq 3.43$Å. This value is in good agreement with the measured average spacing (~3.46Å) of the Moiré fringes. Correlation between lattice fringes and the indexed diffraction pattern shows that the twinning plane is parallel to the incident electron beam. This and the appearance of Moiré fringes suggest that the microtwins do not make up the total thickness of the foil.

Figure 55 C displays {110} lattice fringes, showing the atomic arrangement near a martensite lath boundary. As the (110) fringes cross the boundary, they are distorted but are continuous except for occasional end-on dislocations. This is also illustrated in Fig. 56 where the areas associated with black patches represent a martensite lath boundary which is inclined with respect to the incident beam. Similar continuity of lattice fringes is shown at the α/martensite boundary (Fig. 57), where the martensite region is distinguished by black and white patches probably due to the high density of dislocations. The arrows indicate the interface which corresponds to the encircled area in the bright field micrograph (Fig. 57 a). The continuity in this case is interpreted as follows. Assuming the K-S orientation relationship holds in the $\alpha + \gamma$ mixture at 950°C then for $(111)\gamma$ the particular variant of the six possible $\{110\}\alpha$ will be the $(10\bar{1})\alpha$ which already exists parallel to $(111)\gamma$ across the original $\gamma - \alpha$ interface. Hence on transformation $\gamma \rightarrow \alpha$, $(111)\gamma$ becomes $(10\bar{1})\alpha$ parallel to $(10\bar{1})\alpha$ in the pre-existing ferrite. This is consistent with the measured d spacings.

2. Carbon Analysis

It has been emphasized in a preceeding section that the carbon content of the martensite is an important structural parameter in determining mechanical properties, in particular impact properties, of DFM steels. However, any attempt to determine the carbon concentration from the equilibrium phase diagram will be inaccurate since the two phase annealing for 20 minutes is a non-equilibrium reaction. Analytical measurements involving x-ray and electron probe techniques become extremely difficult for the submicron martensite particles (e.g. Fig 19). Lattice fringe imaging, however, is a powerful technique in analyzing extremely localized chemical composition.

In this study, carbon concentration was measured directly from the lattice fringe images using the relationship between carbon content and the tetragonality of martensite. The tetragonality of martensite, i.e. the mean anisotropic distortion of the lattice, increases with increasing carbon content, and is given by[112]

$$C = 2.8664 + 0.116 \times \text{wt. \% C} \qquad (5)$$

$$A = 2.8664 - 0.013 \times \text{wt. \% C} \qquad (6)$$

The d spacing of a (hkl) plane for a tetragonal structure is related to the corresponding lattice parameter as follows:

$$\frac{1}{d^2} = \frac{h^2 + k^2}{a^2} + \frac{\ell^2}{c^2} \qquad (7)$$

In Fig. 57 the ferrite (no tetragonality) and martensite phases are separated by the interface. The average fringe spacing directly measured in the martensite region was appreciably larger than that in the ferrite, indicating that the C-axis is not parallel to the lattice fringes (i.e. in equation 7, $\ell \neq 0$). Optical diffraction patterns taken from the areas of the ferrite, martensite, and α/martensite interface are shown in Fig. 58 , where d_{101} (assuming the {110} plane was specifically (101) plane) spacings of the ferrite and the martensite are shown to be unequal. A slight change in orientation across the interface is also seen in the figure.

For the specific case of Fig. 57, equation 7 reduces to

$$\frac{1}{d_{101}^2} = \frac{1}{a^2} + \frac{1}{c^2} \qquad (8)$$

The d_{101} value for the martensite should not be obtained from direct measurement of the average fringe spacing since this is based on the microscope magnification whose accuracy is not always guaranteed. Therefore, d_{101} for the ferrite is taken as reference, and on this relative basis d_{101} for the martensite is determined. Thus measured d_{101}, as well as a and c in equations 5 and 6 respectively are substituted to equation 8 to obtain the required carbon content in the martensite. For the DFM structure in Fig. 57, d_{101} in the martensite was determined to be ~2.05Å, and the corresponding carbon

content was found to be ~0.65 wt. %. This value of carbon concentration in the martensite is slightly higher than that predicted from the Fe-C equilibrium phase diagram (~0.45 wt. %) corresponding to approximately 20 pct. volume fraction of martensite. It should be noted, however, that in general two sets of {110} lattice fringe images with different indices will be required to ascertain that at least one of them shows the tetragonality of martensite.

The principal difficulties encountered in imaging lattice fringes in martensitic steels are associated with (i) relatively small lattice spacings (largest d = 2.03Å), (ii) correction of objective astigmatism due to the magnetic field of the specimen, and (iii) very high, localized strain fields in the structure. This investigation demonstrates, however, that the lattice imaging technique can be successfully applied to the martensitic transformation in steels.

V. SUMMARY AND CONCLUSIONS

This investigation has been aimed at designing superior DFM steels which can meet today's energy and resource conservation requirements, together with the characterization of duplex microstructure-property relationships. From this study the following conclusions have been drawn:

1. DFM steel is a two phase alloy containing a controlled amount of martensite in a ferrite matrix to develop the desired combination of strength and formability. Selection principles for improved mechanical properties of DFM steels have been proposed in order to obtain desirable microstructural characteristics which in turn result in desirable mechanical properties. Design variables include martensite volume fraction, morphology and properties of the constituent phases, microstructural features, and nature of interface.

2. The alloy, of composition Fe/2% Si/0.1% C, has been selected according to the selection principles. Duplex treatment for this new steel resulted in a fine, fibrous, and discontinuous distribution of martensite particles in a ferrite matrix.

(i) Tensile test of the 2% Si DFM steel showed attractive properties, e.g. yield strength ~70 KSi, tensile strength ~112 KSi, uniform elongation ~15%, and total elongation ~25% at about 40% martensite. A wide range of desirable properties is obtainable by controlling the amount of martensite volume fraction.

(ii) These properties are superior to a series of Cr and Mn containing DFM steels, and to some selective commercial HSLA steels

including Van 80. Moreover, they already exceed the industrial goals for HSLA steels for the automobile industry.

(iii) The superior tensile properties found in the duplex 2% Si steel are attributed to silicon being one of the alloying elements which most favorably control the design variables: Promoting dislocated martensite in a fine, fibrous, and discontinuous distribution, providing solid solution strengthening in the ferrite, and improving the α/martensite interface by inhibiting the formation of coarse carbides during the final quench.

In addition Si broadens the ($\alpha + \gamma$) range when added to the Fe-C system so that small temperature variations in the two phase region do not change composition significantly, thereby assuring reproducibility of material manufacture.

3. It appears that the mechanical behavior of DFM steel is controlled by both microscopic (dislocation) and macroscopic (fiber loading) mechanisms.

4. Stress-strain characteristics of the Si containing DFM steels were as follows:

(i) Extremely high rate of work hardening in the early stage of plastic deformation ($\lesssim$ 3% elongation).

(ii) Smooth transition from elastic to plastic deformation without showing yield point phenomena.

(iii) High ratio of tensile/yield strength and good elongation to necking.

These features are indicative of excellent formability.

5. Over the range of 15~ 80% martensite the rule for two phase mixtures appears to hold as a fairly good approximation of the tensile behavior of the duplex systems.

6. It was found that the volume fraction and connectivity of martensite as well as the presence of coarse carbides near the α/martensite interface play an important role in determining tensile properties. The effects of the other design parameters could not be isolated in this investigation.

7. Tempering experiments led to the following conclusions:

(i) Yield strength of DFM structures (~25% martensite) was determined by the flow stress of the ferrite, and was not affected by the strength of martensite.

(ii) Yield strength level was maintained up to 400°C tempering for 1 hour. Tensile strength of the composite showed gradual decrease with increasing tempering temperature, but with much slower rate than that of 100% martensite.

(iii) Tempering at 200°C for 1 hour resulted in the improvement of tensile ductility without attendant loss of strength. Higher tempering temperature resulted in no further improvement in tensile properties. Above conclusions have been established from the tempered duplex microstructure-property relationships.

8. Impact properties were strongly influenced by the connectivity, carbon concentration, and volume fraction of martensite.

9. It appears that the following factors are the origin of the superior tensile properties found generally in DFM steels:

(i) High purity of ferrite matrix.

(ii) Both strong and tough martensite as a second phase constituent.

(iii) Equal elastic constants.

(iv) Good coherency at the α/martensite interface.

10. Phase transformation studies resulted in the following conclusions:

(i) The concept of a concentration "spike" at the advancing α/γ boundaries has been introduced as an explanation as to how the alloy element influences the morphology of duplex microstructural constituent in Fe/x/0.1 C alloys.

(ii) Competitive processes between the ferrite and martensite determines the tempering response of the DFM structures.

(iii) Lattice fringe imaging of the α/martensite interface revealed that {110} fringes were continuous across the interface, indicating good coherency.

(iv) It has been shown that lattice imaging technique can be successfully applied to phase transformations in steels.

VI. REMARKS

It is only in the last two years that the extremely attractive feature of DFM structures, coupled with practical feasibility and economy of production, have been realized. Consequently this has triggered intensive and ever-growing research programs. The automotive industry is especially interested in such programs since the DFM steels can help designers achieve significant fuel economies through weight reduction. In so far as broad principles have now been established, it should be possible to design DFM alloys in a considerably more precise manner. However, much more work is required to complete the picture. For instance, a variety of DFM structures can be developed using many different processing techniques (Fig. 1). Each technique and alloy composition should be looked into separately depending upon specific property requirements, manufacturing capabilities, and costs involved.

DFM structures have been shown favorable for other engineering properties such as fatigue endurance, weldability, and impact resistance. Thus it appears that the special features of DFM steels can be utilized to advantage to a much greater degree than is appreciated at this time.

ACKNOWLEDGMENTS

The author wishes to express his deep appreciation to Professor Gareth Thomas for his continued guidance, encouragment and support throughout the course of this investigation. He would like to thank Professors J. W. Morris, Jr. and S. A. Schaaf for their review and critical comments of this manuscript.

The assistance provided by the support staff of the Materials and Molecular Research Division of Lawrence Berkeley Laboratory is acknowledged. Thanks are due, in particular, to Carolyn Gosnell, Gloria Pelatowski, Lee Johnson, and Ed Edwards. Appreciation is also extended to Carmen Hubbard and Shirley Ashley for typing this manuscript. The author is also grateful to Peter Costello and Robert Drosd for manuscript arrangement. Dr. Asada and Daido Steel Company graciously supplied the alloys used in this research.

Finally, I am greatly indebted to Mr. and Mrs. Park Young-Joo for their love and support that made this work possible.

This research was done with support from the U. S. Energy Research and Development Administration.

REFERENCES

1. Processing and Properties of Low Carbon Steel, J. M. Gray, ed., AIME Proceedings of the Int'l. Symposium, Ohio, Oct. 1972.
2. Micro Alloying 75, Symposium on High Strength, Low-Alloy Steels, Washington, D. C., 1975.
3. Journal of Metals 29, No. 1, Jan. 1977.
4. R. R. Preston, J. of Metals 29, No. 1, 9 (1977).
5. Carlo Parrini et al., Micro Alloying 75, Symposium on High Strength, Low-Alloy Steels, Products and Process, p. 56, Washington, D. C., 1975.
6. S. Hayami and T. Furukawa, ibid., p. 78.
7. I. Tamura et al., Trans. Iron Steel Inst. Japan 13, 283 (1973).
8. M. S. Rashid, SAE Preprint 760206, Feb. 1976.
9. J. Y. Koo and G. Thomas, Mat. Sci. and Engr. 24, 187 (1976).
10. J. Y. Koo and G. Thomas, Met. Trans. 8A, 525 (1977).
11. R. G. Davies, Ford Research Report #SR-77-29 (1977).
12. Automotive Engineering 84, 49 (1976).
13. D. J. Bailey and R. Stevenson, Research Publication, GMR-2373, April (1977).
14. R. Stevenson, D. J. Bailey, and G. Thomas, GMR-2374, April (1977).
15. H. Carpenter and J. M. Robertson, Metals, Oxford Press, London (1939).
16. S. A. Herres and C. H. Lorig, Trans. ASM 40, 775 (1945).
17. R. L. Cairns and J. A. Charles, JISI 205, 1044 (1967).

18. R. A. Grange, Proceedings of the 2nd Int'l. Conf. on the Strength of Metals and Alloys, ASM, Pacific Grove, p. 861 (1970).

19. K. Araki, K. Nakaoka, M. Abe, and N. Ohashi, 9th Biennial Conference of IDDRG Research Group Proceedings, 39 (1976).

20. A. Kelly and G. J. Davies, Met. Rev. 10, 37 (1965).

21. P. J. E. Forsyth, Composite Materials, London Iliffe Books Ltd., p. 67 (1966).

22. E. Orowan, Nature 149, 643 (1942).

23. A. Kelly, Met. Trans. 3, 2313 (1972).

24. C. T. Liu and J. Gurland, Trans. AIME 242, 1535 (1968).

25. V. R. Riley, J. Composite Materials 2, 436 (1968).

26. A. S. Carrara and F. J. McGarry, ibid, p. 222 .

27. R. F. Decker, Met. Trans. 4, 2495 (1973).

28. L. M. Brown and R. K. Ham, Stengthening Methods in Crystals, A. Kelly and R. B. Nicholson, eds., Elsevier Publishing Co., p. 12 (1971).

29. B. A. Wilcaux and A. H. Clauer, The Superalloys, C. T. Sims and W. C. Hagle, eds., John Wiley and Sons, New York, p. 79 (1972).

30. G. C. Sih, E. P. Chen, and S. H. Huang, Engr. Fracture Mechanics 6, 343 (1974).

31. B. Karlsson and G. Lindén, Mat. Sci. and Engr. 17, 209 (1975).

32. S. D. Antolovich, A. Saxeria, and G. R. Chanani, Met. Trans. 5, 623 (1974).

33. P. L. Manganon, Jr. and G. Thomas, Met. Trans. 1, 1577 (1970).

34. B. Harris, Composites, p. 152, July (1972).

35. E. O. Hall, Proc. Phys. Soc. B64, 742 (1951).

36. W. J. Petch, Iron and Steel Institute J., London 174, 25 (1953).

37. G. Thomas, Battelle Conf. on Fundamental Aspects of Structural Alloy Design, Richland, Washington, in press, LBL-4175 (1975).

38. I. L. Mogford, Met. Rev. Review 114, 12, 49 (1967).

39. J. E. Hilliard and W. S. Owen, JISI, Nov. p. 268 (1952).

40. M. R. Plichta and H. I. Aaronson, Met. Trans. 5, 2611 (1974).

41. R. F. Hehemann, Phase Transformation, ASM, p. 410 (1970).

42. E. Piwowarsky, Hochwertiges Gußeisen, Springer-Verlag, p.52 (1951).

43. J. Chipman, Metal Handbook, ASM, 8th ed., p. 276 (1973).

44. H. I. Aaronson, Decomposition of Austenite by Diffusional Processes, V. F. Zackay and H. I. Aaronson, eds., Interscience, New York, p. 387 (1962).

45. J. W. Christian, The Theory of Transformations in Metals and Alloys, Pergamon, New York, 1965.

46. B. V. N. Rao, J. Y. Koo, and G. Thomas, 33rd Annual Proc. Electron Microscopy Soc. America, G. W. Bailey, ed., p. 30 (1975).

47. K. W. Andrews, D. Y. Dyson, and S. R. Keown, Interpretation of Electron Diffraction Patterns, Plenum Press, New York, p. 137 (1967).

48. J. Gordine and I. Codd, JISI, p.461, April (1969).

49. H. I. Aaronson and H. A. Domain, Trans. AIME 236, 871 (1966).

50. G. S. Ansell et al., Met. Trans. 2, 2443 (1971).

51. G. R. Speich and W. C. Leslie, Met. Trans. 3, 1043 (1972).

52. D. Kalish and M. Cohen, Mat. Sci. and Eng. 6, 156 (1970).

53. A. T. Davenport, F. G. Berry, and R. W. K. Honeycombe, Metal Sci. J. 2, 104 (1968).

54. K. Campbell and R. W. K. Honeycombe, Metal Sci. 8, 197 (1974).

55. W. B. Morrison, JISI 201, 317 (1963).

56. M. Tanino and K. Aoki, Trans. Iron Steel Inst. Japan 8, 339 (1968).

57. The Making, Shaping, and Treating of Steel, H. E. McGannon, ed., 9th edition, p. 1132 (1971).

58. D. J. H. Cockayne, Z. Naturforsch 27a, 452 (1972).

59. D. J. H. Cockayne, I. L. F. Ray, and M. J. Whelan, Phil. Mag. 20, 1265 (1969).

60. B. Karlson and G. Lindén, Mat. Sci. and Engr. 17, 153 (1975).

61. H. I. Aaronson, H. A. Domian, and G. M. Pound, Trans. AIME 236, p. 753, ibid. p. 768 (1966).

62. H. W. Paxton, Transformation and Hardenability in Steels, Climax Molybdenum Co., Ann Arbor, Mich. p. 39 (1967).

63. G. R. Speich and A. Szirmae, Trans. AIME 245, 1063 (1969).

64. G. A. Roberts and R. F. Mehl, Trans. ASM 31, 613 (1943).

65. R. R. Judd and H. W. Paxton, Trans. AIME 242, 206 (1968).

66. A. E. Nehrenberg, Trans. AIME 188, 162 (1950).

67. A. Goldberg, Trans. ASM 61, 26 (1968).

68. J. D. Grazier, H. W. Paxton, and W. W. Mullins, Trans. AIME 233, 130 (1965).

69. V. D. Sadovskii, Probl. Metallog. and Heat Treatment, p. 31 (1956).

70. M. J. Young, Master Thesis, University of California, Berkeley, LBL-6620 (1977).

71. M. Hillert, Acta Met. 3, 34 (1955).

72. L. S. Darken, Trans. AIME 221, 654 (1961).

73. J. S. Kirkaldy, Can. J. Phys. 36, 907 (1958).

74. L. S. Darken, Atom Movements, ASM Metal Park, Ohio, p. 1 (1951).

75. K. J. Ivine and F. B. Pickering, JISI 201, 944 (1963).

76. P. Gordon and R. A. Vandermeer, Recrystallization, Grain Growth and Textures, ASM, Metals Park, Ohio, p. 118 (1957).

77. K. R. Kinsman and H. I. Aaronson, Met. Trans. 4, 959 (1973).

78. L. C. E. Geniets and J. F. Knott, Metal Sci. J. 6, 69 (1972).

79. G. Clark, R. O. Richie, and J. F. Knott, Nature Physical Science 239, 104 (1972).

80. W. S. Owen, Trans. ASM 46, 812 (1954).

81. J. Nutting, JISI 207, 872 (1969).

82. G. R. Speich, Trans. AIME 245, 2553 (1969).

83. R. W. K. Honeycombe, Structure and Strength of Alloy Steels, Climax Molybdenum Co. Ann Arbor, Mich. (1974).

84. A. G. Alten and P. Payson, Trans. ASM 45, 498 (1953).

85. H. W. King and S. G. Glover, JISI, p. 281, Nov. (1960).

86. C. J. Altstetter et al., Trans. ASM 55, 287 (1962).

87. B. G. Reisdorf, Trans. AIME 227, 1334 (1963).

88. M. S. Bhat, Ph.D. Thesis, University of California, Berkeley, LBL-6046, Feb. (1977).

89. D. A. Leak and G. M. Leak, JISI, 189 (1958).

90. B. Karlsson and B. O. Sundstrom, Mat. Sci. Engr. 16, 161 (1974).

91. G. S. Ansell and F. V. Lenel, Acta Met. 8, 612 (1960).

92. R. Kossowsky and N. Brown, Trans. AIME 233, 1389 (1965).

93. E. Orowan, Discussion in Symposium on Internal Stresses in Metals and Alloys, Inst. of Metals, London, p. 451 (1948).

94. M. F. Ashby, Strengthening Methods in Crystals, A. Kelly and R. B. Nicholson, eds., Elsevier Publishing Co., p. 137 (1971).

95. T. C. Lindley, G. Oates, and C. E. Richards, Acta Met. 18, 1127 (1970).

96. D. V. Wilson, Trans. ASM, 47, 321 (1955).

97. A. Kelly, Composite Materials, London Iliffe Books, LTD p. 1 (1966).

98. G. R. Speich and W. C. Leslie, Met. Trans. 4, 1873 (1974).

99. H. Fischmeister, J.-O. Hjalmered, B. Karlsson, G. Lindén, and B. Sundstrom, The Microstructure and Design of Alloys, Proc. 3rd. Int'l. Conf. on Strength of Metals and Alloys, P.621, Inst. of Metals and Iron Steel Inst., London (1973).

100. H. C. Fiedler, JISI 205, 158 (1967).

101. J. M. Capus and G. Mayer, JISI, p. 149, Oct. (1960).

102. T. C. Lindley and C. E. Richards, Metal Sci. J. 4, 81 (1970).

103. C. J. McMahon and M. Cohen, Acta Met. 13, 991 (1965).

104. T. Kunio, M. Shimizu, K. Yamada, and H. Suzuki, Engr. Fracture Mechanics 7, 411 (1975).

105. W. B. Morrison and R. L. Miller, Strengthening Mechanisms, 12th Sagamore Army Materials Research Confernece, p. 183 (1965).

106. J. M. Cowley and S. Iijima, Electron Microscopy in Mineralogy, H.-R. Wenk, ed., Springer-Verlag, Berlin, p. 123 (1976).

107. R. Sinclair, R. Gronsky, and G. Thomas, Acta Met. 24, 789 (1976).

108. D. R. Clarke, Nitrogen Ceramics, F. Riley, ed., Proc. of a NATO Advance Summer Institute on Nitrogen Ceramics, In press (1976).

109. G. Thomas, J. of Metals 29, 31 (1977).

110. R. Gronsky, Ph.D. Thesis, University of California, Berkeley, LBL-5784, Dec. (1976).

111. P. B. Hirsch, et al., Electron Microscopy of Thin Crystals, p. 169 (1965).

112. B. D. Cullity, Elements of X-Ray Diffraction, p. 485 (1967).

113. Annual Book of ASTM Standards, Designation E8-69, p. 196 (1973).

114. ibid, Designation E23-72, p. 277.

115. E. E. Underwood, Metals Engr. Quart. 1, 70 (1961).

116. K. Uchida, K. Araki, and S. Fukunaka, United States Patent, #3936324 (1976).

117. K. Nakaoka, K. Araki, and O. Kimpara, Sosei To Kako 17, No. 190, 875 (1976).

118. K. Araki, S. Fukunaka, and K. Uchida, Technical Research Publication, Nippon Kokan K. K. (1977).

TABLE I. ALLOY COMPOSITIONS AND M_s, M_f, A_s, A_f TEMPERATURES

Alloy Number	Fe	C	Cr	Si	Measured (°C)			
					M_s	M_f	A_s	A_f
2	Bal.	0.06	0.49	----	550	446	755	910
1	Bal.	0.07	2.02	----	450	350	755	890
5	Bal.	0.073	4.00	----	440	320	755	810
6	Bal.	0.075	----	0.49	560	480	740	930
4	Bal.	0.065	----	2.02	555	480	742	1020

TABLE II. ANNEALING TEMPERATURES IN THE ($\alpha + \gamma$) RANGE.

Specimen Designation	Volume Pct. Martensite	2	1	5	6	4
S1	20	815	815	812	850	950
S2	40	860	830	817	880	990
S3	60	880	850	822	910	1015

TABLE III. TENSILE TEST SUMMARY (UNTEMPERED).

Specimen†	% Martensite	YS (KSi)	UTS (KSi)	e_u% (uniform)	e_T% (total)	R.A. (%)
2A*	100	113	134	3	15	74
2S1**	15	47	79	15	24	58
2S2	35~40	63	93	11	22	74
2S3	65	79	101	6	19	79
1A	100	110	132	5	11	41
1S1	20~25	62	93	12	20	38
1S2	60	69	101	9	14	34
1S3	85	80	116	7	11	37
5A	100	130	156	4	15	67
5S1	30	61	87	7	13	46
5S2	40	66	98	6	11	36
5S3	55~60	73	109	6	10	30
6A	100	135	160	4	10	59
6S1	15~20	61	95	14	25	66
6S2	40~45	68	102	12	23	69
6S3	70	77	105	10	21	67
4A	100	128	154	5	15	60
4S1	25~30	63	109	17	27	60
4S2	35~40	70	112	15	25	59
4S3	45~50	78	121	14	23	59

* "A" refers to the initial martensitic microstructure.

** "S" refers to the specimen given two phase annealing.

† The numbers preceding the letters pertain to the alloy numbers.

TABLE IV. TENSILE TEST SUMMARY

(TEMPERED 100% MARTENSITE)

Specimen*	Tempering Temperature(°C)	YS (ksi)	UTS (ksi)	e_u(%) (uniform)	e_T% (total)
2A	AQ				
2AT1	200	134	158	2.5	11
2AT2	400	121	131	2	13
2AT3	600	72	83	7	20
5A	AQ				
5AT1	200	140	171	2.5	11
5AT2	400	135	156	2	11
5AT3	600	88	101	5	18
6A	AQ				
6AT1	200	137	165	3.5	13
6AT2	400	112	123	4	16
6AT3	600	72	85	9	20
4A	AQ	141	173	5	13
4AT1	200	139	170	4	12
4AT2	400	133	148	4	15
4AT3	600	86	102	13	25

* The numbers preceeding letters denote alloy numbers.

TABLE V. TENSILE TEST SUMMARY

(TEMPERED DUPLEX STRUCTURE)

Specimen	% Martensite	Tempering Temp. (°C)	YS (ksi)	UTS (ksi)	e_u (%)	e_T (%)	R.A. (%)
2S	35~40	AQ	65	92	10	22	72
2ST1		200	62	85	10	23	77
2ST2		400	60	79	8	23	82
2ST3		600	46	62	13	29	87
5S	30	AQ	59	87	8	13	42
5ST1		200	68	93	5	11	43
5ST2		400	51	76	8	17	57
5ST3		600	48	67	11	27	85
6S	70	AQ	75	117	10	19	
6ST1		200					
6ST2		400	54	82	11	26	
6ST3		600	47	70	17	29	
4S	30	AQ	65	110	16	23	59
4ST1		200	59	103	17	30	70
4ST2		400	60	96	16	28	73
4ST3		600	56	76	17	30	77

TABLE VI. CHARPY IMPACT PROPERTIES

($\frac{3}{4}$ SUBSIZE SPECIMEN)

Duplex Alloys	Vol. Pct. Martensite	Testing Temperatures (°C)				
		-75	-50	-20	0	24
2S	35	1.8 ± 0.5	2.2 ± 0.0	3.0 ± 0.1	3.5 ± 0	4.3 ± 0.2
	90	3.2 ± 0.0	3.5 ± 0.2	4.2 ± 1.0	9.2 ± 0.3	9.5 ± 0.5
6S	30~35	2.0 ± 0.1	3.6 ± 0.3	4.5 ± 0.3	7.8 ± 0.4	16.4 ± 2.2
	60	3.0 ± 0.4	4.0 ± 1.0	5.5 ± 0.4	16.0 ± 1.1	20.2 ± 1.3
4S	30~35	2.2 ± 0.4	3.2 ± 0.4	4.4 ± 0.6	7.3 ± 0.4	17.0 ± 2.0
	60	2.4 ± 0.1	2.9 ± 0.1	4.0 ± 0.4	7.0 ± 1.5	15.0 ± 3.0

TABLE VII.

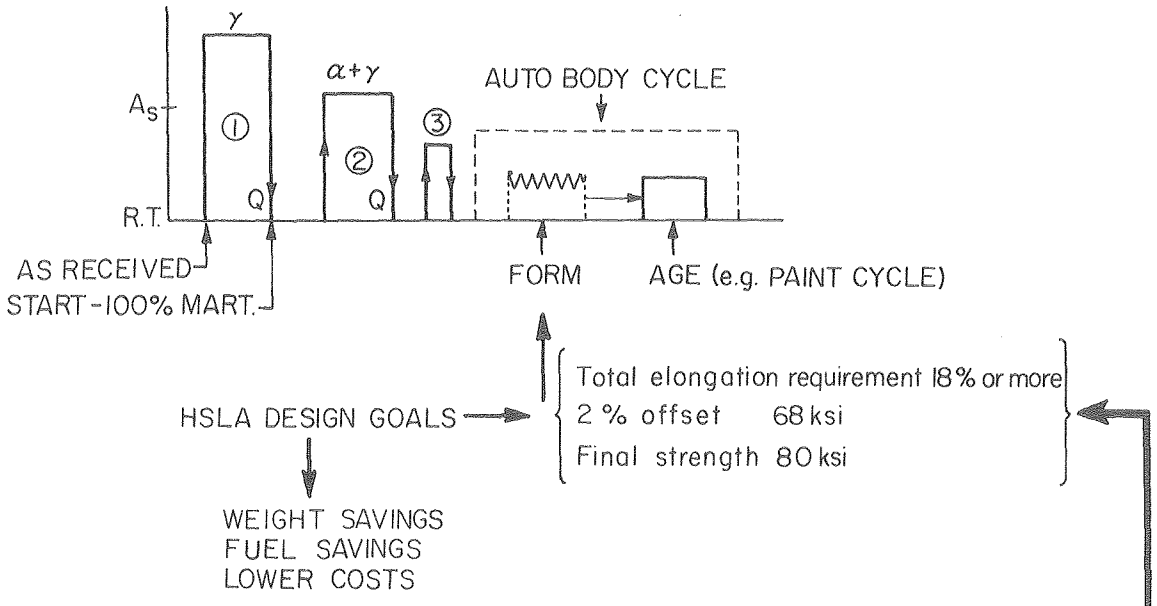

NEW STEEL Fe/2 % Si/0.1 % C[(1)]

M_S: 555 °C, A_S: 742 °C, A_f: 1020 °C

Treatment	% M_S	Y. S. ksi	U.T.S. ksi	% Unif. El.	% Tot. El.	R.A.
① A.Q.	100	128	154	5	15	60
① + ②	25-30	63	109	17	27	60
"	35-40	70	112	15	25	59
"	45-50	78	121	14	23	53
①+②+③ (200°)	30	59	103	17	30	70

(1) No alloy carbide formers ∴ HSLA not needed

XBL 761-6303

FIGURE CAPTIONS

Fig. 1. Schematic diagram of many different ways of heat treatment to produce controlled DFM structures.

Fig. 2. (a) Schematic diagram showing orientation of Charpy impact specimen in the forged plate. (b) Sketch of dilatometer specimen.

Fig. 3. Schematic representation of duplex treatment used in this investigation.

Fig. 4. Optical micrographs of the initial martensitic structures. (a) Cr steels, and (b) Si steels.

Fig. 5. Optical micrograph of DFM structures developed in alloy 2 (Fe/0.5 Cr/0.1 C).

Fig. 6. Optical micrograph of DFM structures developed in alloy 5 (Fe/4 Cr/0.1 C). (a) Early stage structure and (b) late reaction time structure.

Fig. 7. Optical micrograph of DFM structure developed in alloy 4 (Fe/2% Si/0.1 C).

Fig. 8. Transmission electron micrographs revealing interlath retained austenite in the 100% martensite structures. (a) Bright field image. (b) Retained austenite reversed contrast in dark field image. (c) Selected area diffraction (SAD) pattern of (a). (002) spot was imaged for dark field (b). (d) Indexing of the diffraction pattern in (c), showing K-S orientation relationship, $\langle 111 \rangle_{\alpha} // \langle 110 \rangle_{\gamma}$. This particular micrographs were obtained from 2% Si steel, but morphology of the retained austenite was similar in all the alloys.

Fig. 9. Another area of the initial martensite structure (a), showing retained austenite trapped between two martensite laths in (b).

Fig. 10. Bright field (a) and dark dirld (b) of retained austenite in the 100% martensite of specimen 2. SAD of (a) is shown in (c), where $(2\bar{2}0)_{\gamma}$ spot used for dark field is marked by the image of objective aperture. Indexing of SAD reveals the N-W orientation relationship between BCC and FCC.

Fig. 11. Bright field (a) and dark field (b) of auto-tempered carbides in specimen 5A (fully martensitic 4 Cr steel). Dark field (b) obtained by $(\bar{2}10)$ carbide spot reverses contrast of carbides. (c) SAD of (a). (d) The carbides were identified as cementite (Fe_3C) by indexing of diffraction pattern (c).

Fig. 12. Bright field (a) and dark field (b) of auto-tempered carbides in specimen 2A.

Fig. 13. Morphology of auto-tempered carbides observed in specimen 4A (100% martensite). (a) Bright field image and (b) dark field image of carbides (Fe_3C).

Fig. 14. Typical twinned area in the martensite phase of Cr containing DFM steels (~ 20% martensite). (a) Bright field and (b) dark field image of the twins. (c) SAD of (a). (d) Indexed diffraction pattern. $(101)_T$ spot was used for imaging dark field (b).

Fig. 15. Martensite region showing an area of internal microtwins in the 2% Si DFM steel. (a) Bright field, and (b) dark field image showing reversal of twin contrast. (c) SAD of (a). The streaks in the diffraction pattern are due to extremely thin layers of the microtwins. (d) Indexing of diffraction pattern (c) identifies the twin spots.

Fig. 16. Composite electron micrographs showing extensive auto-tempered carbides in the martensite constituents of the 0.5 Cr DFM steel. (a) Bright field and (b) dark field of the carbides. Matrix image is also shown in the dark field image since a carbide spot superimposed with a matrix spot was imaged.

Fig. 17. Auto-tempered carbides in the martensite phase of DFM steels. (a) DFM alloy 4. (b) DFM alloy 6. α/martensite interfaces are shown in both bright field micrographs.

Fig. 18. Dislocation substructures in ferrite regions of Cr DFM steels. (a) Dislocations rearranged to form sub-boundaries. (b) Another ferrite region showing high dislocation density. The fresh dislocations in (b) were generated by the $\gamma \rightarrow$ martensite transformation strain during the final quench. Nearby martensite island is also visible.

Fig. 19. Transmission electronmicrographs showing fibrous DFM structures developed in the 2 pct Si steel. In both micrographs (a) and (b), two parallel needles are martensite phase surrounded by ferrite with a high density of dislocations.

Fig. 20. Morphology of heavy precipitation of carbides in the immediate vicinity of α/martensite boundaries in 1010 steel. The similar type of eutectioid transformation product was observed only in DFM alloys 2 and 6. (a) Bright field and (b) dark field of the carbides. (c) Bright field image showing interface precipitation morphology. (d) Bright field image of fibrous morphology of the carbides.

Fig. 21. Similar type of carbides as in Fig. 20. (a) Bright field and (b) dark field image of the carbides observed in DFM alloy 6. (c) Bright field and (d) dark field of the carbides in DFM alloy 2.

Figs. 22-32. Transmission electron micrographs of tempered DFM structures.

Fig. 22. (a) Bright field and (b) dark field pair showing precipitation of coarse carbides in a ferrite region of the 0.5 Cr DFM steel tempered at 200° C for 1 hour. (c) SAD of (a). (d) The coarse carbides, ~ 170 Å wide and ~ 1500 Å long were identified as cementite by indexing diffraction pattern.

Fig. 23. Bright field (a) and dark field (b) of the carbides present in a ferrite region of the 2% Si DFM alloy after tempering at 200° C for 1 hour. The carbides were identified as cementite.

Fig. 24. Transmission electron micrograph of a ferrite region in the 0.5 Cr DFM steel after 200° C tempering for 1 hour, showing finely dispersed precipitation on dislocations and at sub-boundaries. (a) Bright field image does not clearly resolve the fine scale precipitates. However, weak beam image (b) shows greatly improved resolution of the heterogeneous precipitation on dislocations and at sub-boundaries. (g, 3g) weak beam imaging condition was used ((a) inset).

Fig. 25. The same as Fig. 24, but in the 2% Si DFM steel.

Fig. 26. Martensite region showing carbide precipitation in the 2% Si DFM steel after tempering at 200° C for 1 hour.

Fig. 27. Transmission electron micrograph of a ferrite region in the 0.5 Cr DFM steel after 400° C tempering for 1 hour. The same explanation as in Fig. 24 is applied here for the bright field (a) and weak beam image (b). Note that, after 400° C tempering for an hour, the fine scale precipitation on dislocations is still visible in the weak beam picture. The same morphology of the ferrite matrix was observed in the 2% Si DFM alloy.

Fig. 28. Transmission electron micrograph of a martensite region in contact with ferrite matrix, tempered at 400° C for 1 hour (specimen 2ST2). Bright field (a) and corresponding dark field (b) pictures illustrate the precipitation of spheroidized carbides along α/martensite and lath boundaries. (c) SAD of (a). (d) Indexed diffraction pattern identifies the carbides as cementite.

Fig. 29. Composite electron micrograph showing extensive precipitation of carbides observed in specimen 4ST2. (a) Bright field and (b) dark field pictures. Corresponding SAD and indexing were the same as in Fig. 28.

Fig. 30. DFM structures tempered at 600° C for 1 hour (specimen 2ST3). Bright field (a) and dark field (b) pair showing precipitation of large carbides only in the martensite regions. (c) SAD of (a). (d) Indexed diffraction pattern identifying the carbides

as cementite. "F"-ferrite matrix. "M"-previous martensite region.

Fig. 31. Bright field (a) and dark field (b) pictures observed in specimen 4ST3, showing large, spheroidized carbides in the martensite region.

Fig. 32. Morphology of the ferrite regions observed in specimen 2ST3. Bright field (a) and corresponding weak beam image (b). (c) and (d) Other areas showing large subgrain sizes.

Fig. 33. Yield and ultimate tensile strengths as a function of martensite volume fraction for the DFM steels.

Fig. 34. Uniform and total elongations as a function of martensite volume fraction for the DFM steels.

Fig. 35. Strength versus uniform elongation is plotted for the DFM Fe/X/0.1 C alloys. Depending on the annealing temperature in the $(\alpha + \gamma)$ range, various volume fractions of martensite and a wide range of strength and elongation combinations are obtained.

Fig. 36. Tensile properties of the duplex 2 pct Si steel are compared with those of commercial HSLA steels.

Fig. 37. Reduction in area as a function of martensite volume fraction for the DFM alloys.

Fig. 38. Plot of 0.2 pct offset yield strength and ultimate tensile strength versus tempering temperature for the 100% martensite structures.

Fig. 39. Plot of uniform and total elongations vs. tempering temperature for the 100% martensite structures.

Fig. 40. Ultimate tensile strength and 0.2 pct offset yield strength as a function of tempering temperature for the DFM steels.

Fig. 41. Uniform and total elongation as a function of tempering temperature for the DFM steels.

Fig. 42. Reduction in area as a function of tempering temperature for the DFM steels.

Fig. 43. Three-fourth subsize CVN impact energy as a function of testing temperature for 0.5 Cr DFM steel containing 35% and 90% martensite volume fraction.

Fig. 44. Three-fourth sub size CVN impact energy as a function of testing temperature for the 0.5% and 2% Si DFM steels containing 30% and 60% martensite.

Fig. 45. Comparison of 3/4 subsize Charpy impact properties of the DFM alloys 2 and 4, each having 35% martensite.

Fig. 46. Scanning electron fractographs. (a) Broken tensile specimen of DFM alloy 6 (25% martensite). (b) Magnified view of (a), showing dimpled rupture. (c) CVN impact specimen of the 100% martensite in specimen 2A. (d) Magnified view of (c), showing quasi-cleavage like fracture mode.

Fig. 47. Scanning electron fractographs in comparison with an optical micrograph observed in 4 Cr DFM steel (a) Optical micrograph showing the distribution of martensite particles primarily along the prior γ grain boundaries. (b) Fracture surface of the standard CVN impact specimen. The areas marked as "A" appear to correspond to the martensite regions. (c) Magnified view of the ductile fracture area in (b). (d) Magnified view of the quasi-cleavage area ("A") in (b).

Fig. 48. Scanning electron fractographs of fractured standard CVN impact specimen of the Si containing DFM steels. (a) Lower magnification view, showing predominantly quasi-cleavage fracture appearance. (b) Magnified view of (a).

Fig. 49. Scanning electron fractographs of broken standard CVN impact specimen of 0.5 Cr DFM steel. Lower magnification (a) and higher magnification (b) pictures reveal the presence of small particles on the bottom of the dimples. These particles were also observed in DFM alloy 6.

Fig. 50. Scanning electron fractograph of broken subsized CVN impact specimen of DFM alloy 2 having 90% martensite. (a) Tested at 0° C. (b) Tested at -20° C.

Fig. 51. Scanning electron fractographs of broken subsized CVN impact specimen of DFM alloy 4 having 30% martensite. (a) Lower magnification and (b) higher magnification view, tested at room temperature. Arrows indicate the shallow dimples.

Fig. 52. Load-elongation (engineering stress-engineering strain) curves for the 2 pct DFM alloy with varying amount of martensite volume fraction (20, 40, and 60%), specimen 4A having 100% martensite, and Van 80.

Fig. 53. Load-elongation curves for the DFM alloys 2 and 5 containing varying amount of martensite volume fraction.

Fig. 54. Phase diagrams showing the expansion of the ($\alpha + \gamma$) range when silicon is added to the Fe-C system.

Fig. 55. (a) {110} lattice fringe image of microtwins in the 2% Si DFM steel and indexed diffraction pattern (inset) with objective aperture image encircling matrix spots and a twin reflection. (b) Conventional bright field image of the area corresponding to (a). The circle indicate the area where intermediate aperture was placed. (c) (110) lattice fringes across a martensite lath boundary. The arrows indicate the boundary.

Fig. 56. (110) lattice fringe image across a martensite lath boundary which is inclined with respect to the incident beam.

Fig. 57. Conventional bright field (a) and lattice image (b) of a α/martensite interface in the 2% Si DFM steel. The lattice image (b) was taken from the area encircled in (a). Martensite tetragonality creates the larger d_{101} spacing in the martensite region (M). "F"-ferrite. The arrows indicate the interface.

Fig. 58. Optical diffraction patterns from the ferrite (α), martensite, and α/martensite interface, showing the tetragonality of martensite.

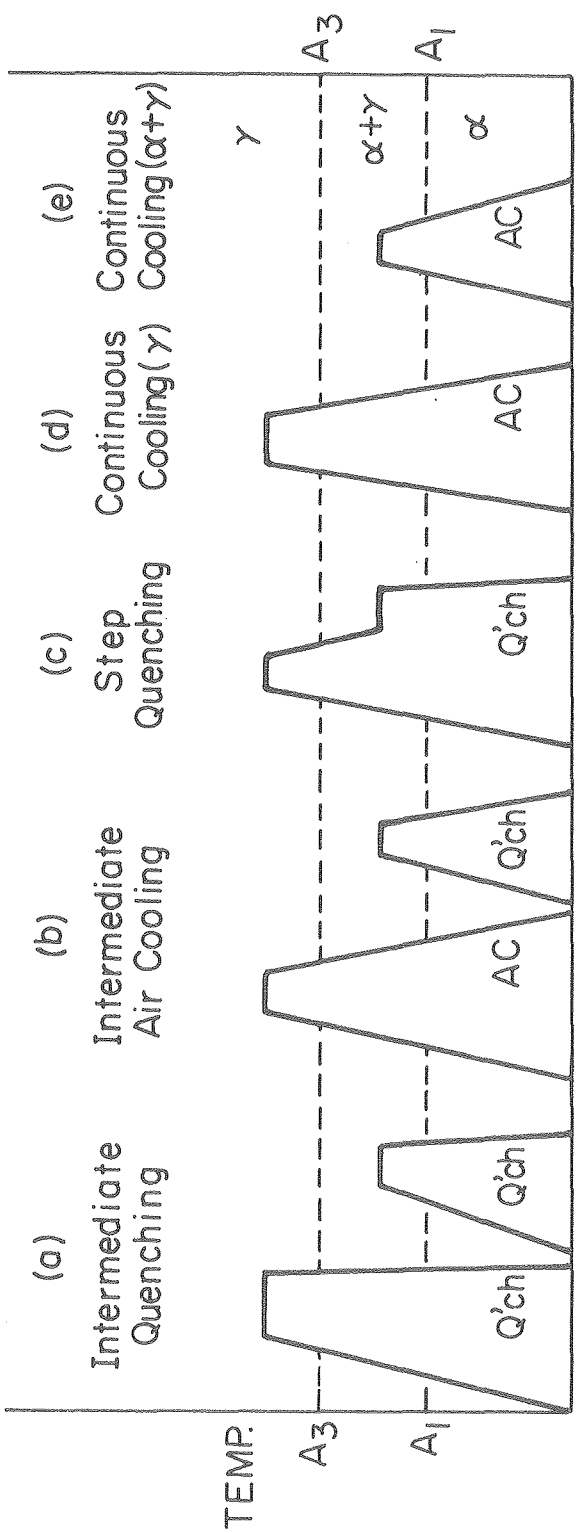

XBL 777-5863

Figure 1

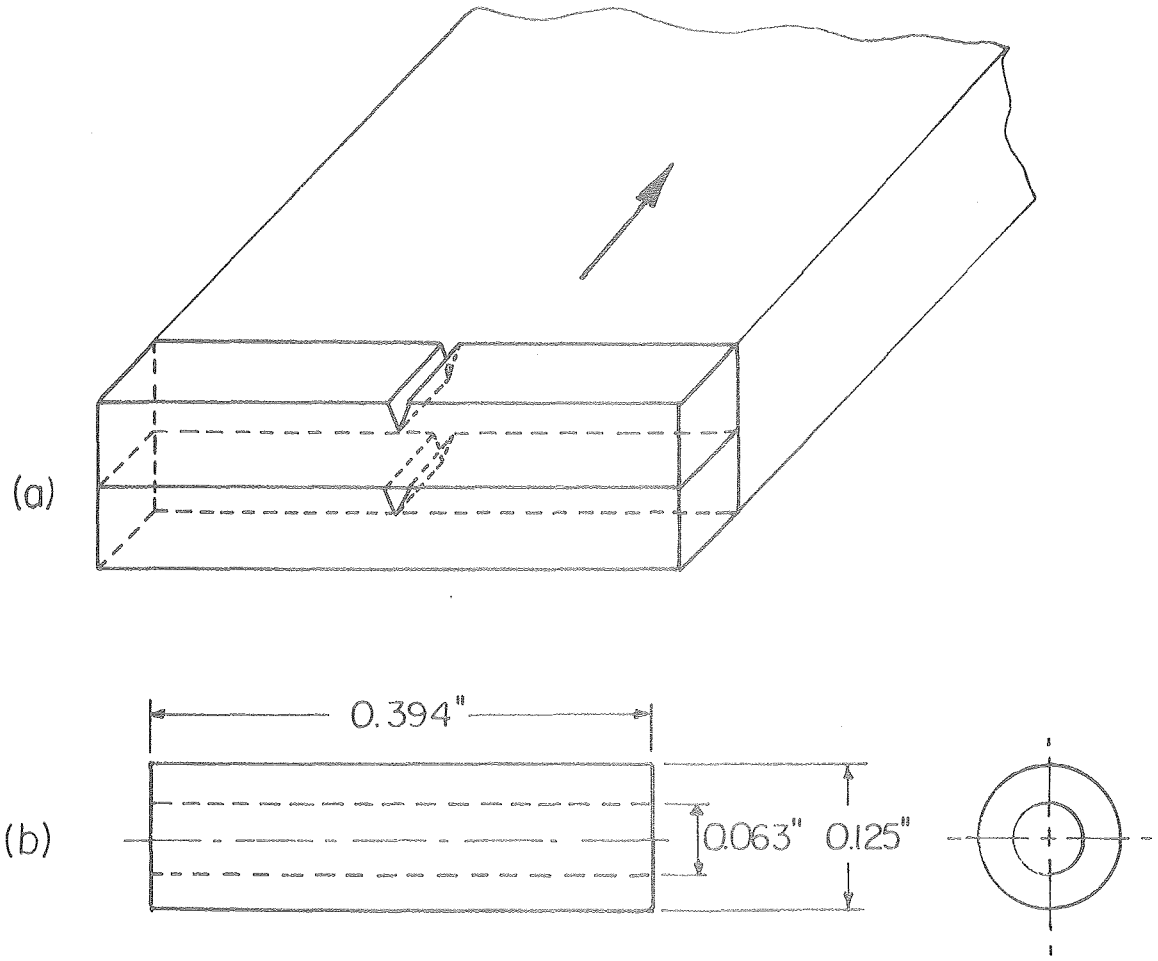

XBL 7 77-5864

Figure 2

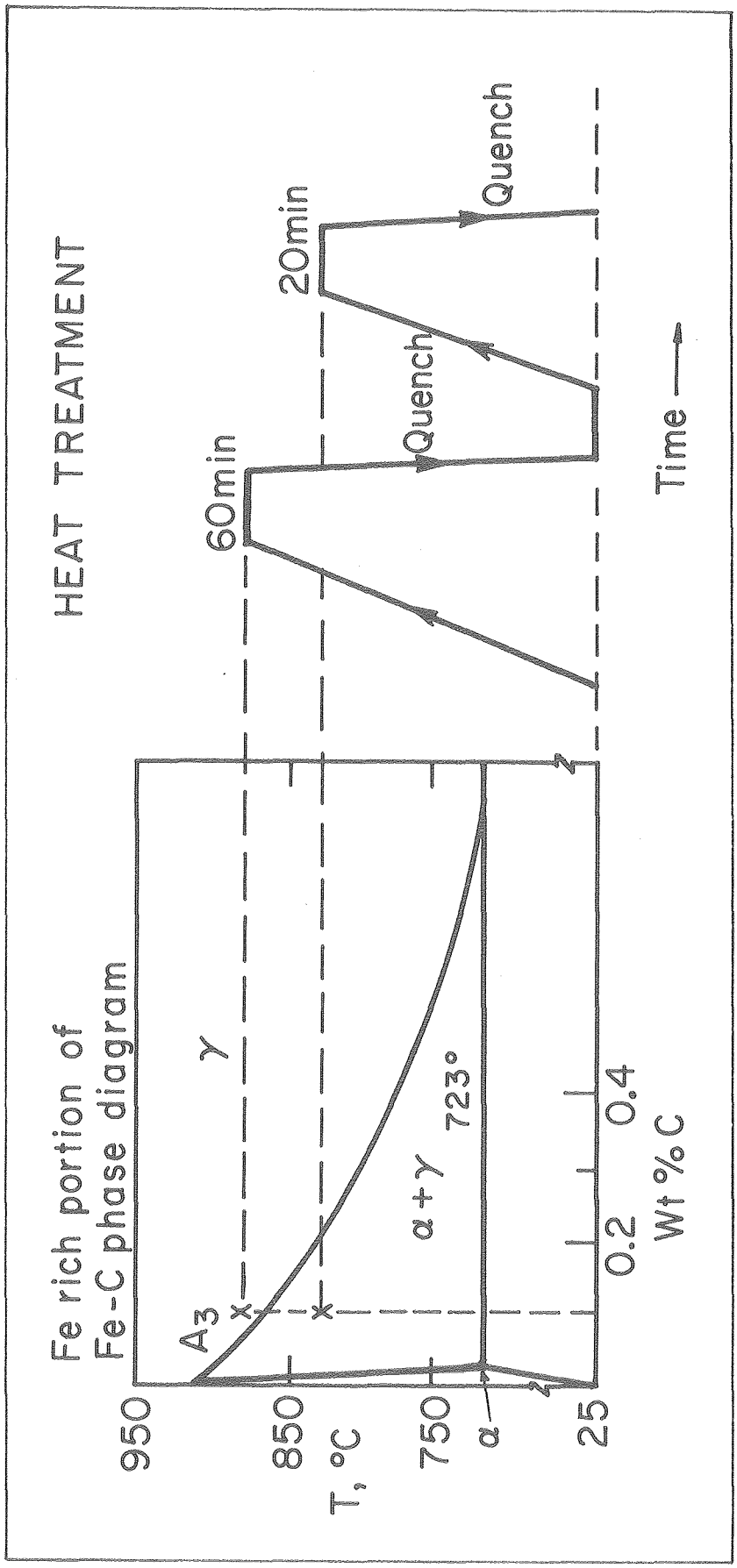
HEAT TREATMENT
Fe rich portion of
Fe-C phase diagram
γ
A3
α + γ
723°
α
950
850
750
25
T, °C
0.2
0.4
Wt % C
60min
20min
Quench
Quench
Time
XBL766-9070

Figure 3

Figure 4

Figure 5

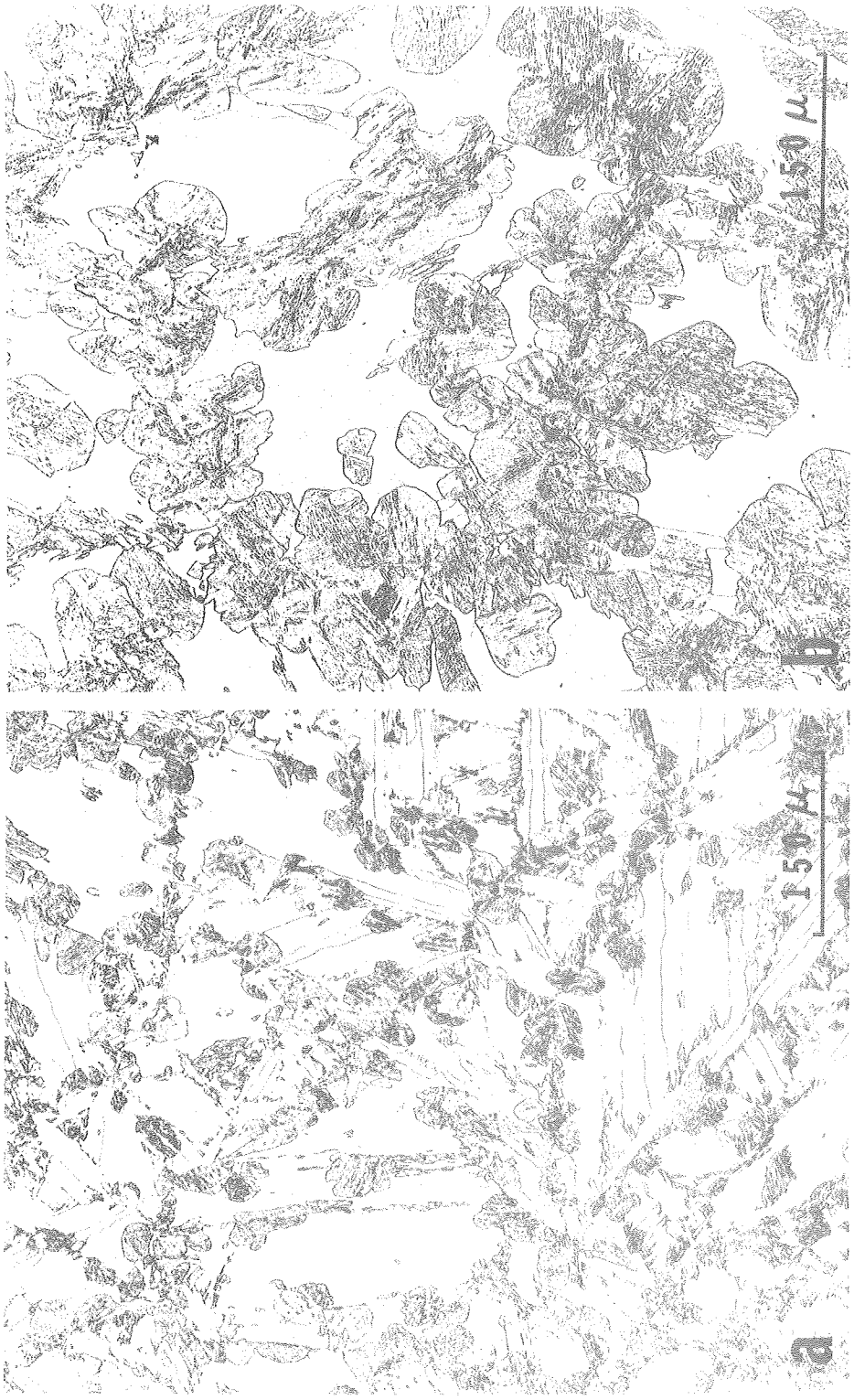

XBB 778-7535

Figure 6

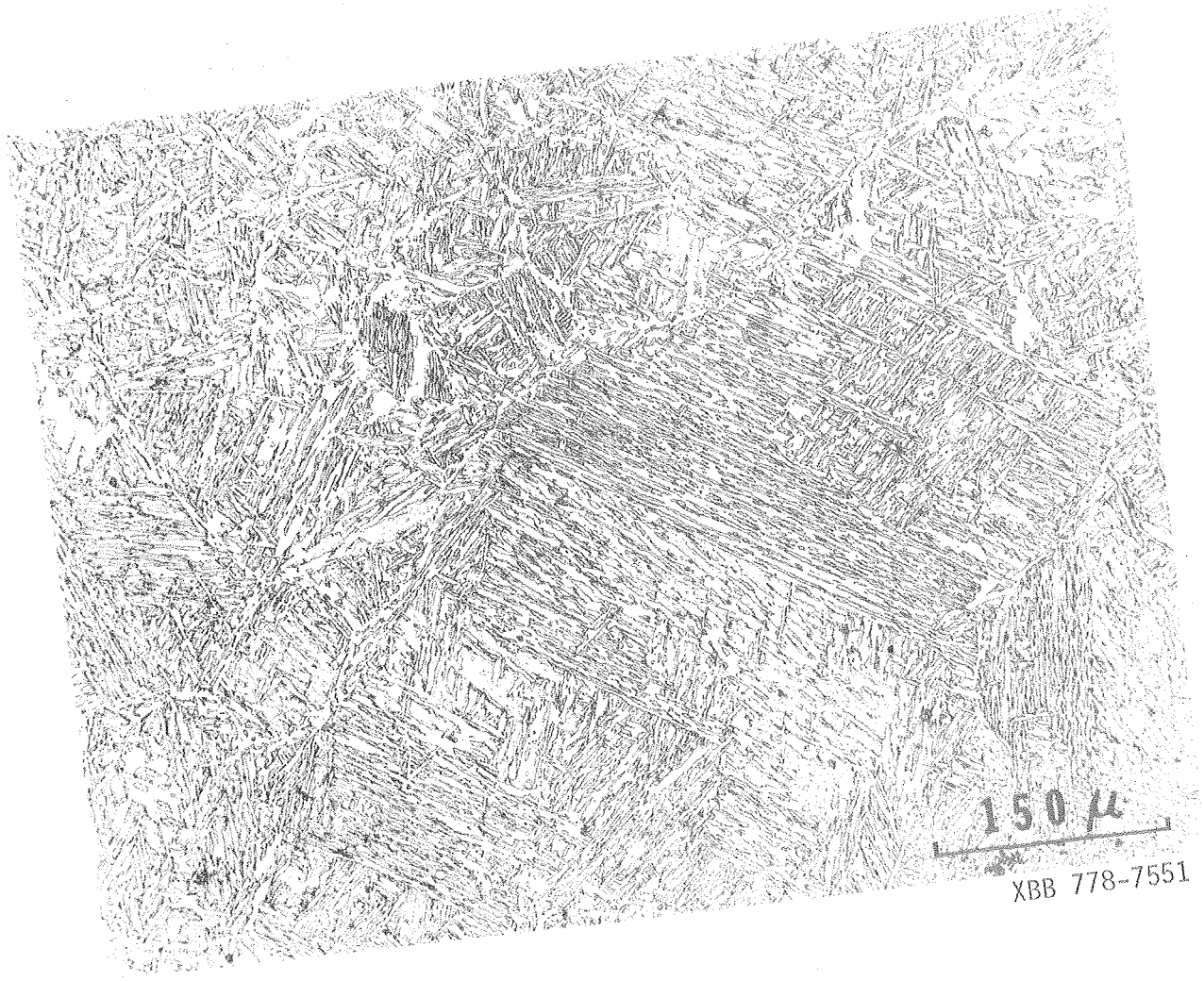

Figure 7

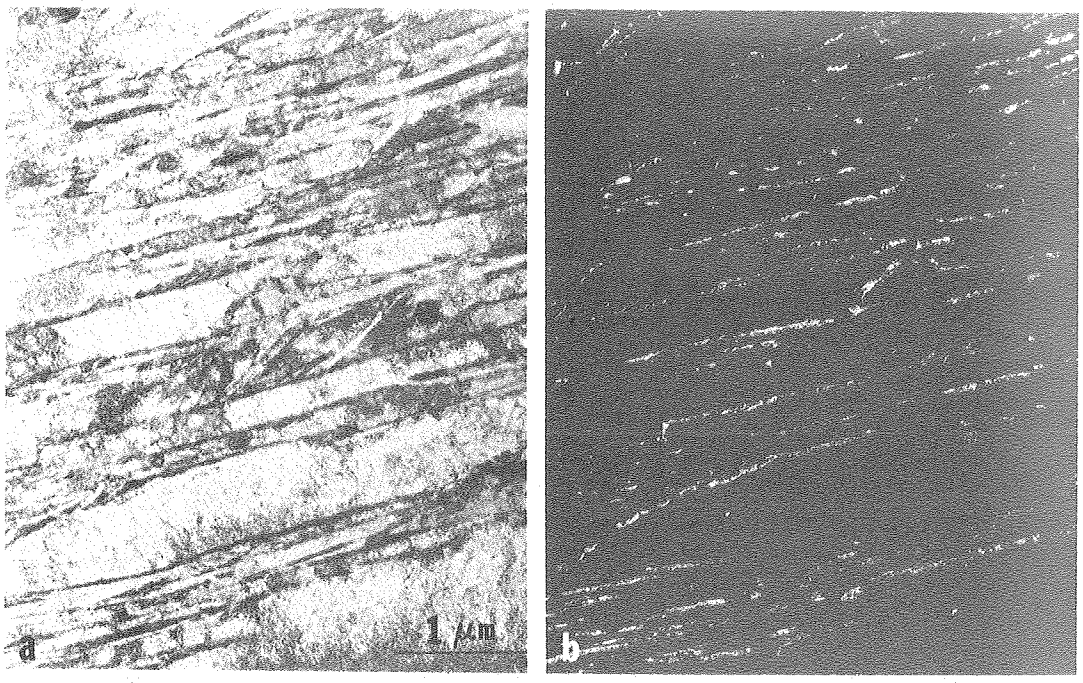

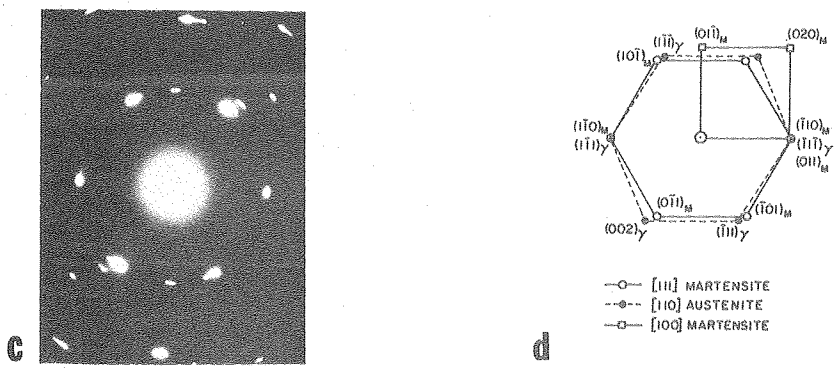

XBB 778-7561

Figure 8

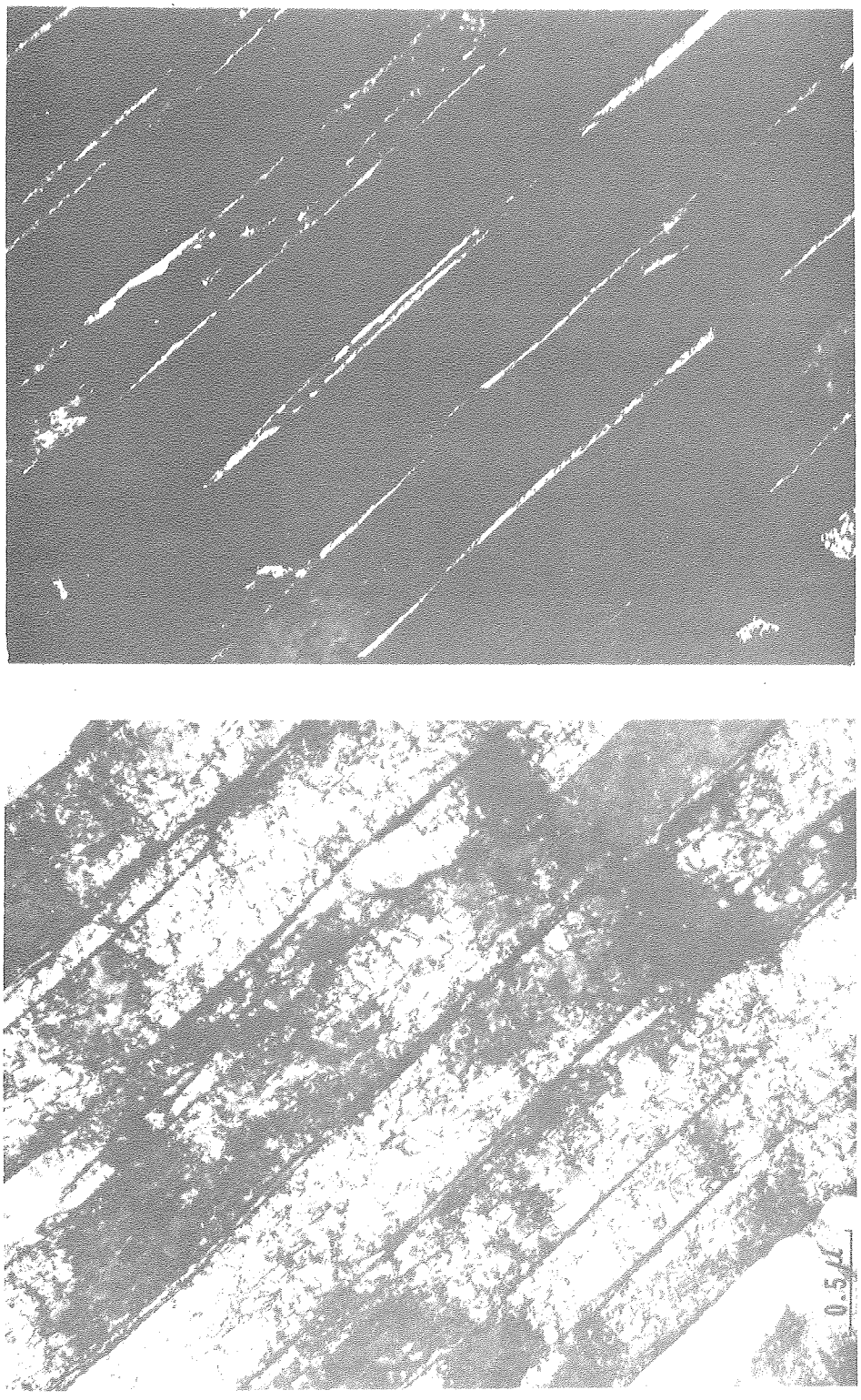

Figure 9

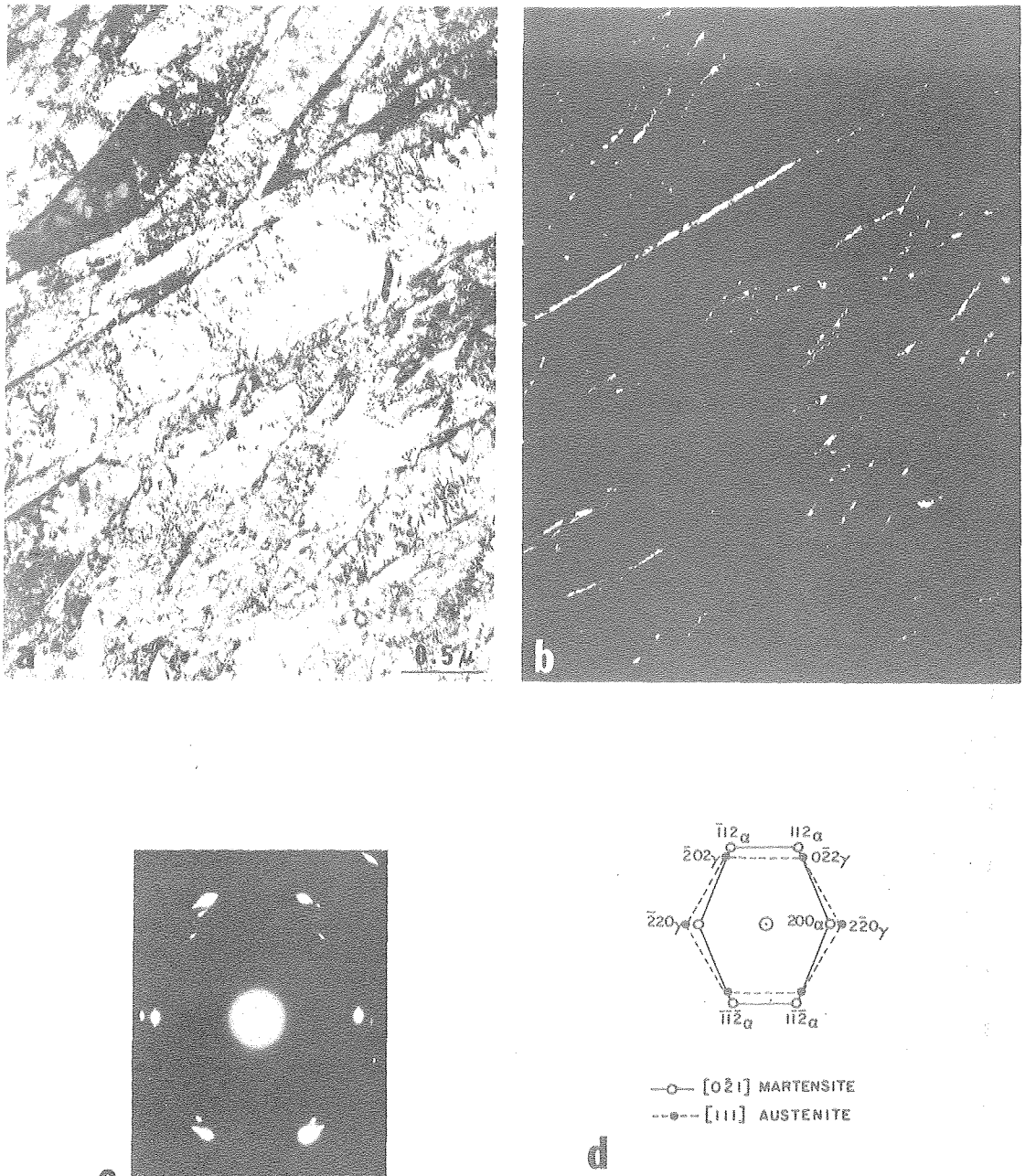

XBB 778-7538

Figure 10

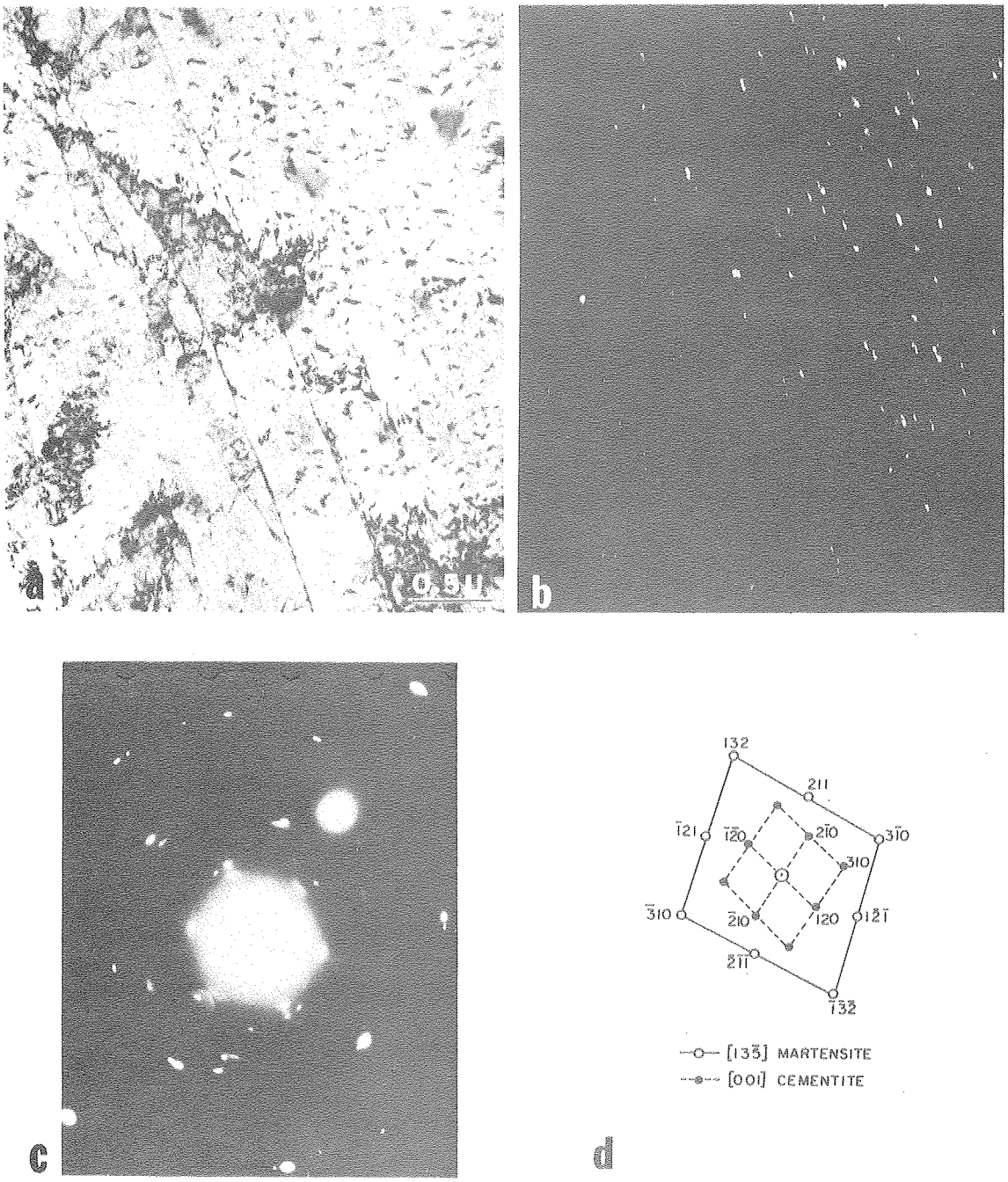

XBB 778-7539

Figure 11

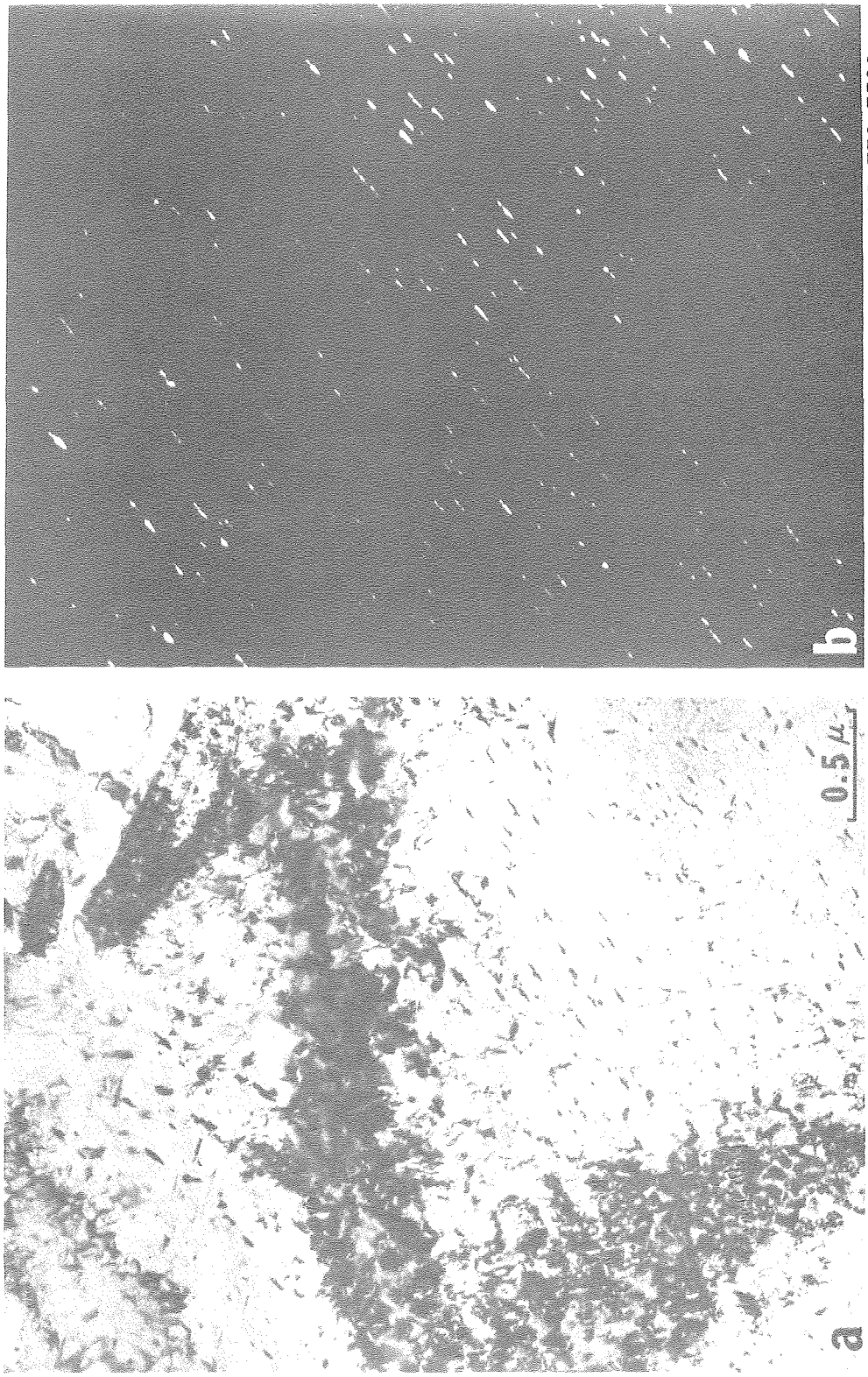

Figure 12

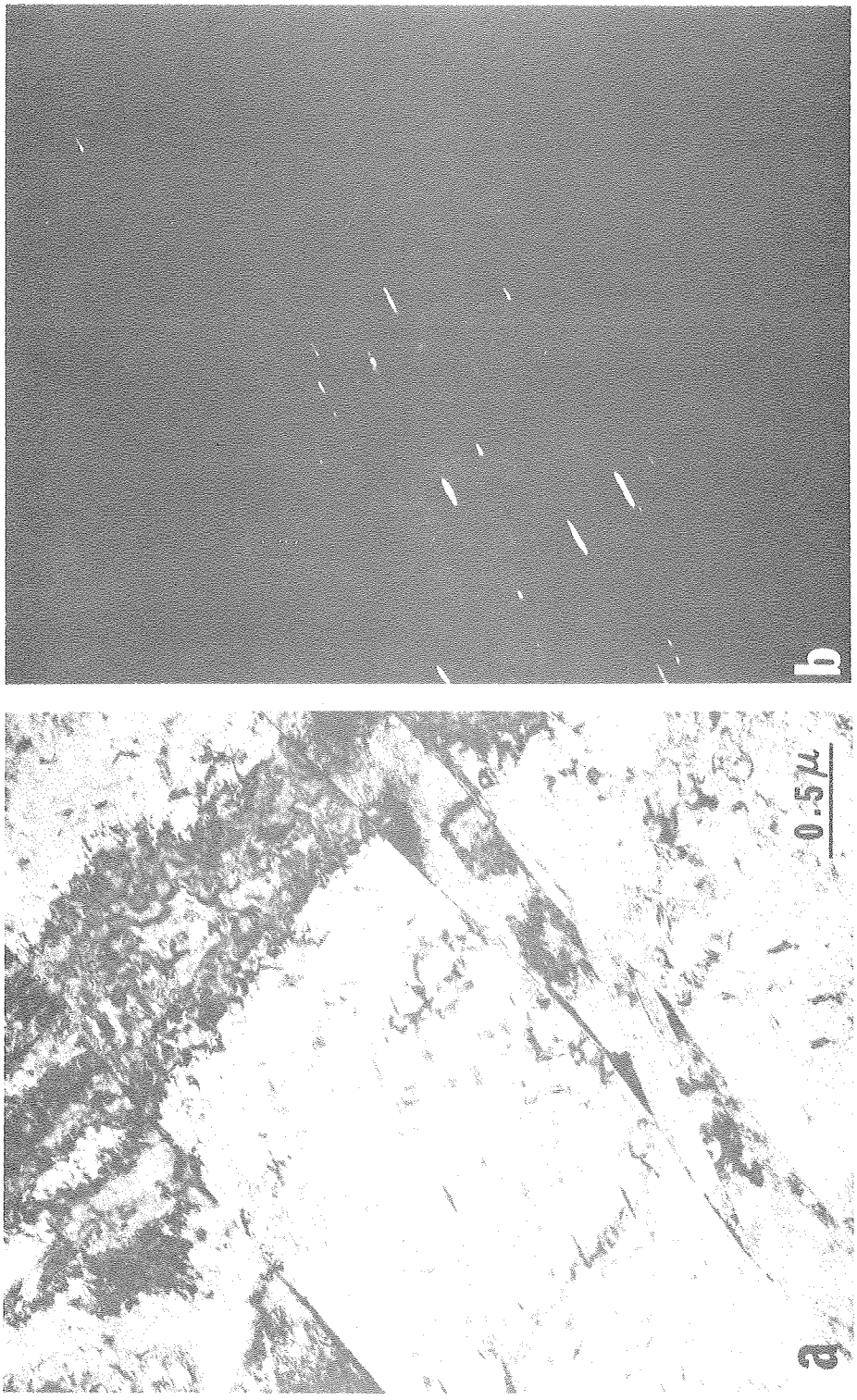

XBB 778-7528

Figure 13

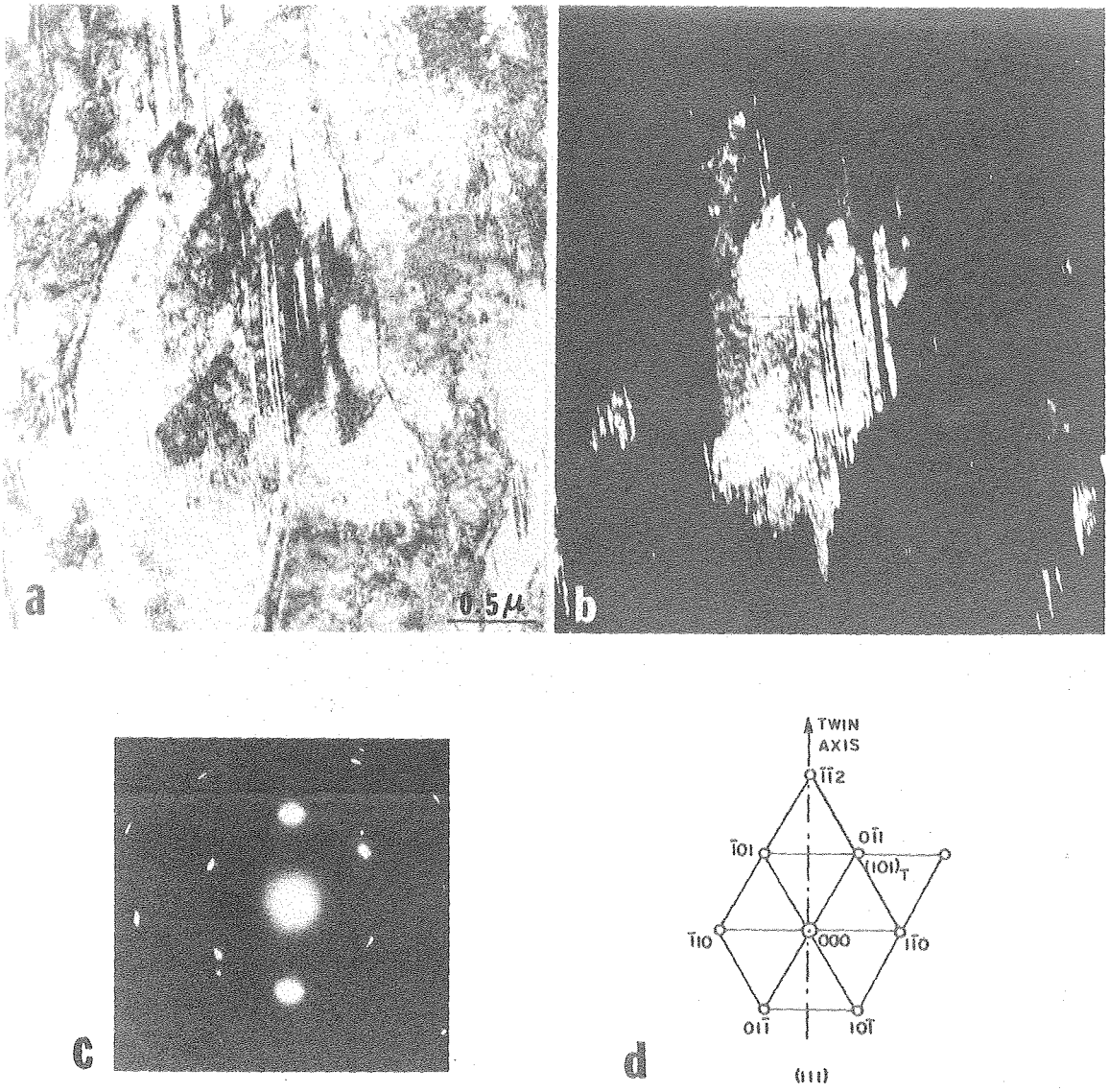

XBB 778-7541

Figure 14

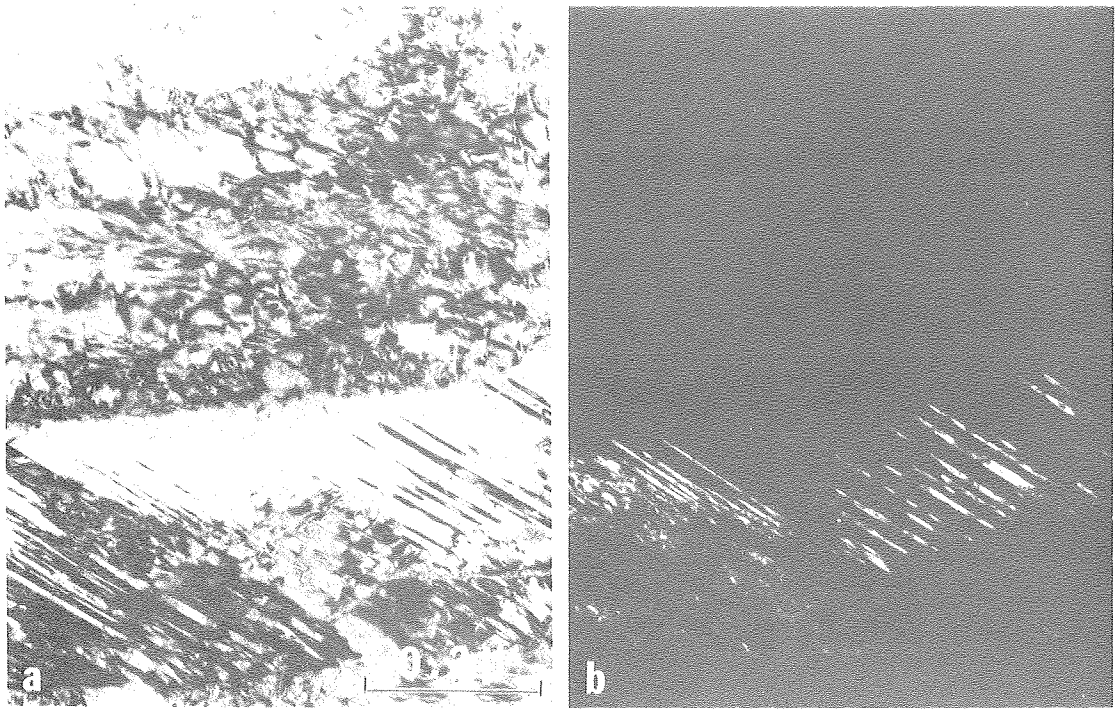

XBB 778-7558

Figure 15

XBB 788-7537

Figure 16

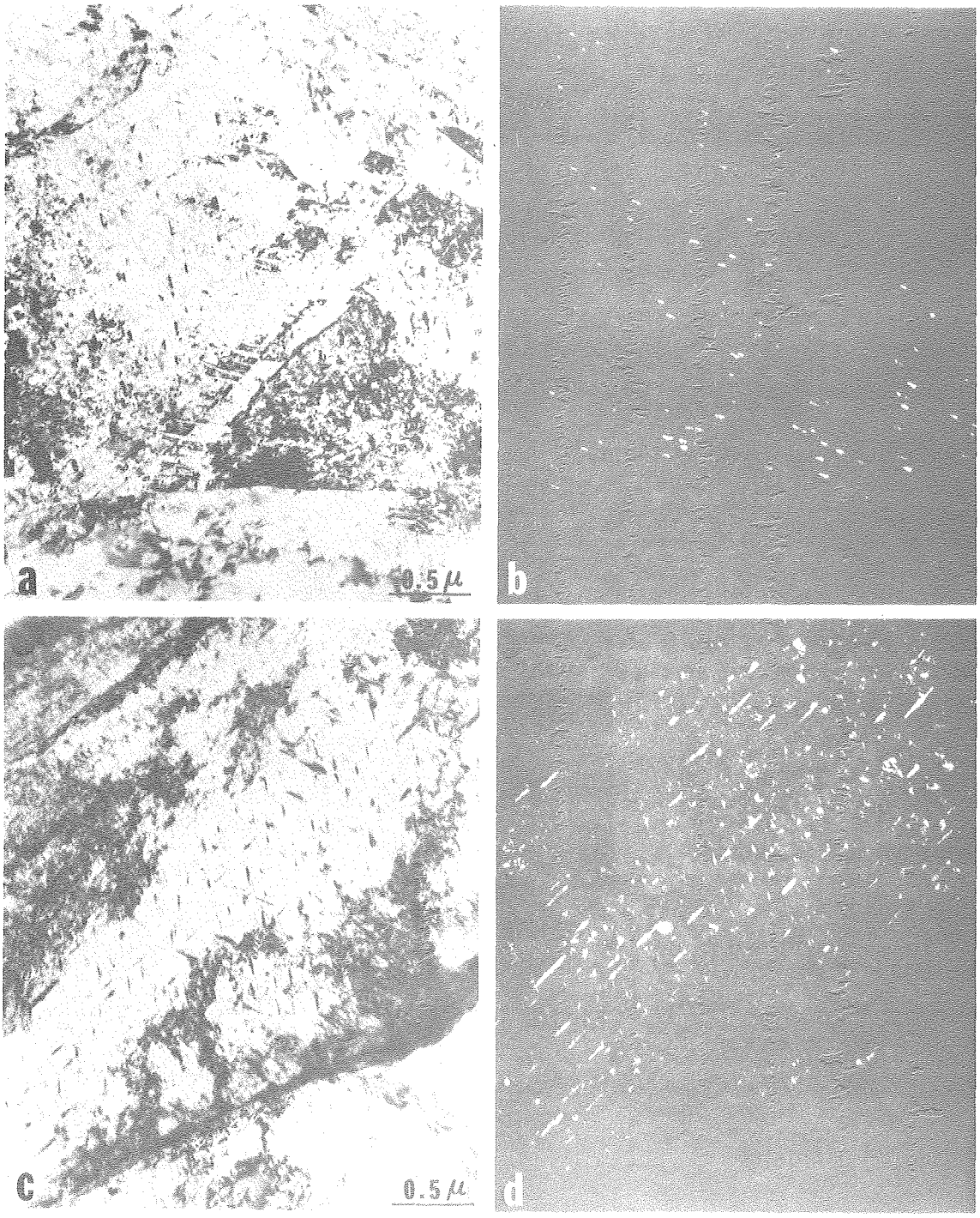

XBB 778-7557

Figure 17

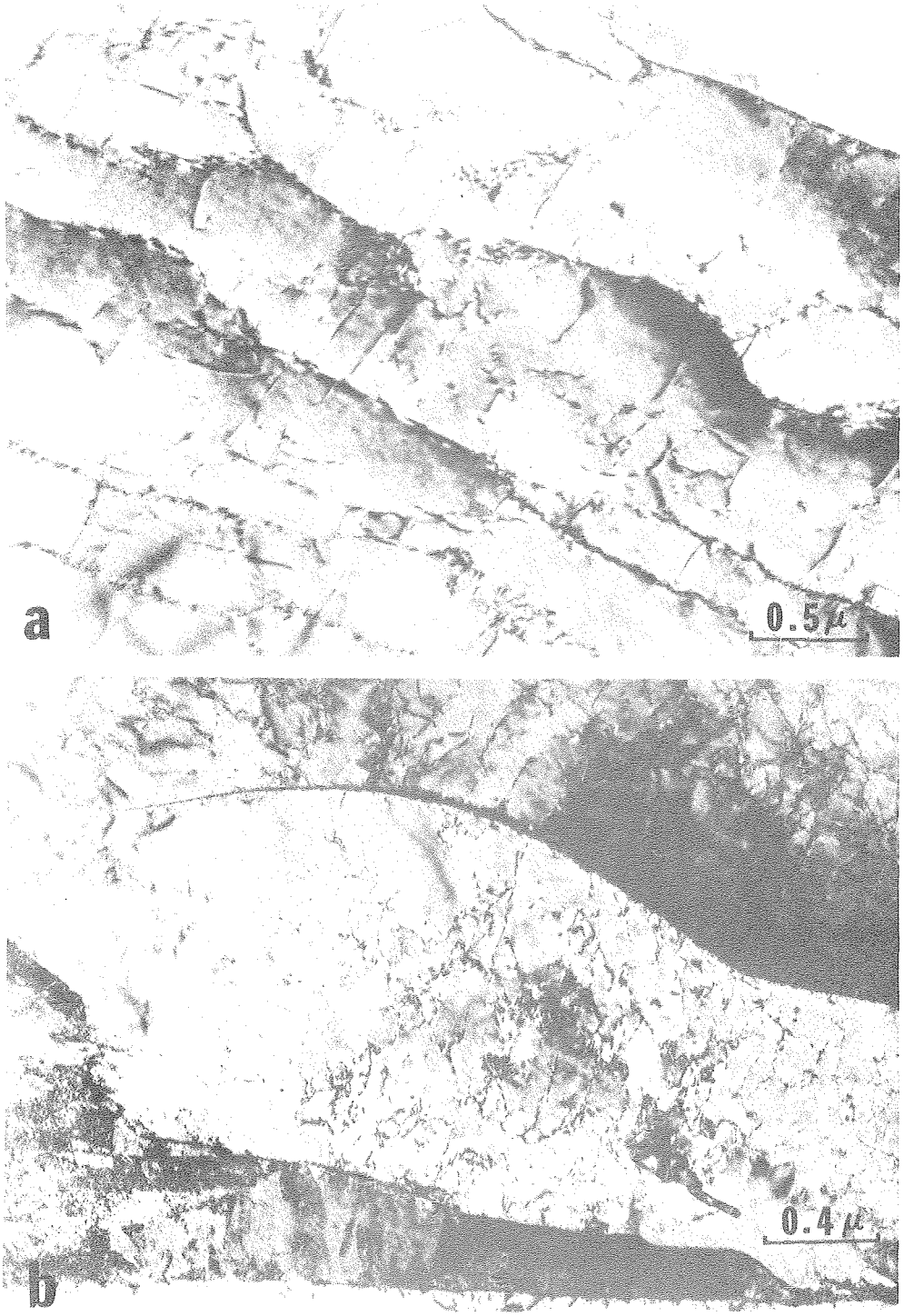

XBB 778-7549

Figure 18

XBB 761-356

Figure 19 (a)

XBB 778-7555

Figure 19 (b)

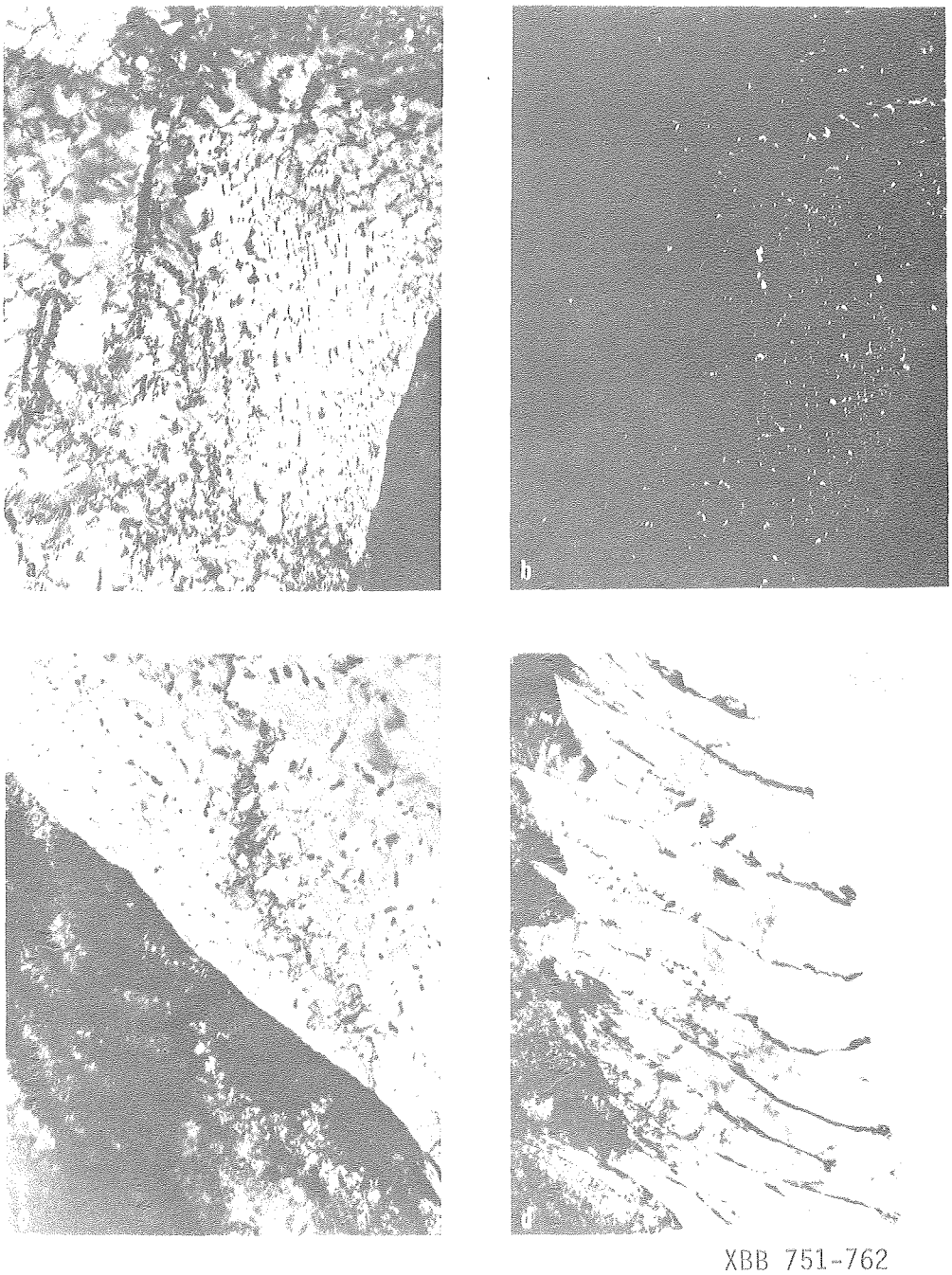

XBB 751-762

Figure 20

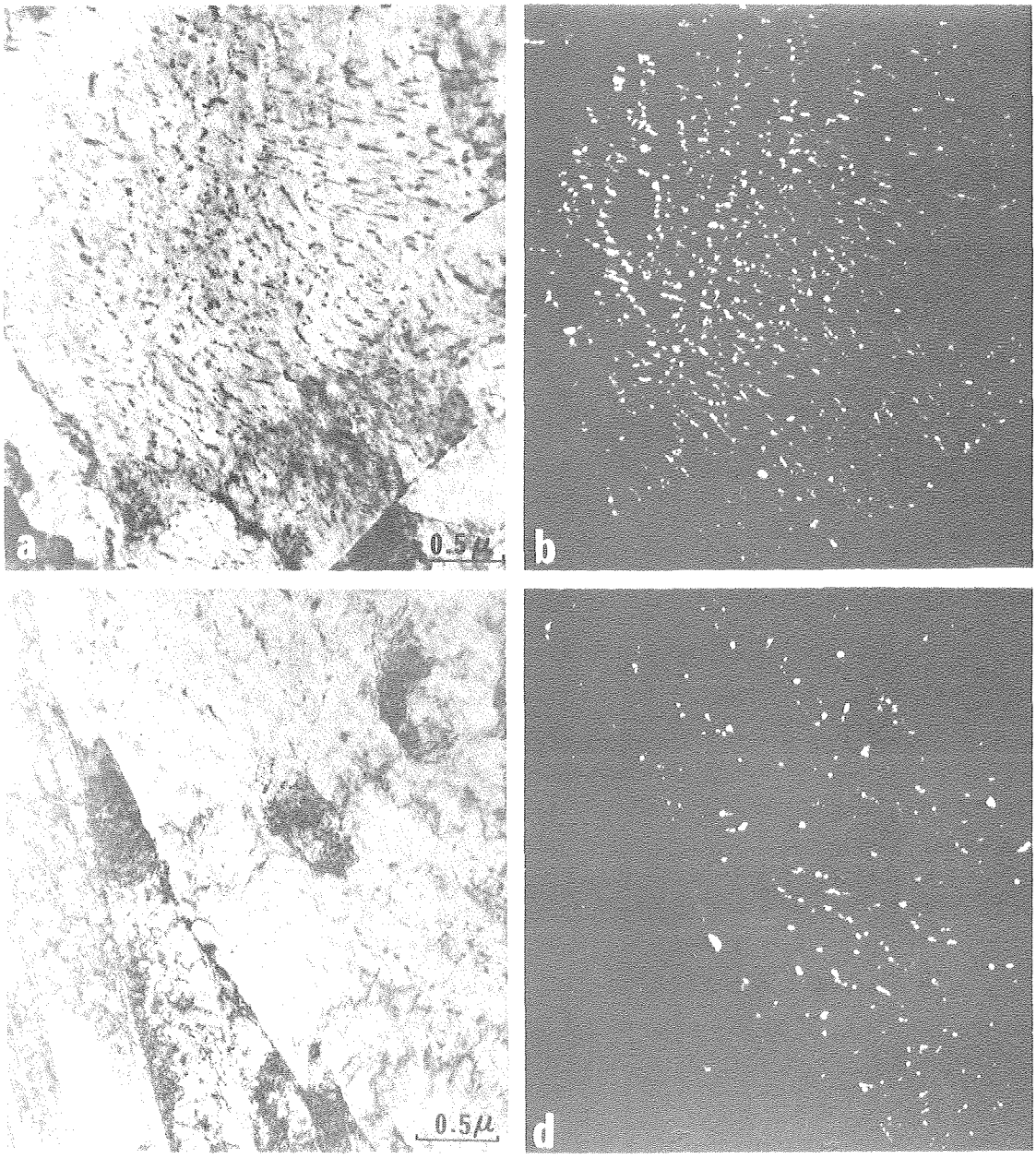

XBB 778-7556

Figure 21

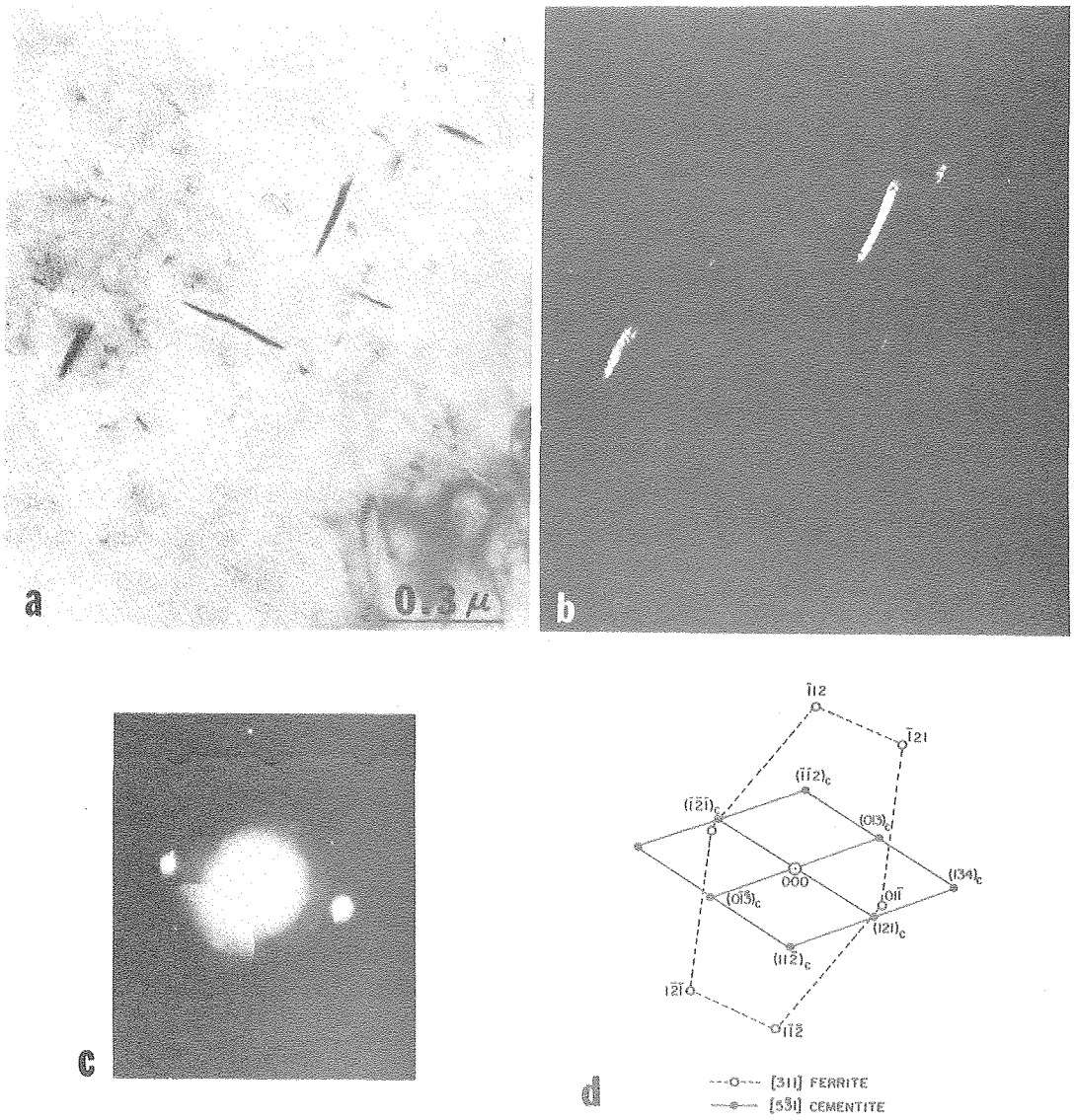

XBB 778-7540

Figure 22

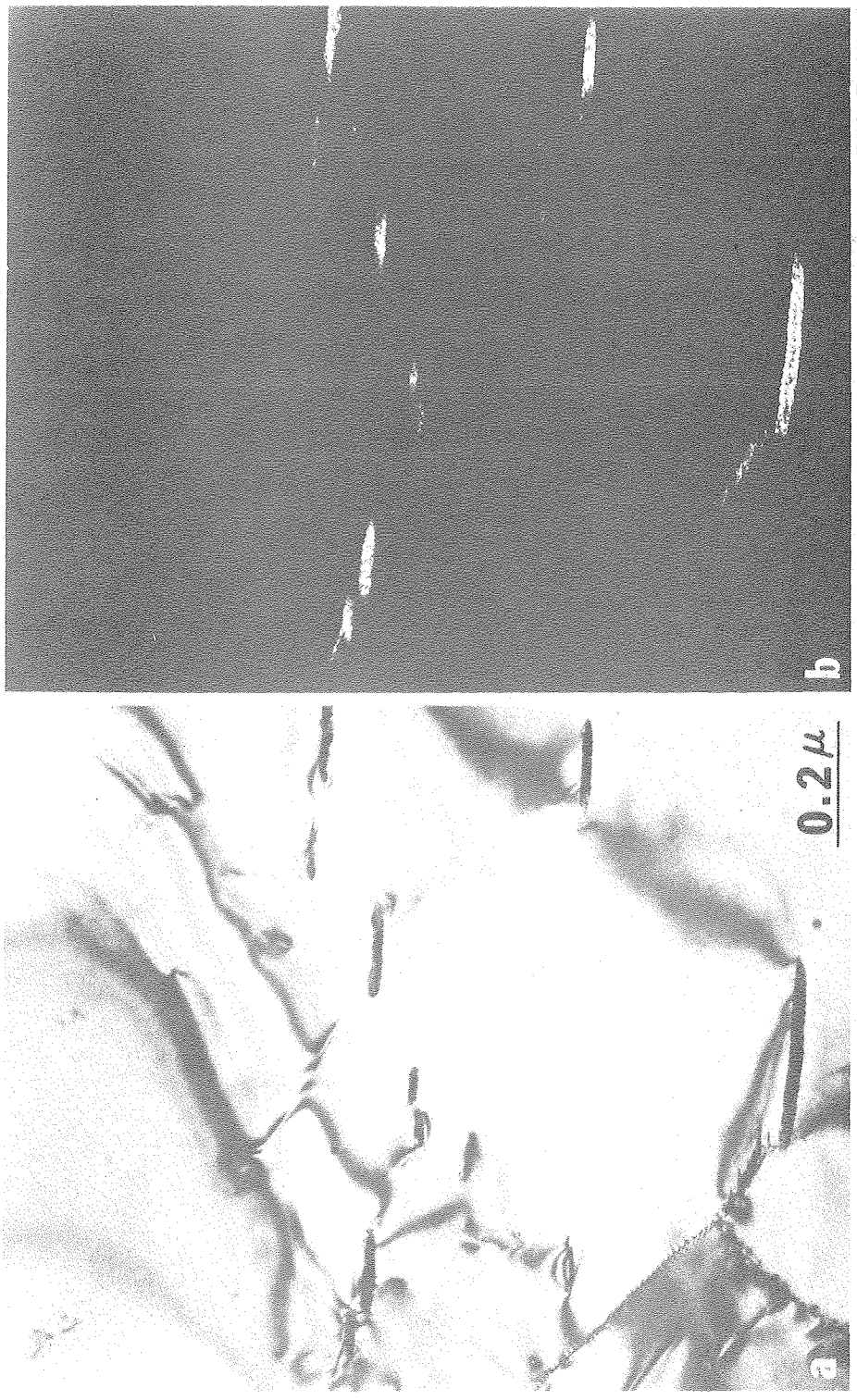

Figure 23

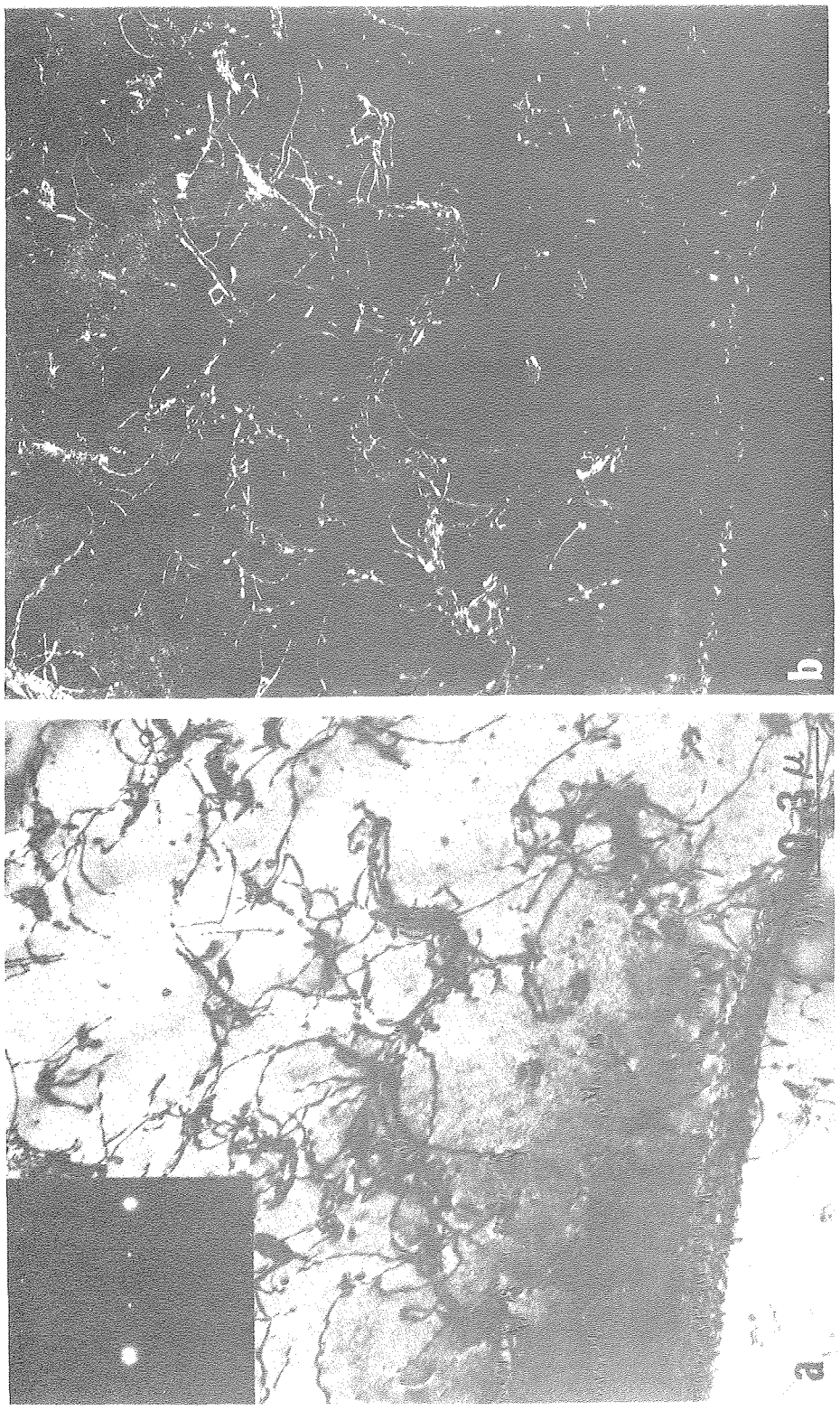

XBB 778-7536

Figure 24

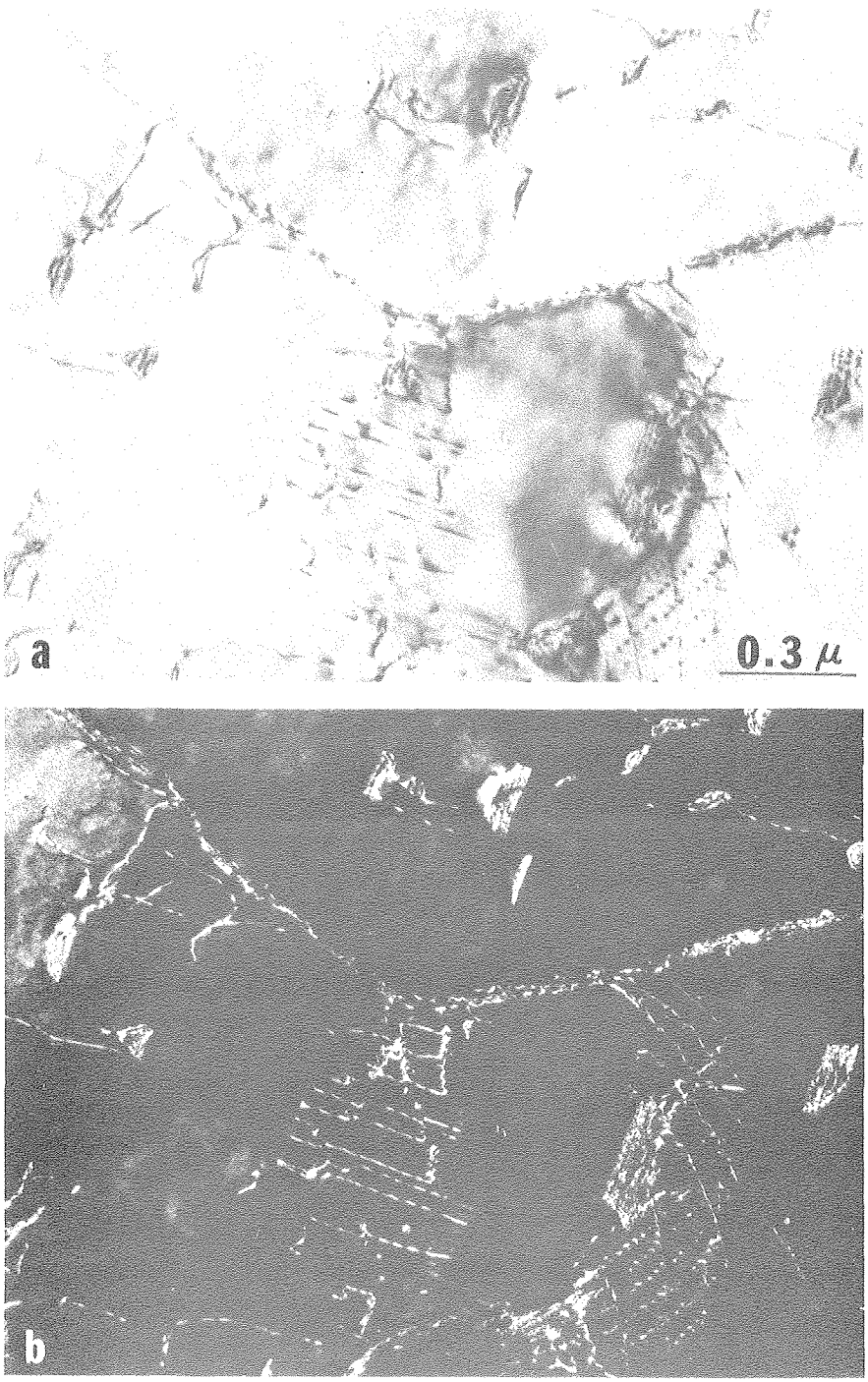

XBB 778-7543

Figure 25

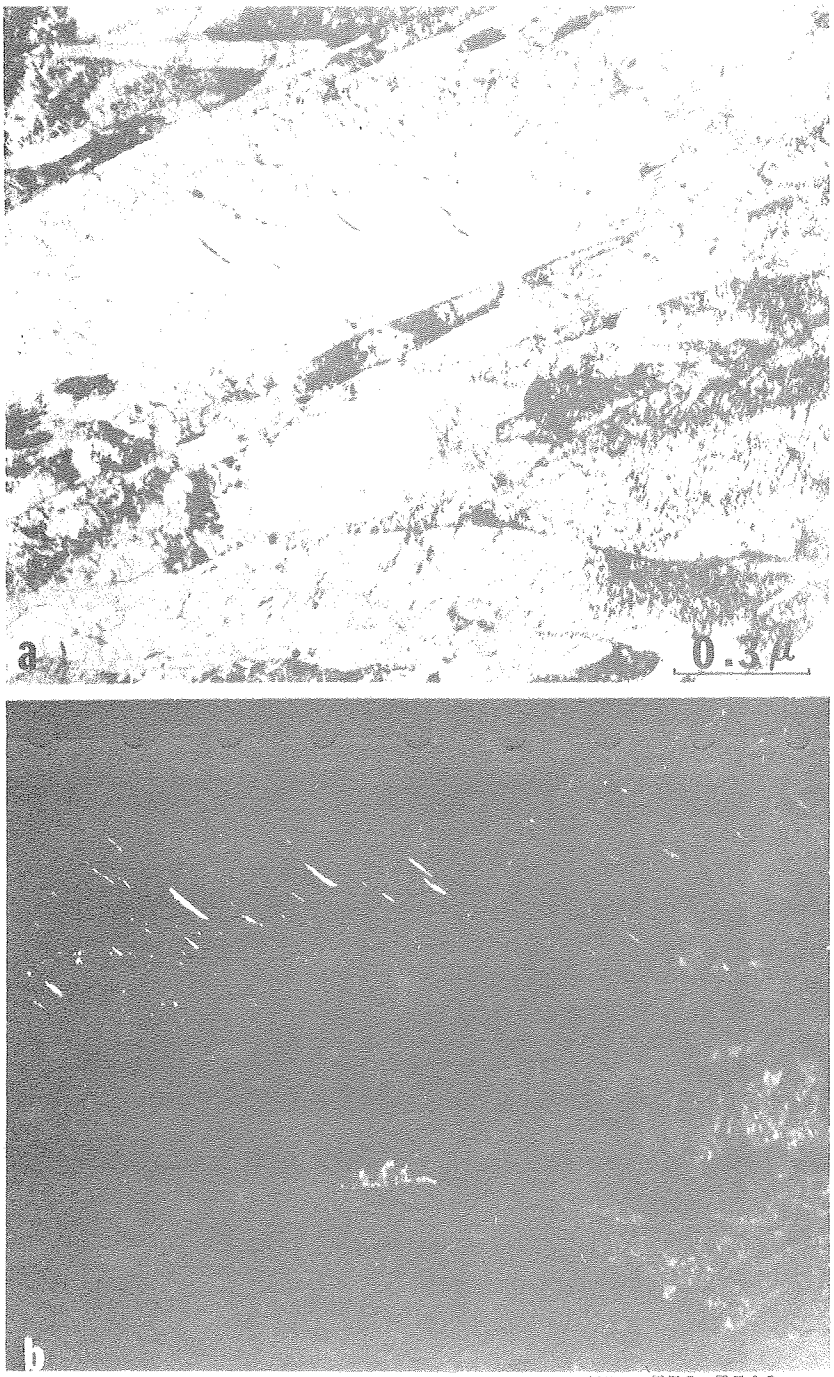

XBB 778-7546

Figure 26

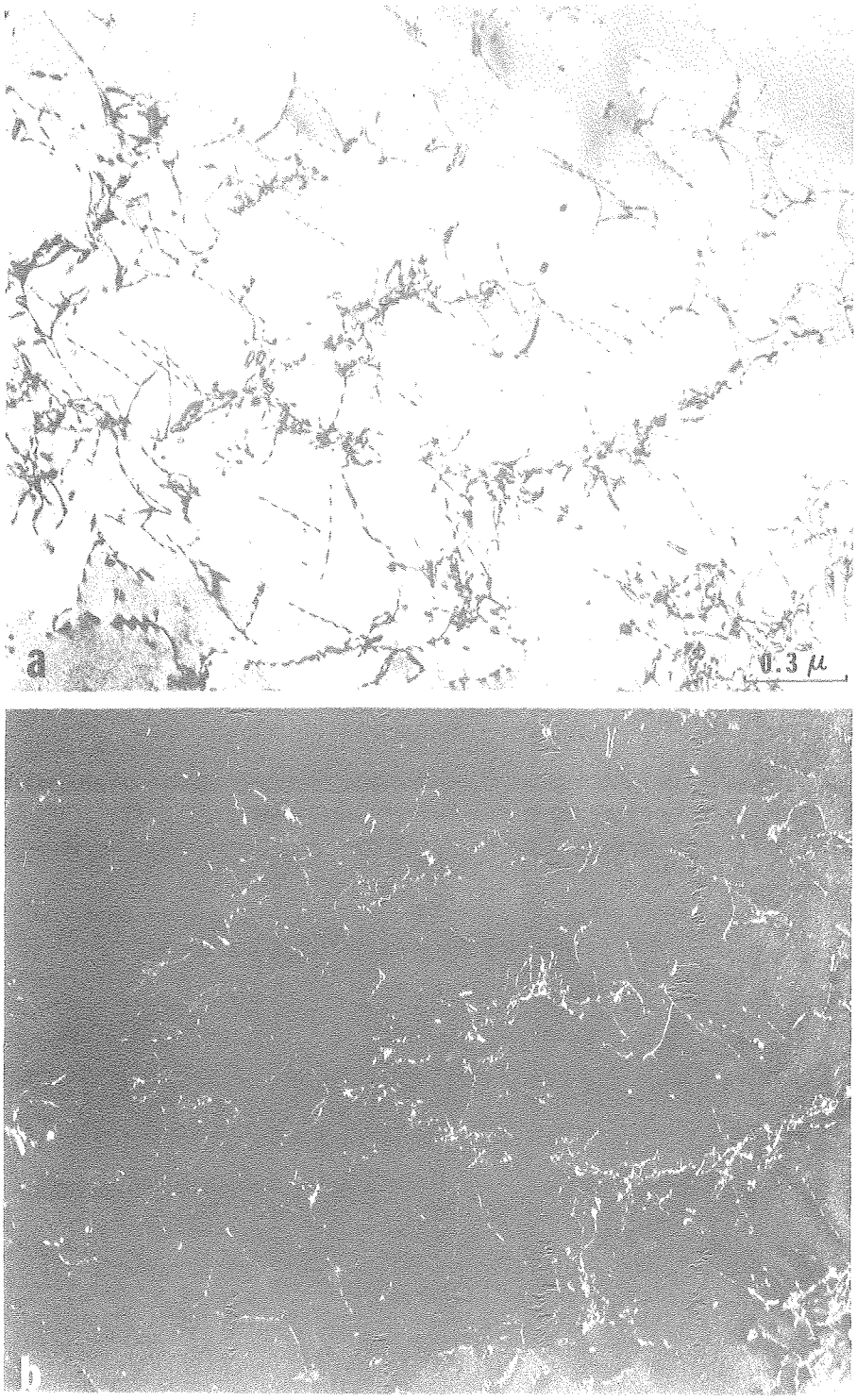

XBB 778-7545

Figure 27

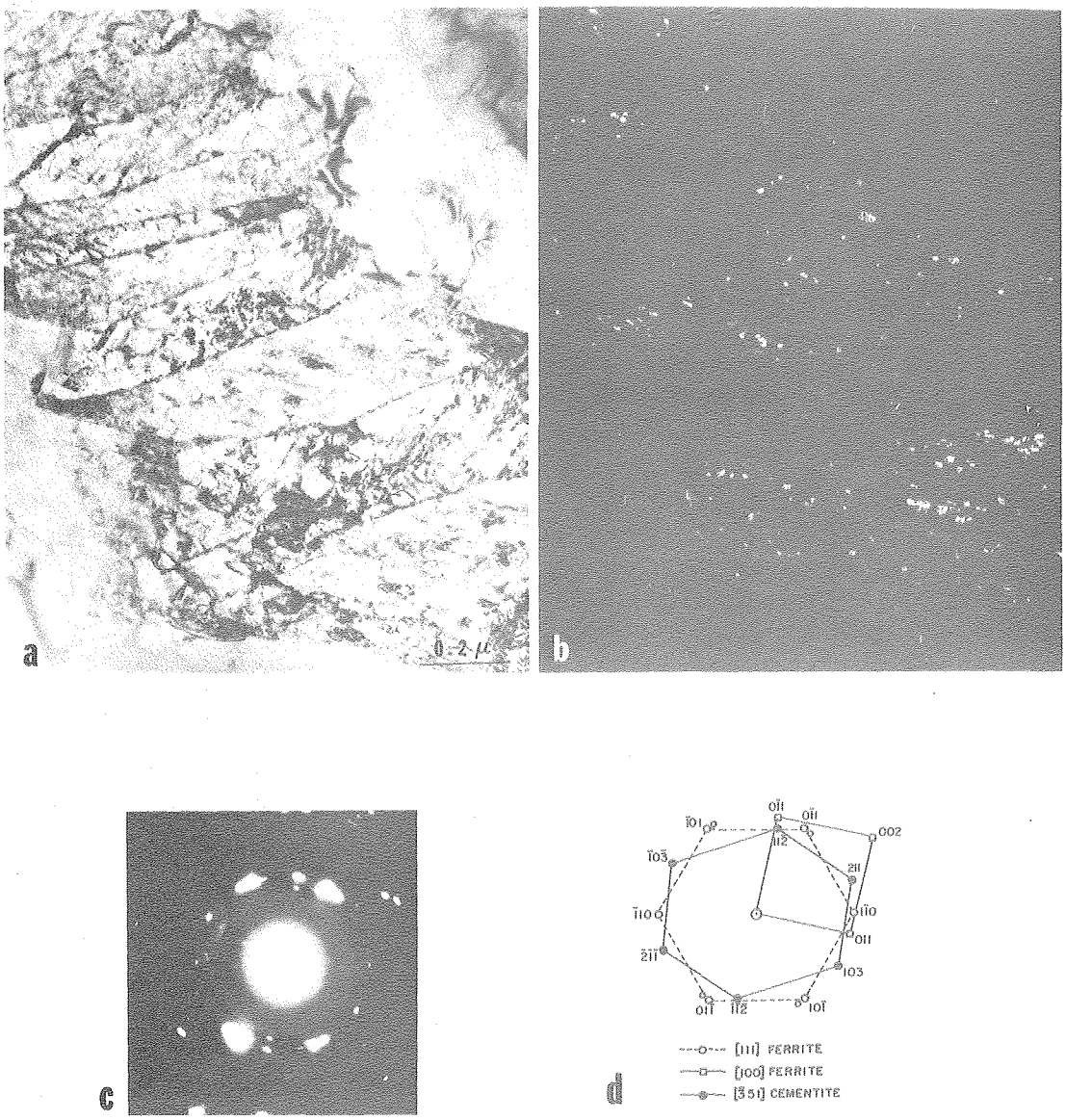

XBB 778-7559

Figure 28

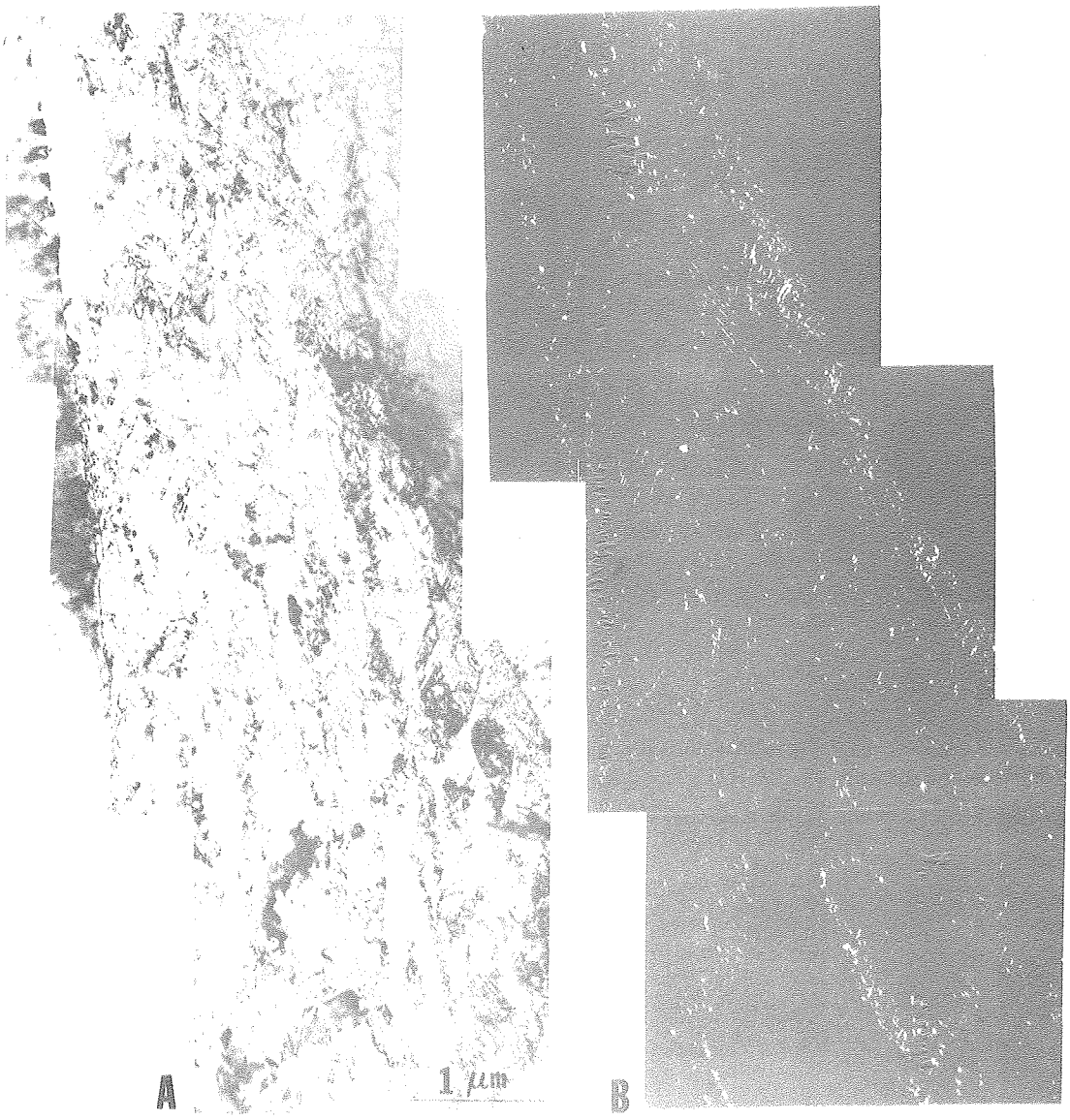

XBB 778-7542

Figure 29

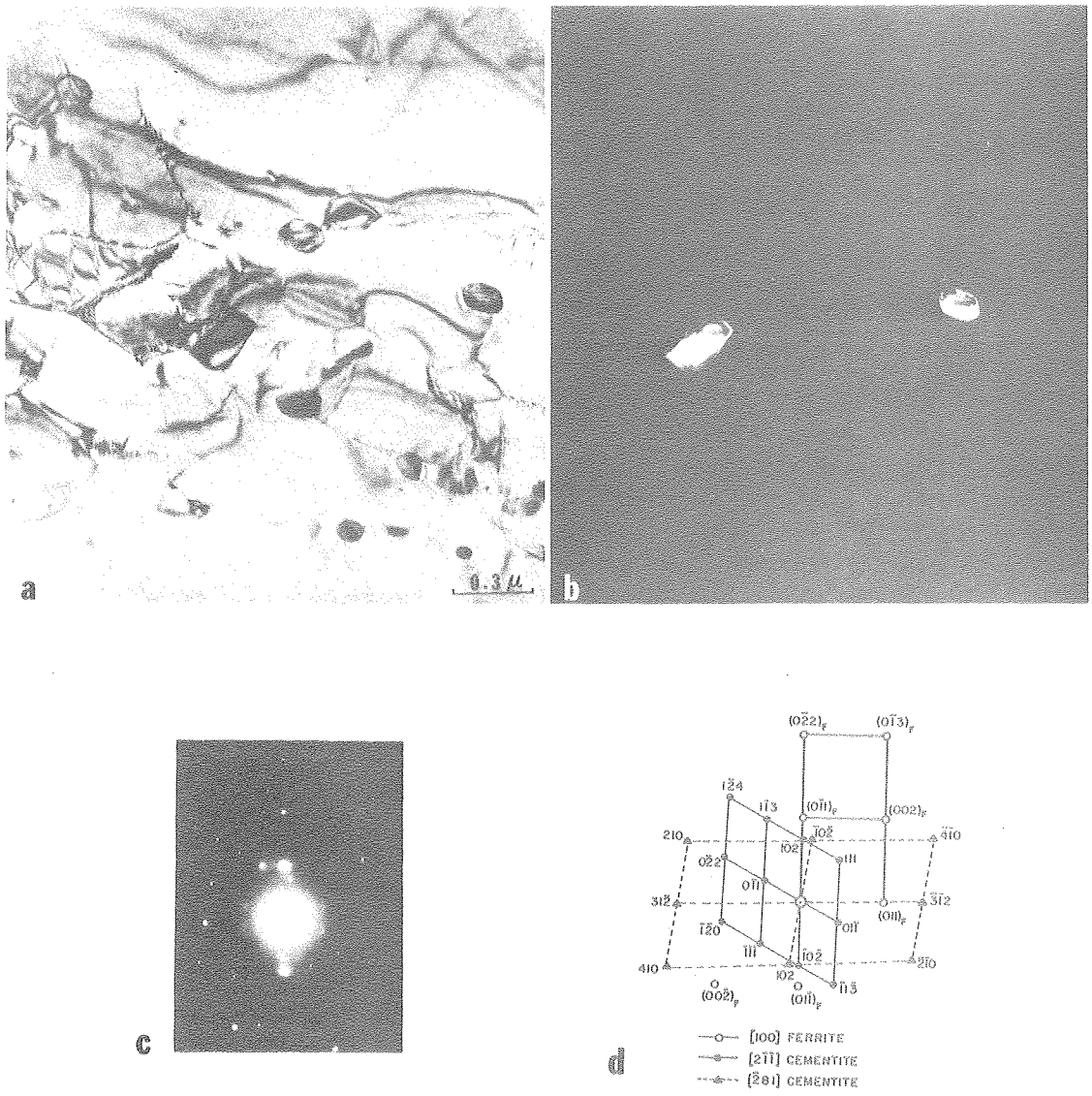

XBB 778-7560

Figure 30

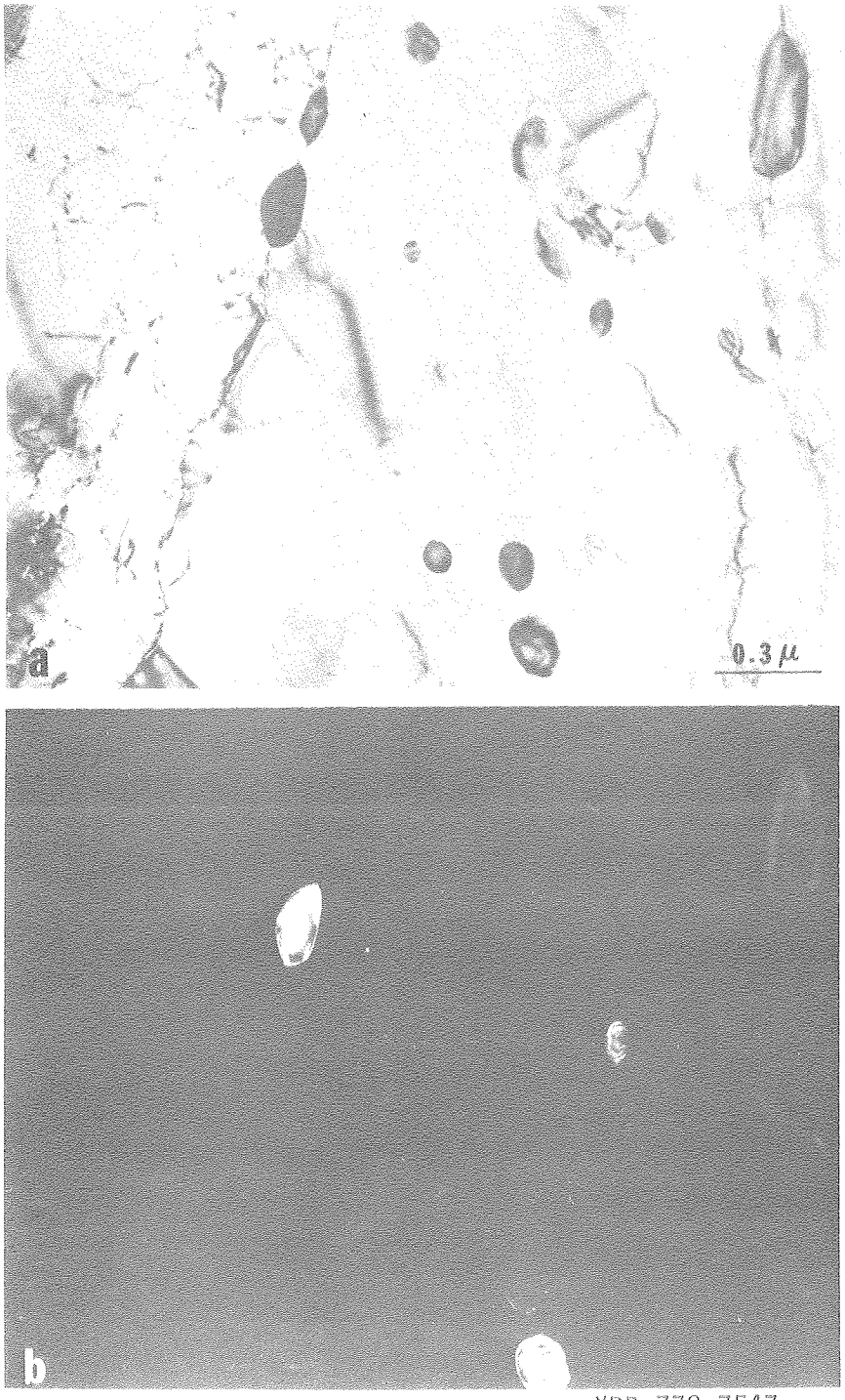

XBB 778-7547

Figure 31

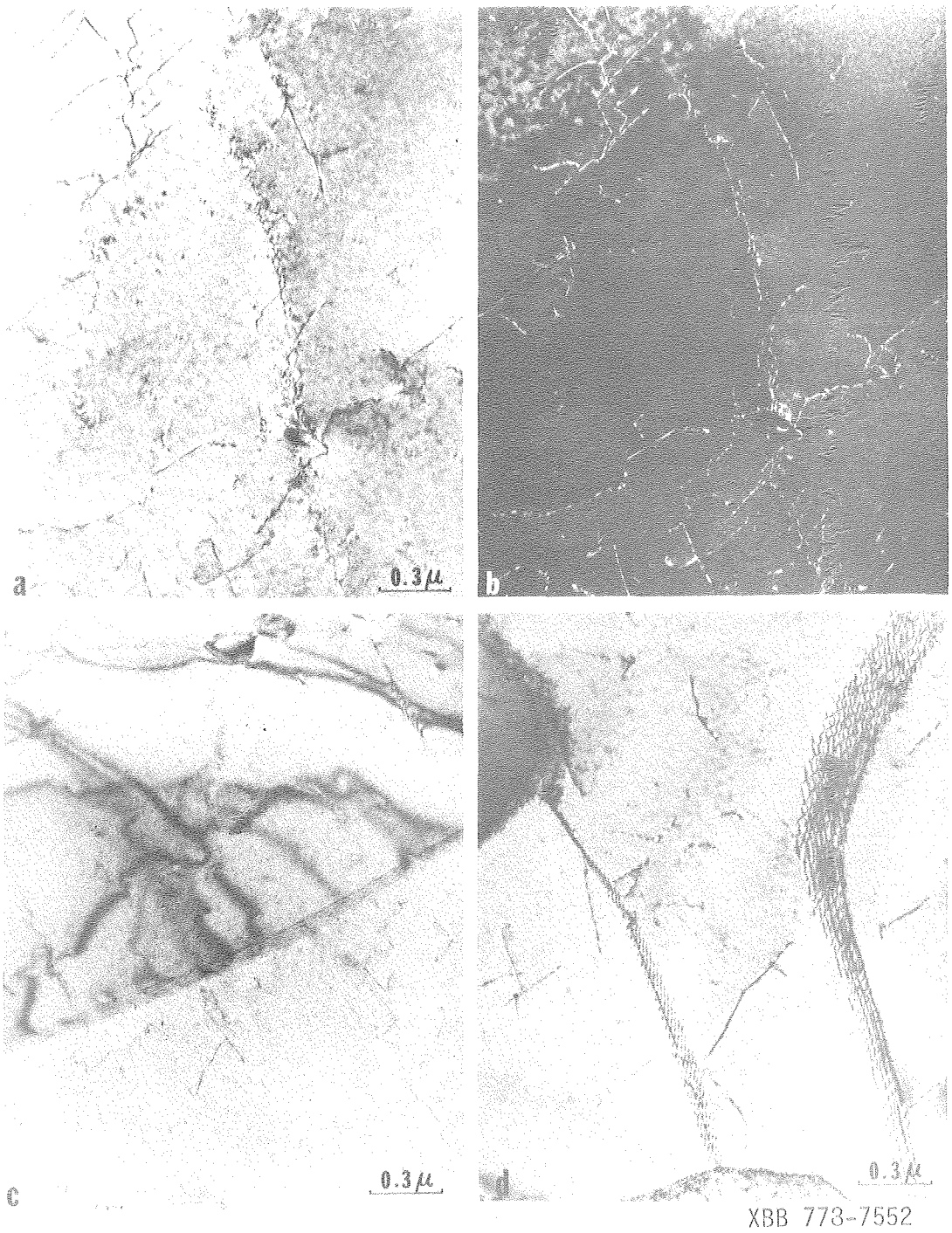

Figure 32

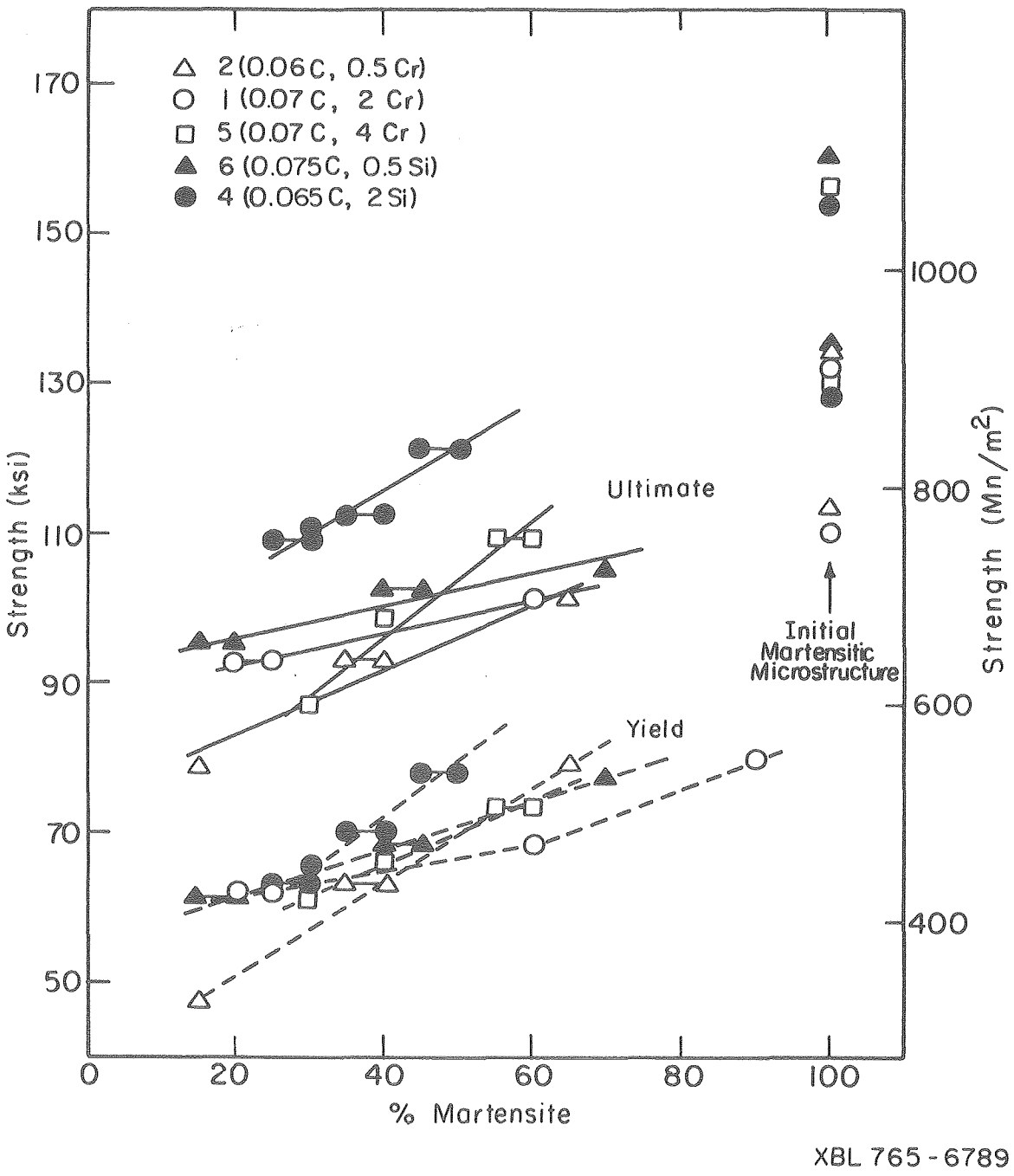

Figure 33

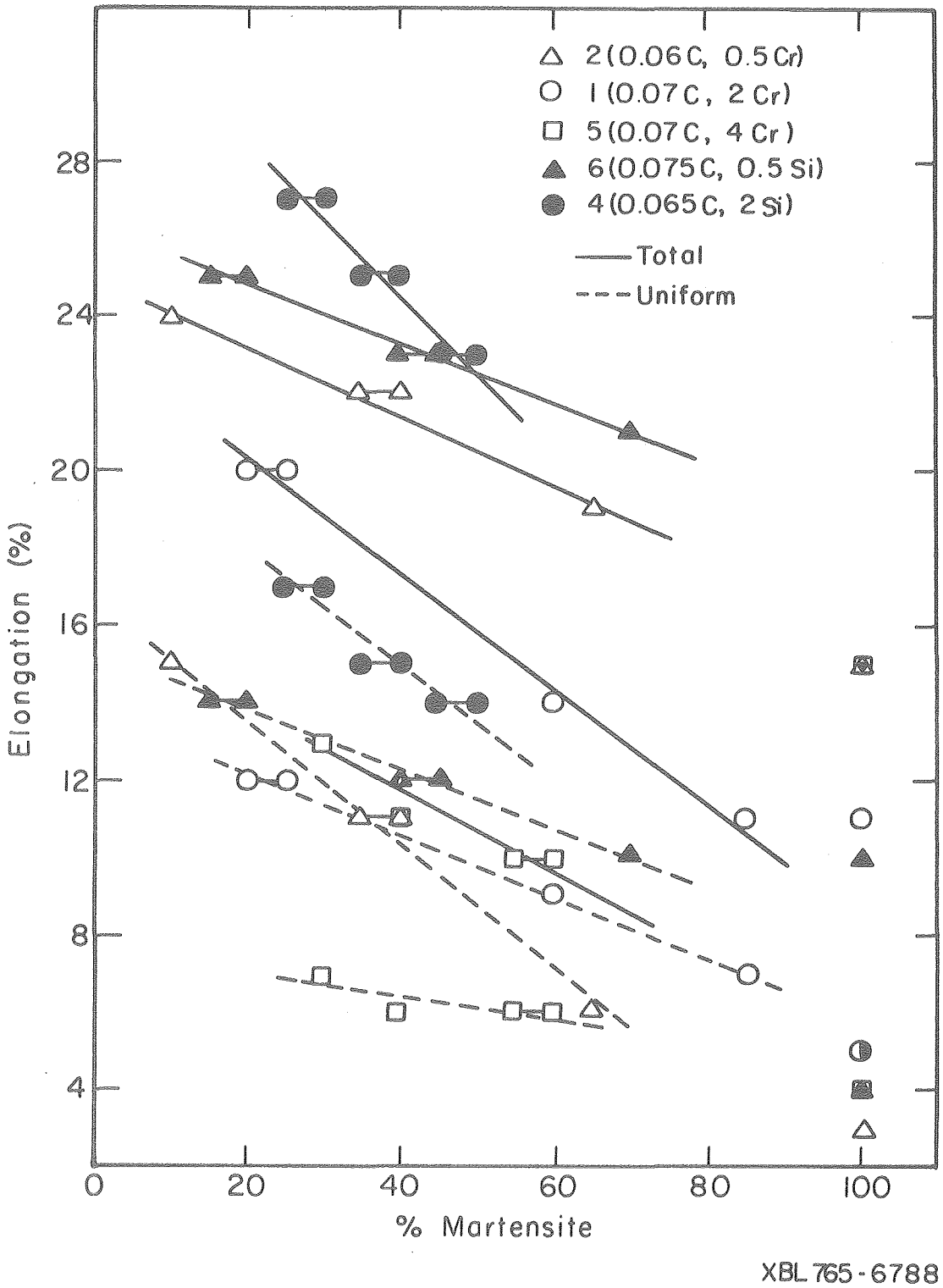
2(0.06C, 0.5Cr)
1(0.07C, 2Cr)
5(0.07C, 4Cr)
6(0.075C, 0.5Si)
4(0.065C, 2Si)
Total
Uniform
Elongation (%)
% Martensite
28
24
20
16
12
8
4
0
20
40
60
80
100
XBL 765-6788

Figure 34

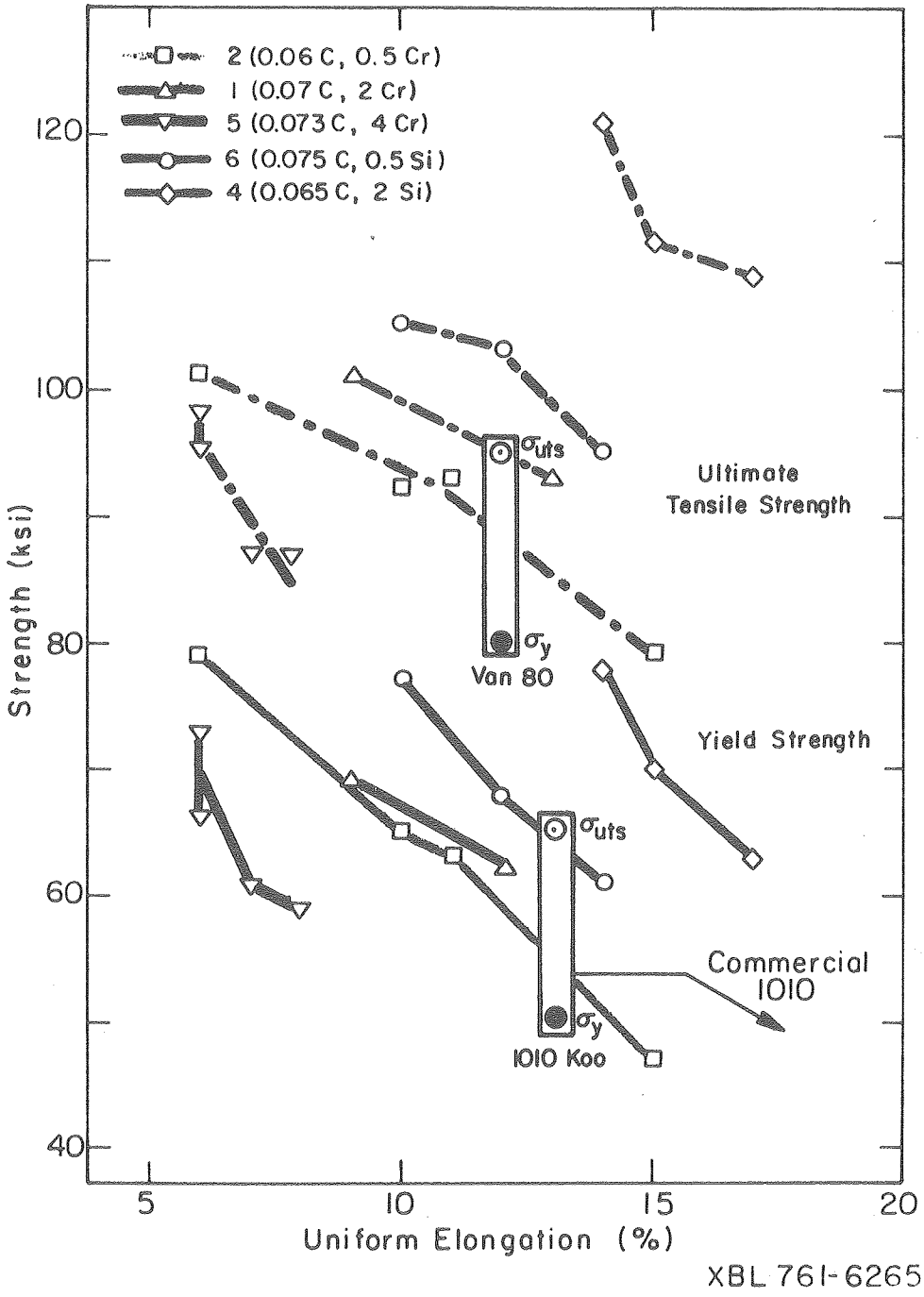

Figure 35

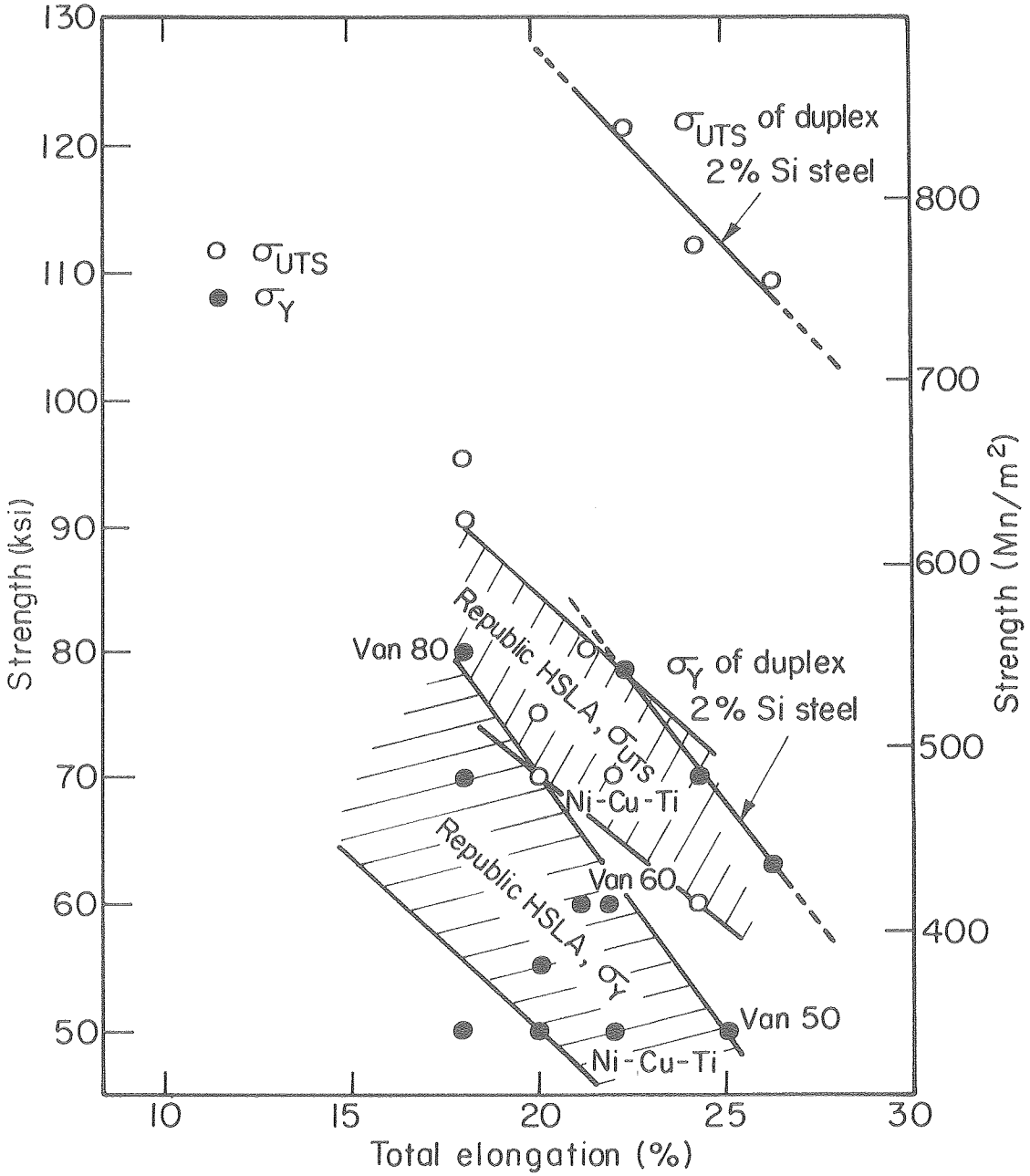

XBL766-9069A

Figure 36

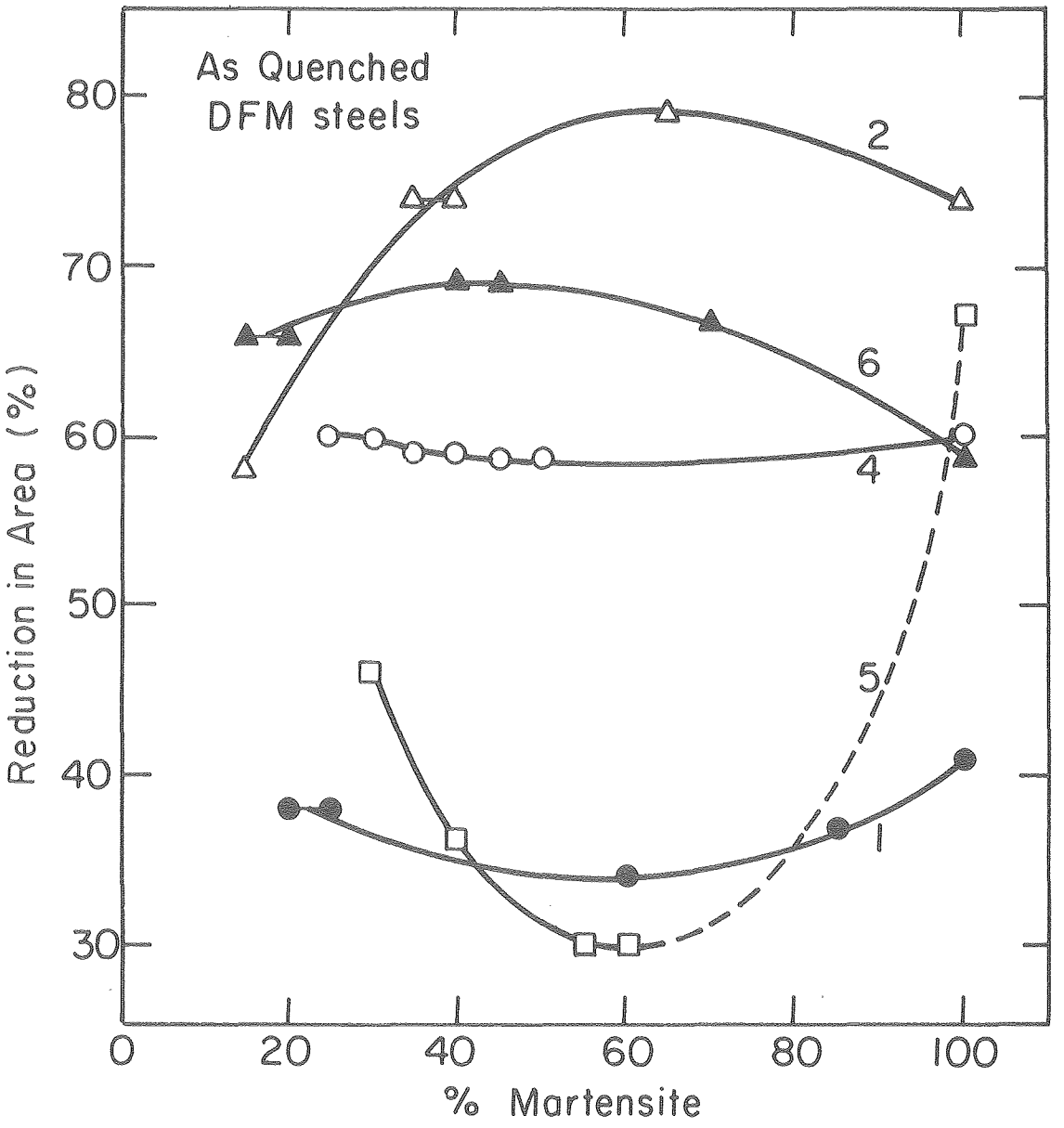

XBL 776-5565

Figure 37

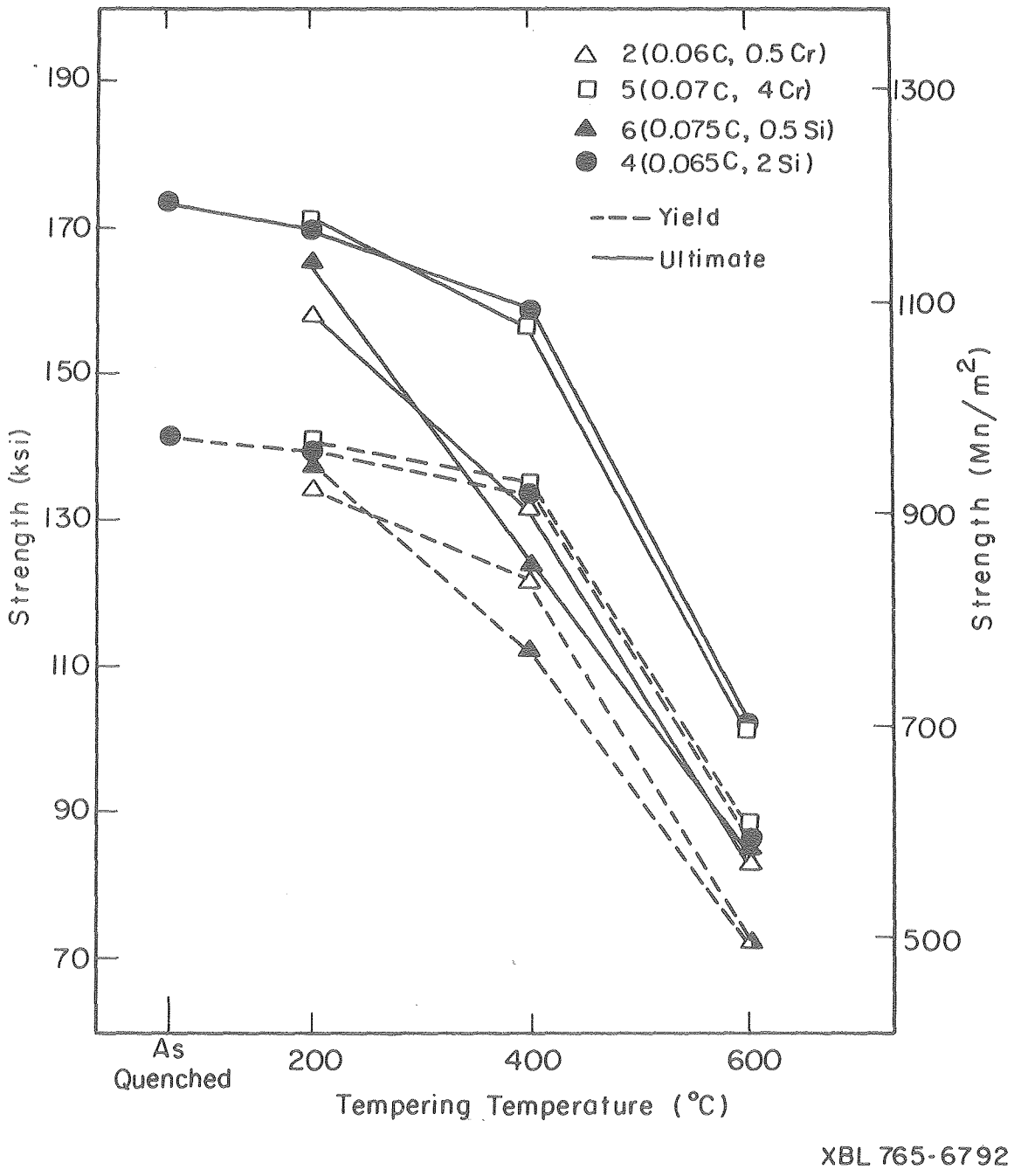
△ 2(0.06C, 0.5 Cr)
□ 5(0.07C, 4 Cr)
▲ 6(0.075C, 0.5 Si)
● 4(0.065C, 2 Si)
Yield
Ultimate
190
170
150
130
110
90
70
1300
1100
900
700
500
Strength (ksi)
Strength (Mn/m²)
As Quenched
200
400
600
Tempering Temperature (°C)
XBL 765-6792

Figure 38

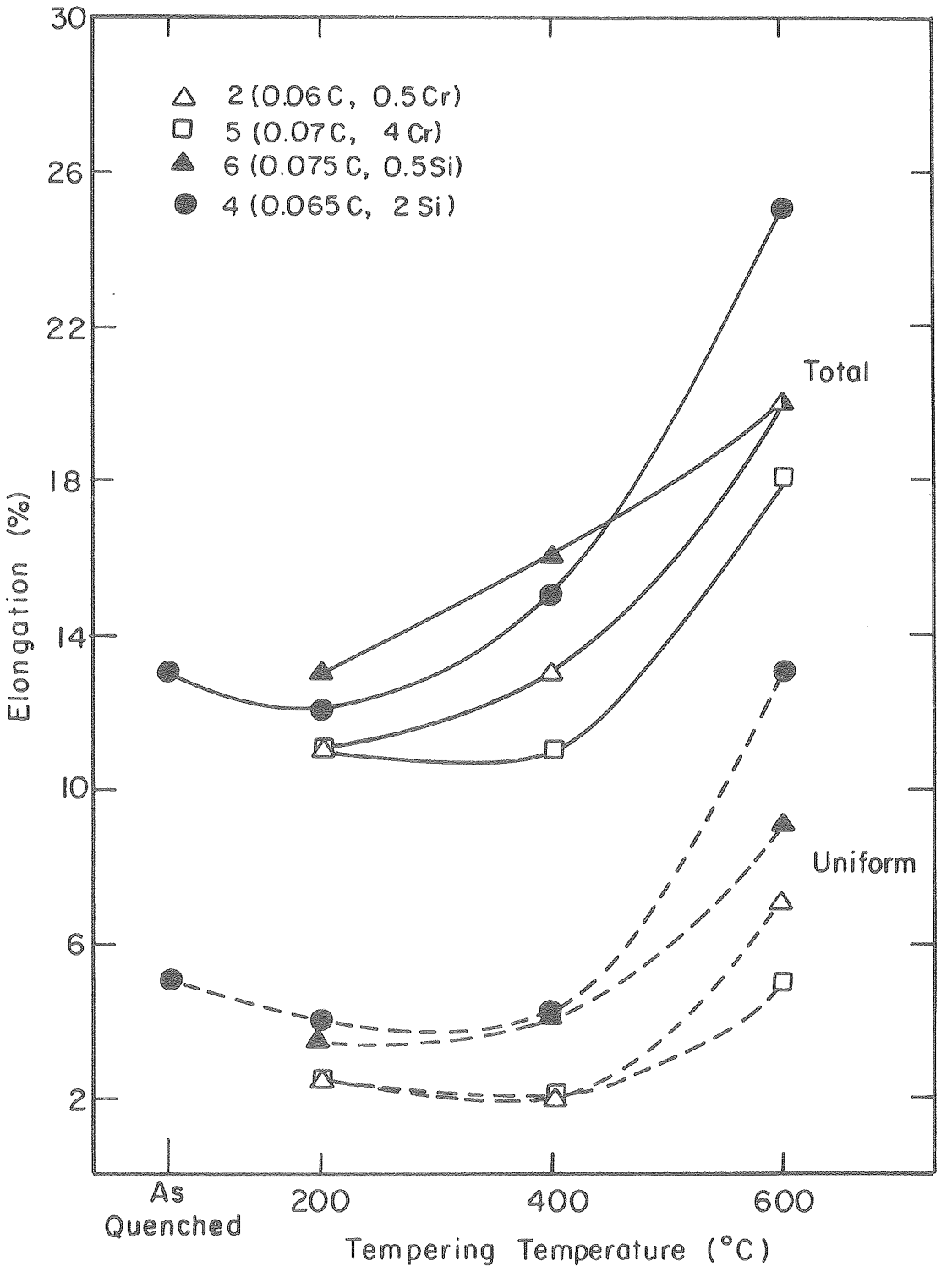

XBL 765-6793

Figure 39

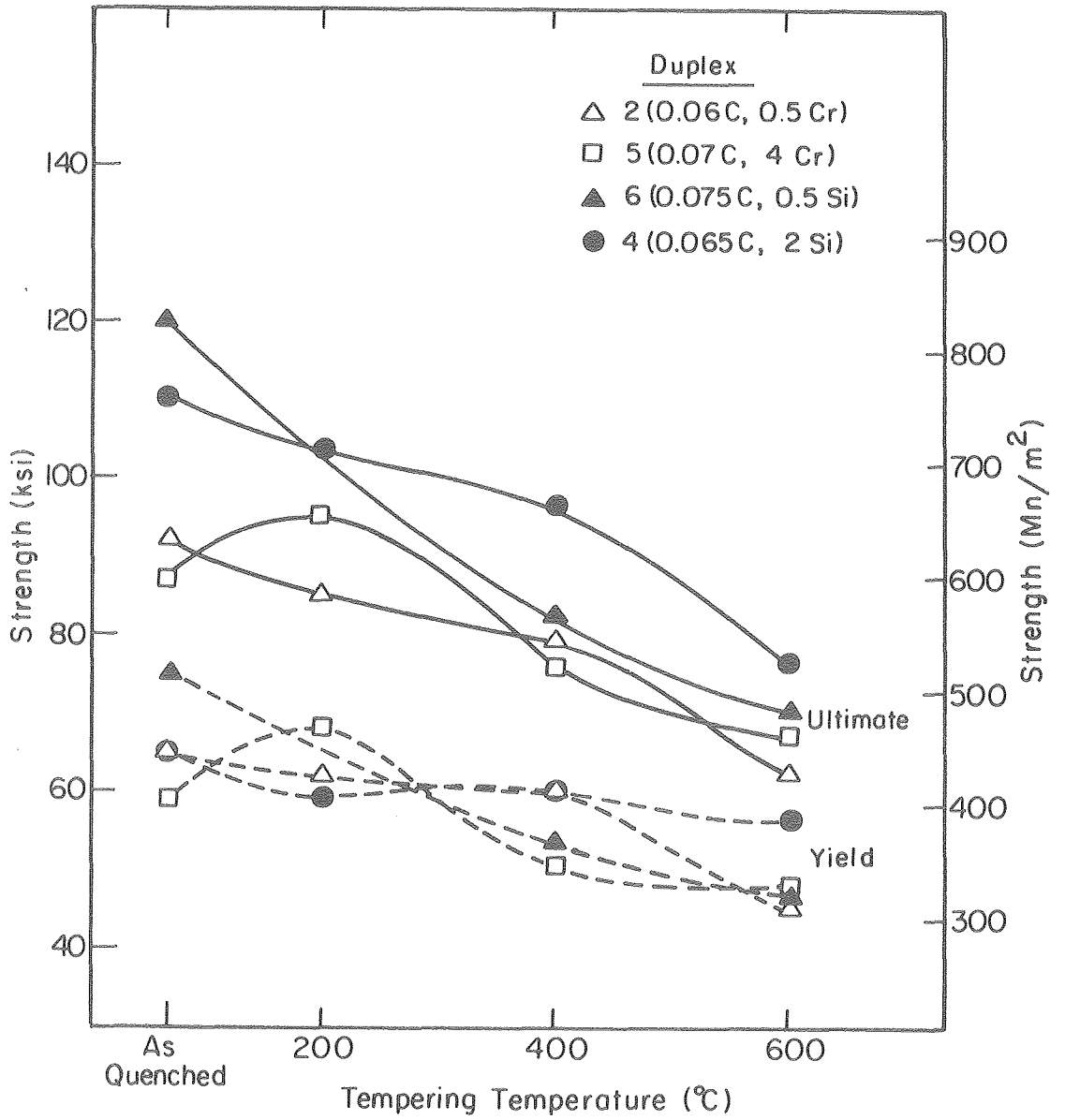

XBL765-6790

Figure 40

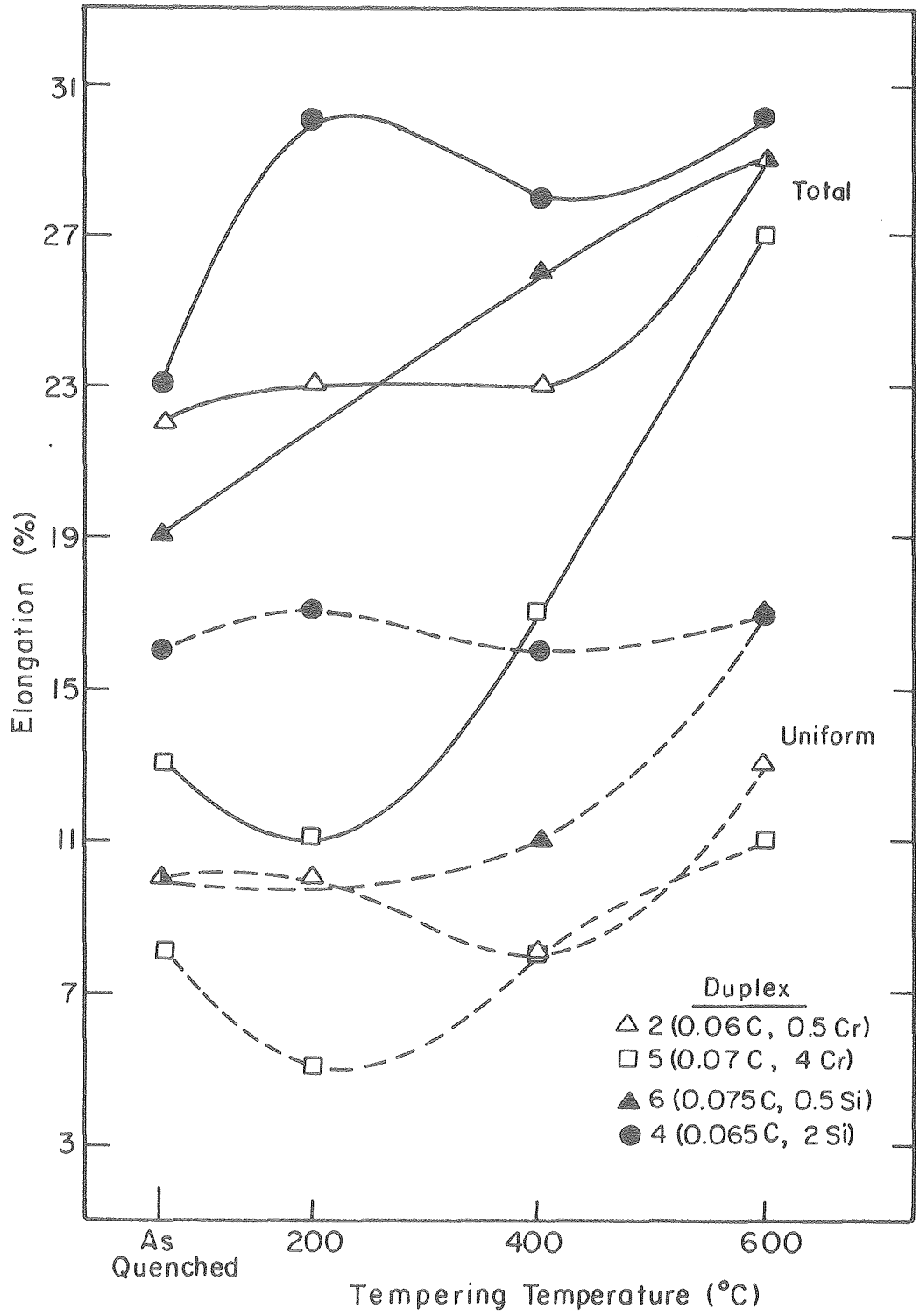

Figure 41

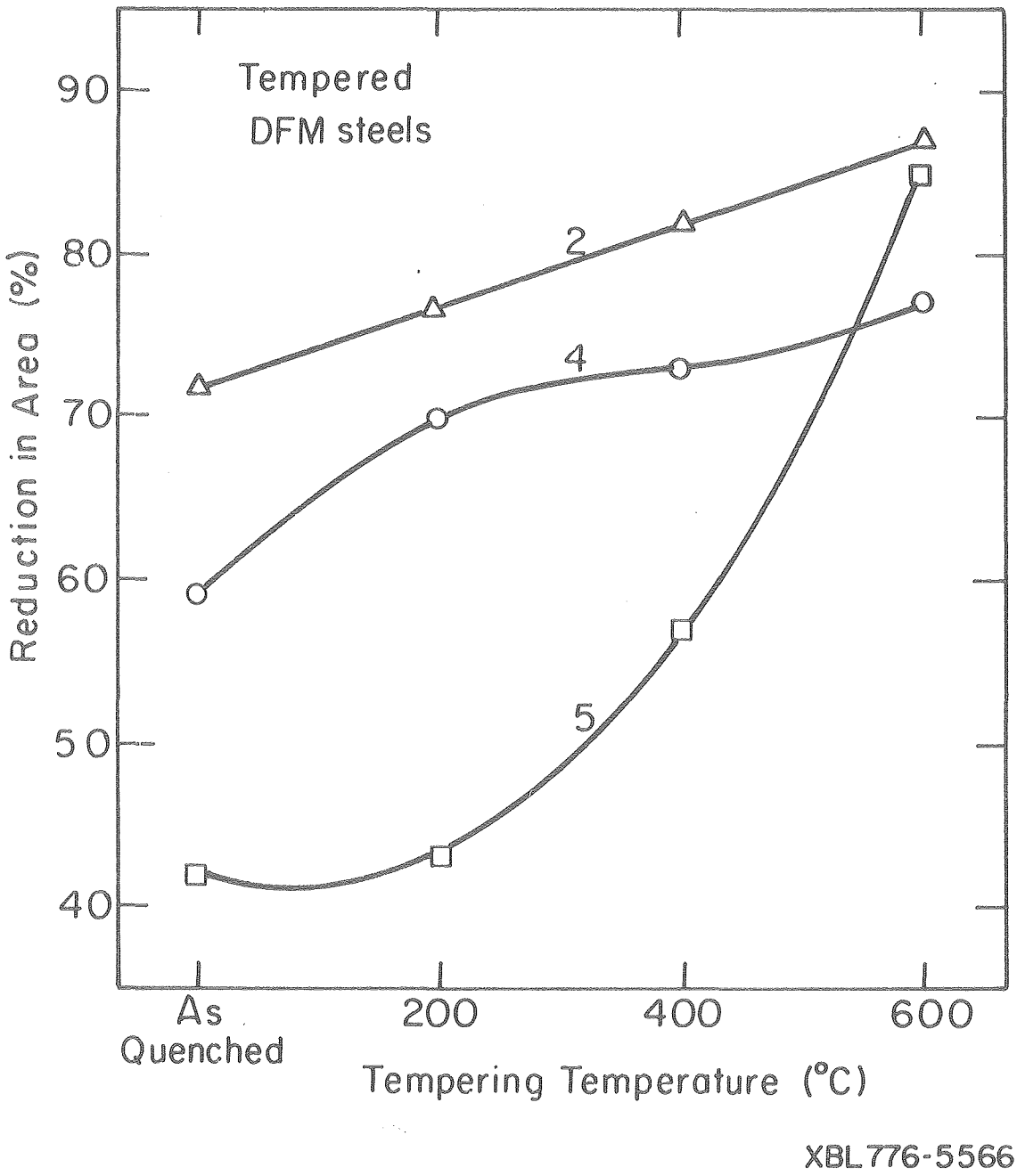

XBL776-5566

Figure 42

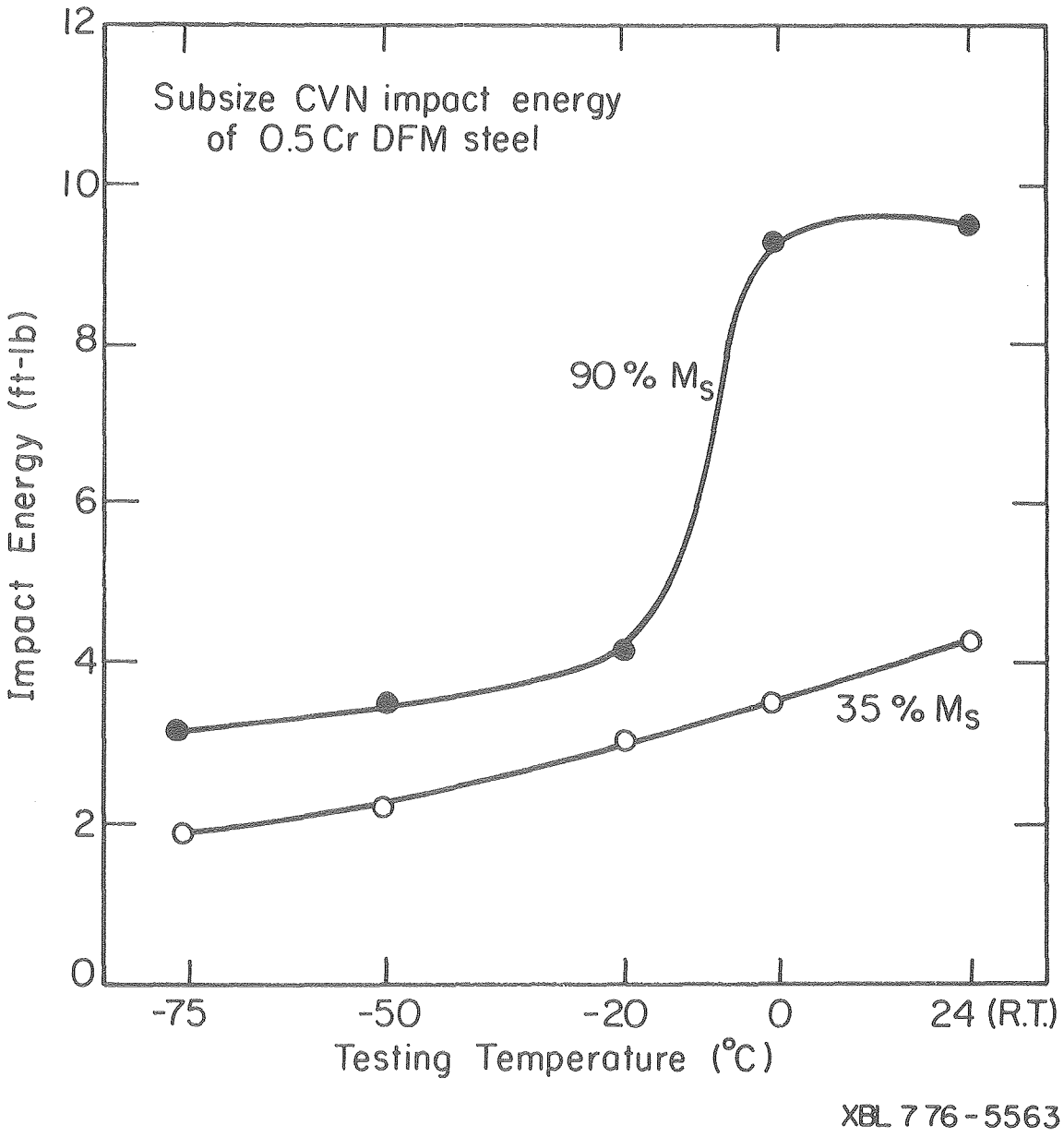

Figure 43

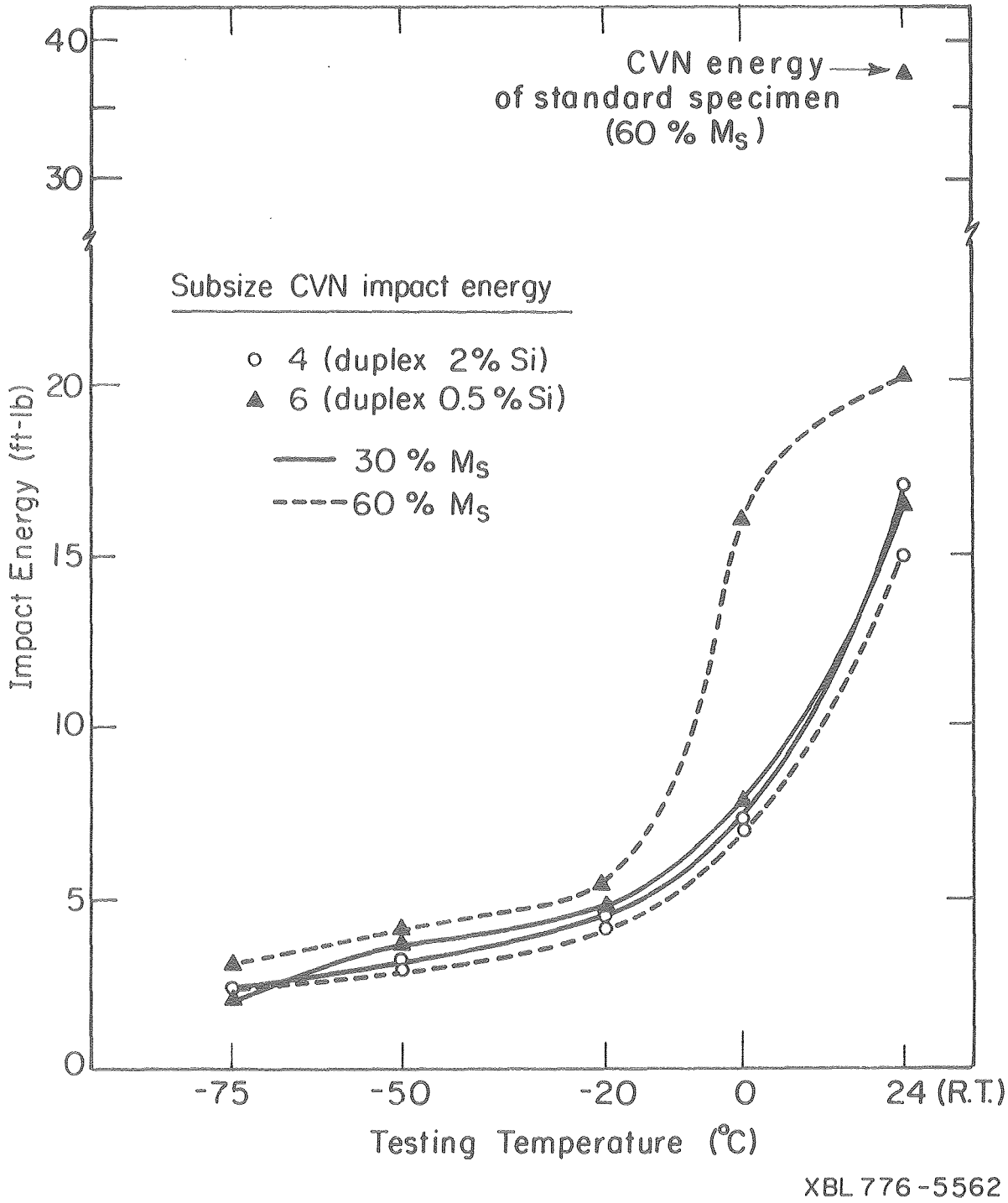
CVN energy
of standard specimen
(60 % Ms)
Subsize CVN impact energy
4 (duplex 2% Si)
6 (duplex 0.5 % Si)
30 % Ms
60 % Ms
Impact Energy (ft-lb)
40
30
20
15
10
5
0
-75
-50
-20
0
24 (R.T.)
Testing Temperature (°C)
XBL 776-5562

Figure 44

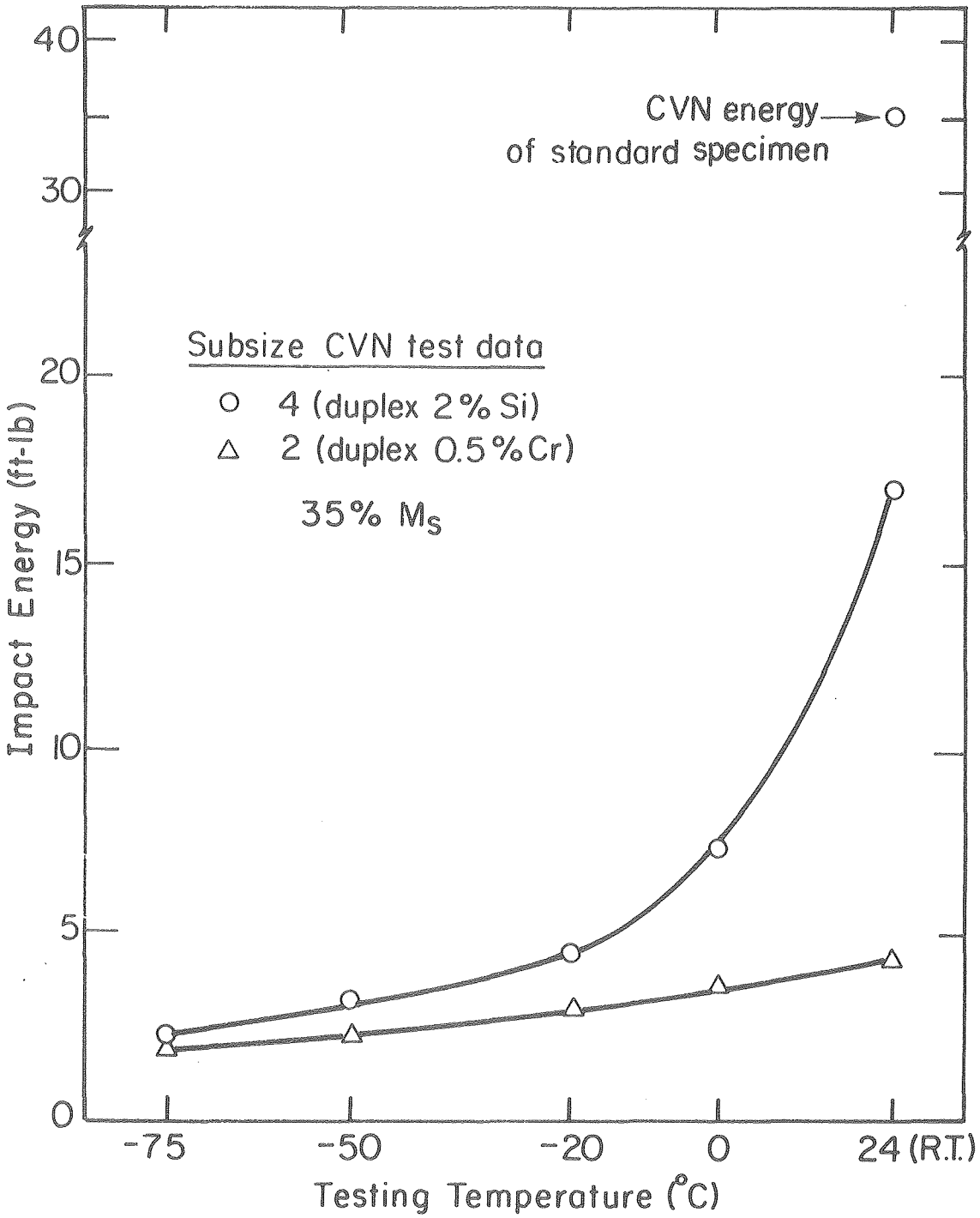

XBL 776-5564

Figure 45

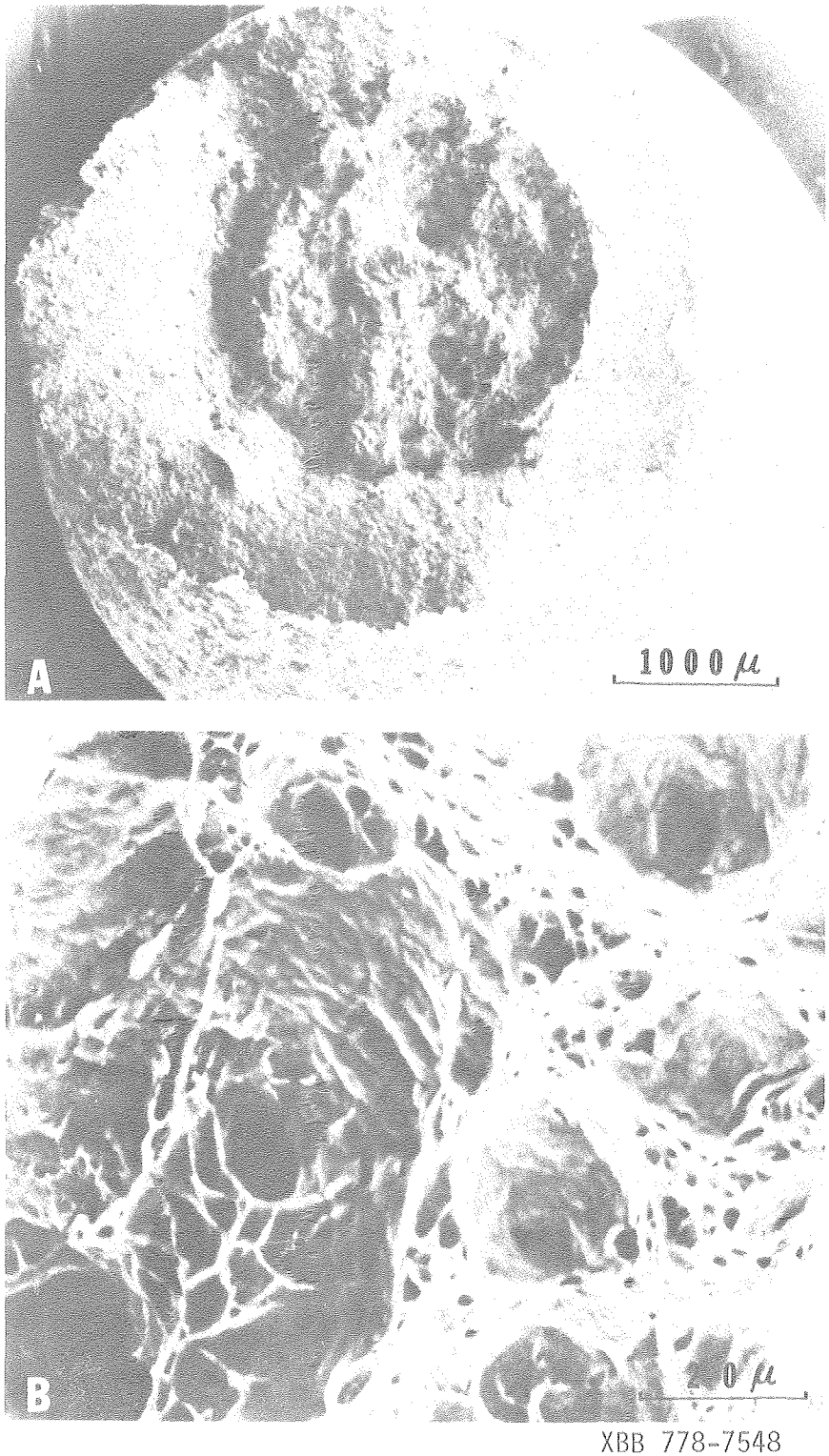

Figure 46

XBB 778-7532

Figure 46 (con't)

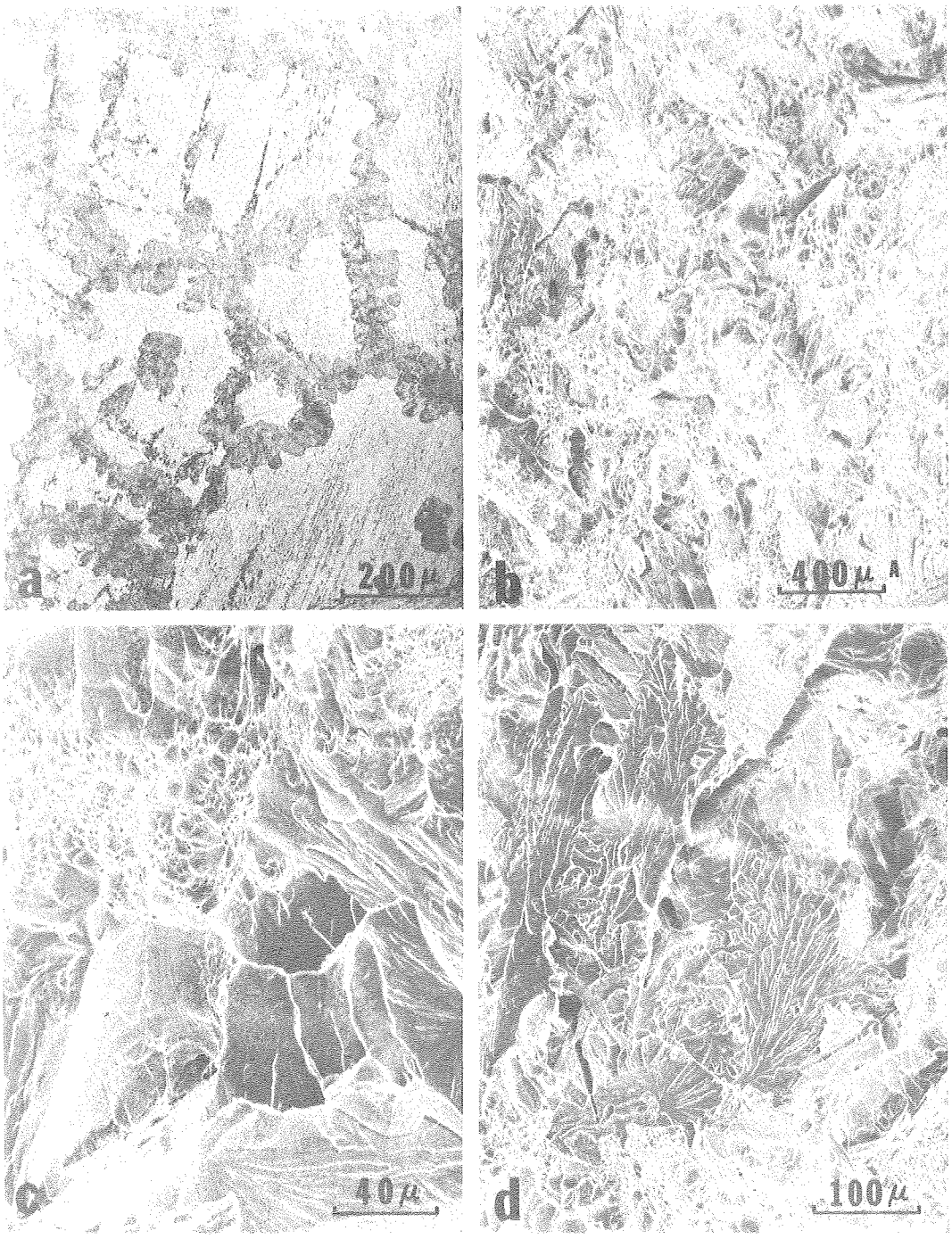

XBB 788-7553

Figure 47

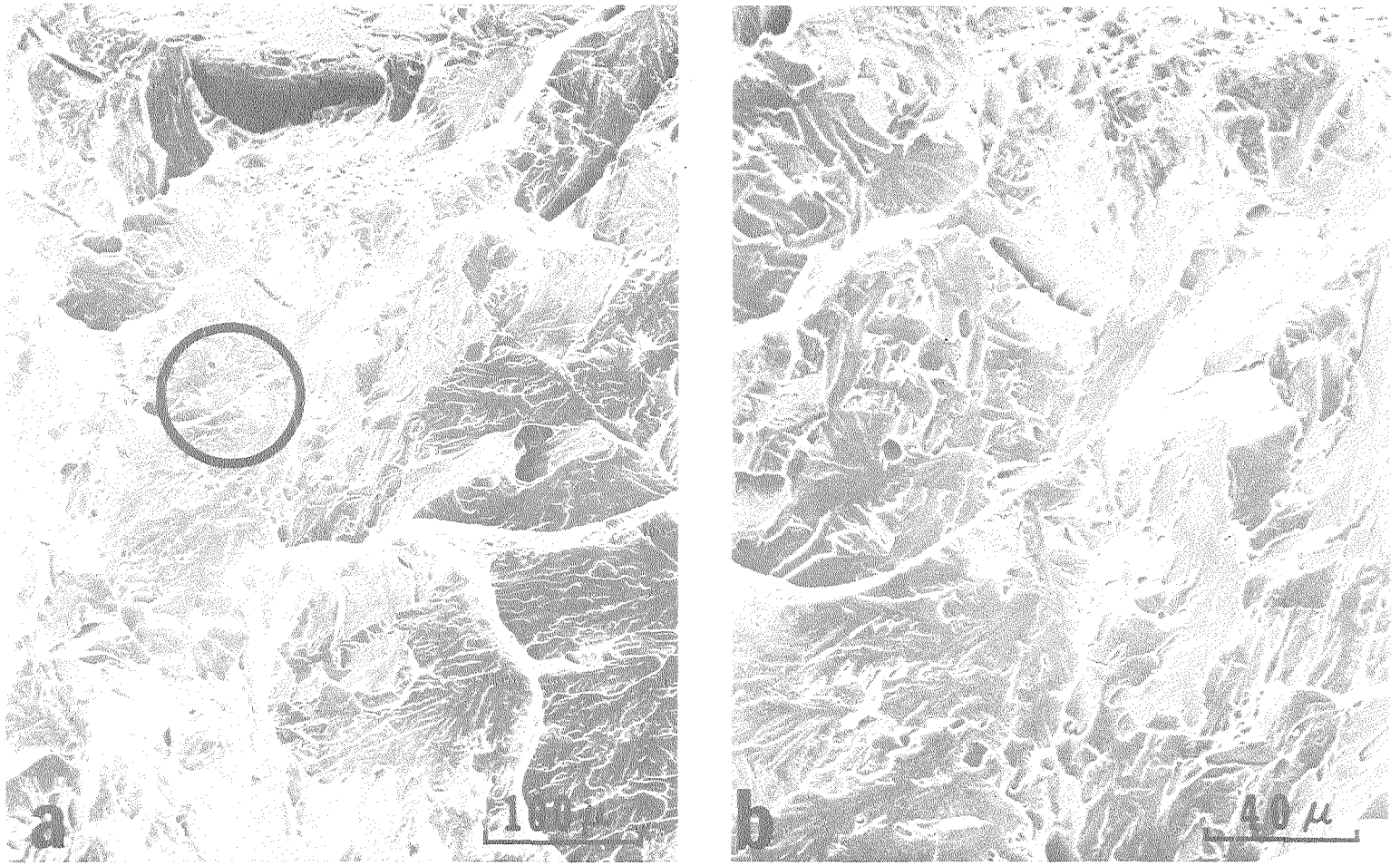

XBB 778-7530

Figure 48

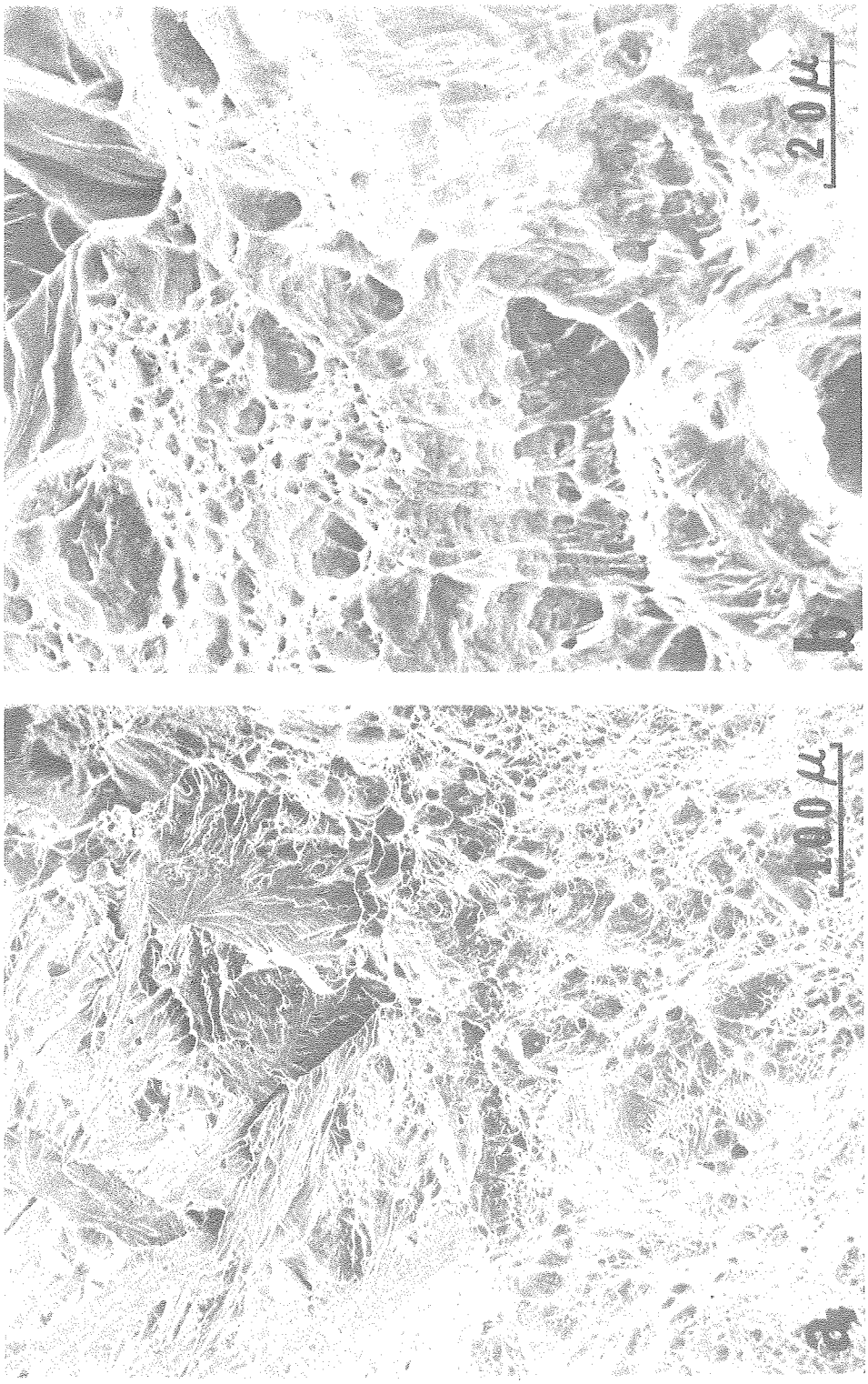

XBB 778-7533

Figure 49

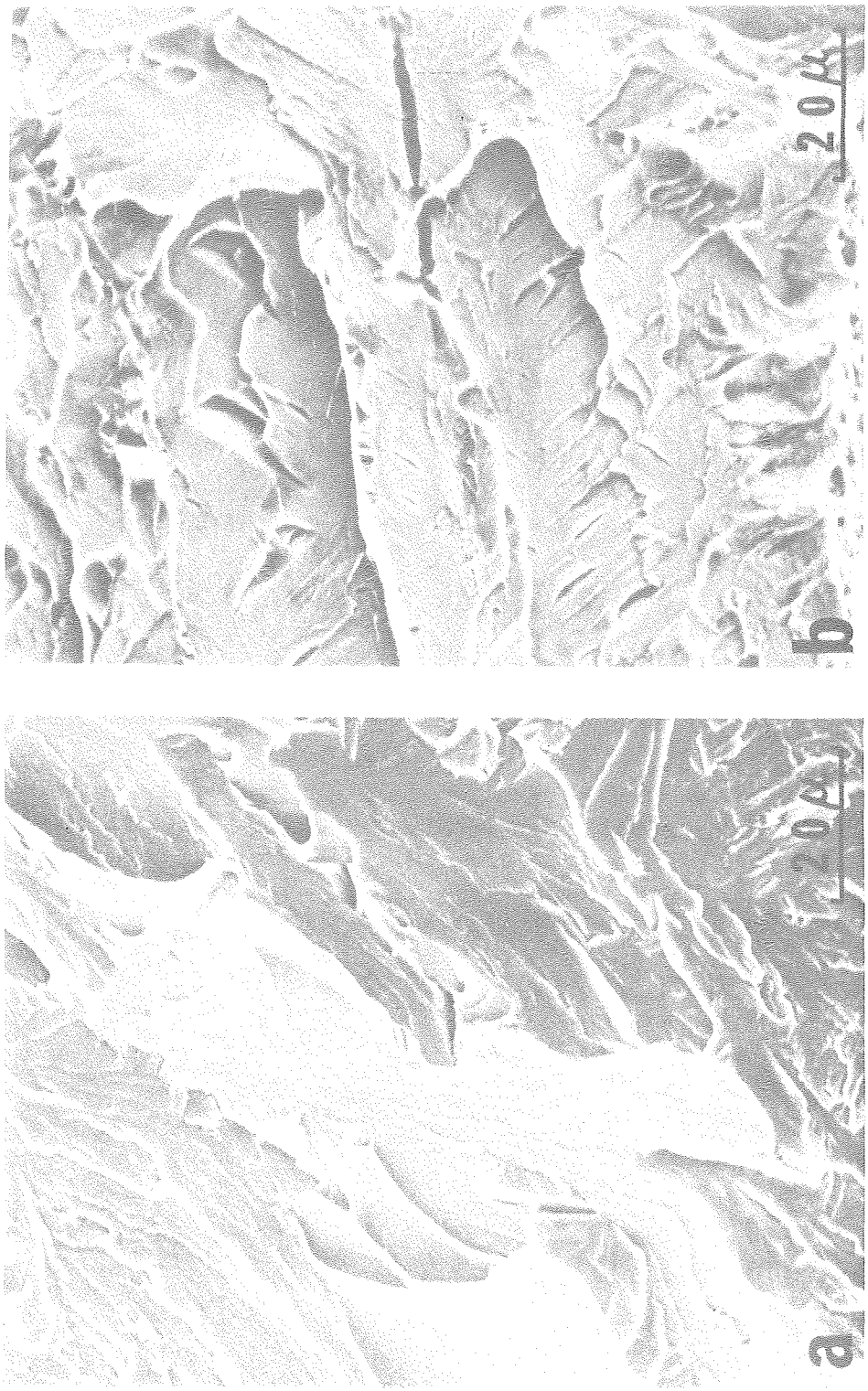

XBB 788-7534

Figure 50

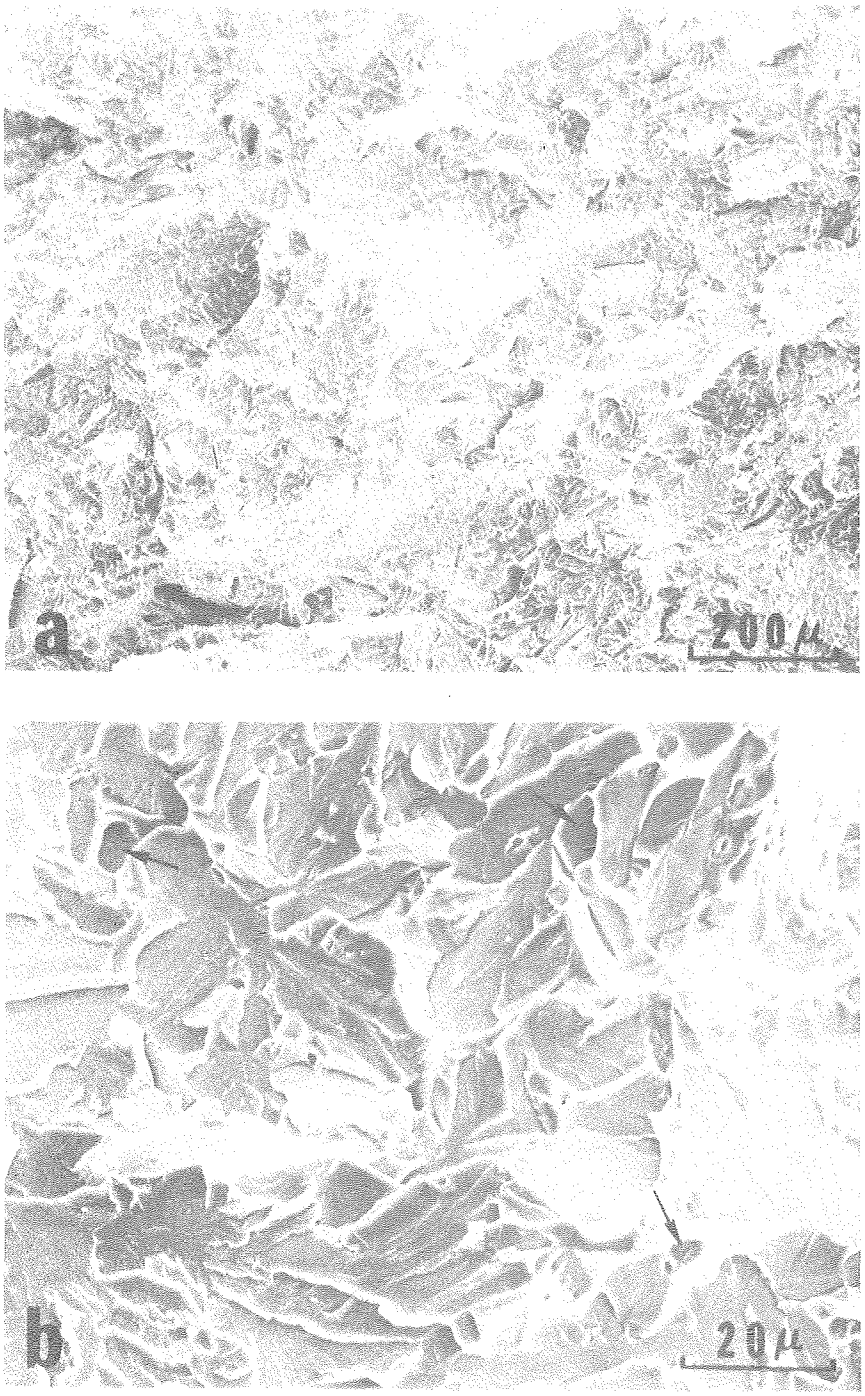

XBB 778-7554

Figure 51

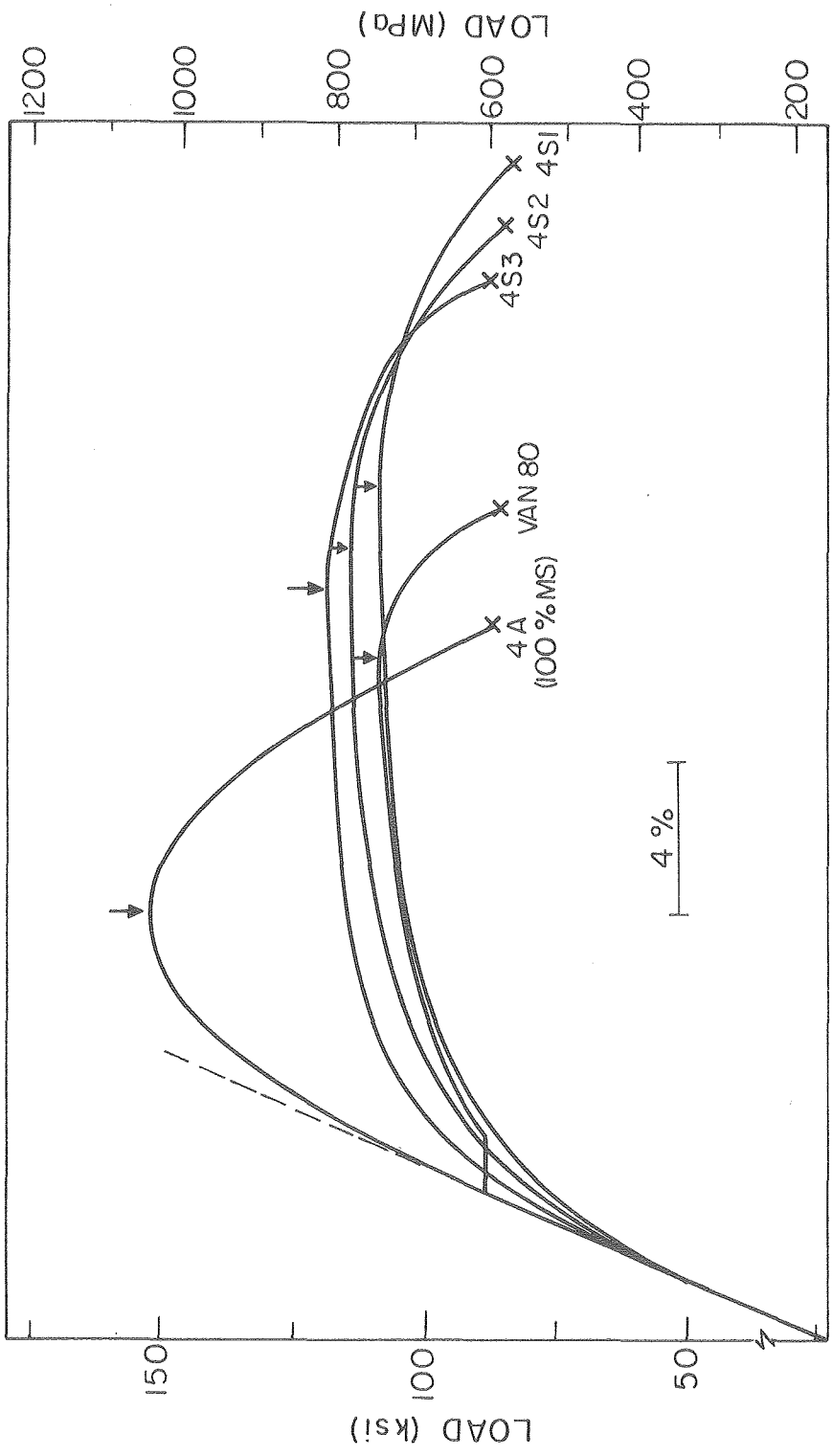

XBL 777-5865

Figure 52

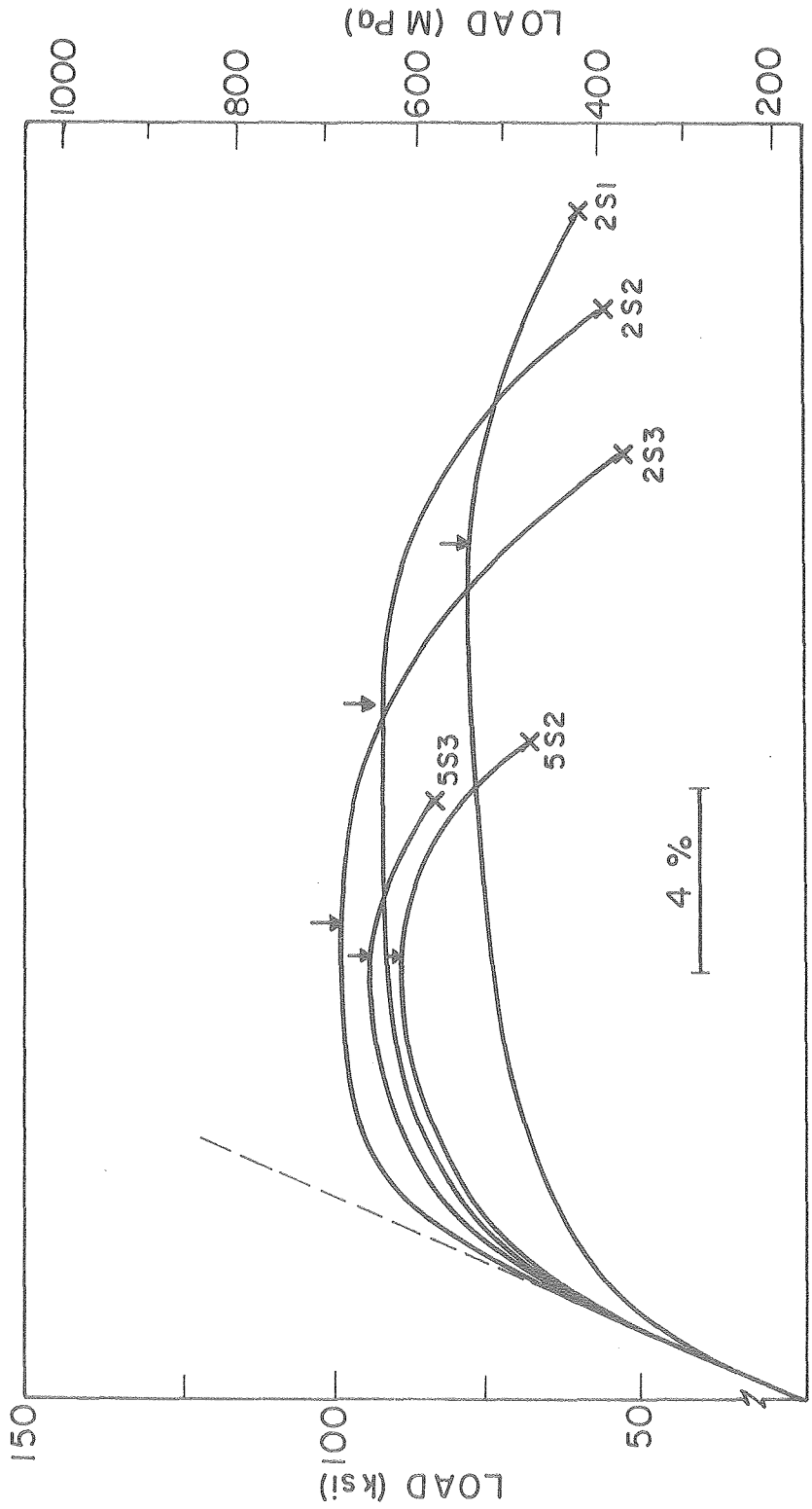

XBL 777-5866

Figure 53

Fe-RICH PORTION OF THE Fe-C PHASE DIAGRAM

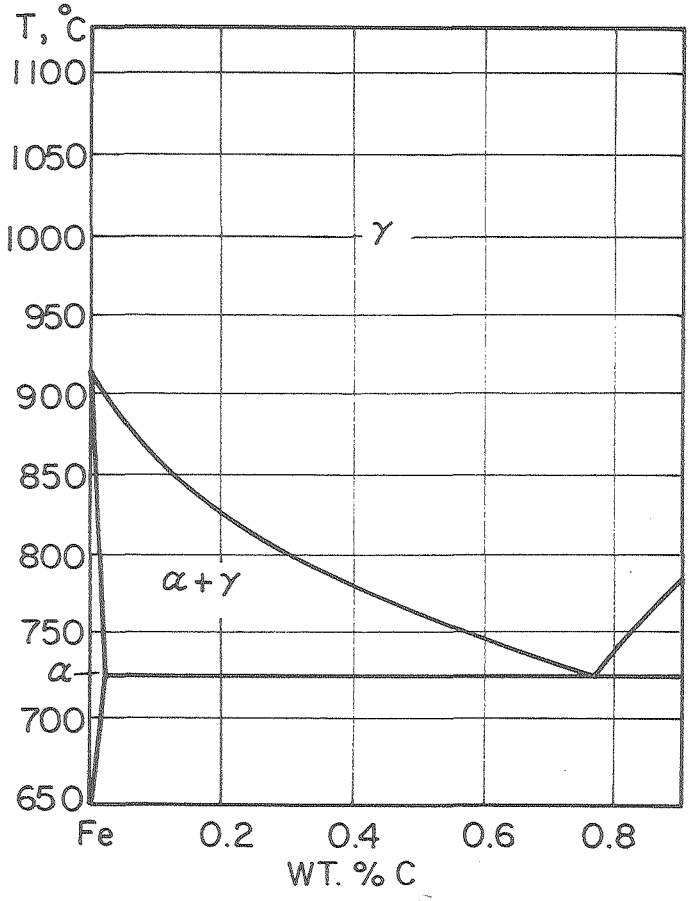

Fe-RICH PORTION OF THE 2.4 WT. % Si SECTION OF THE Fe-Si-C PHASE DIAGRAM

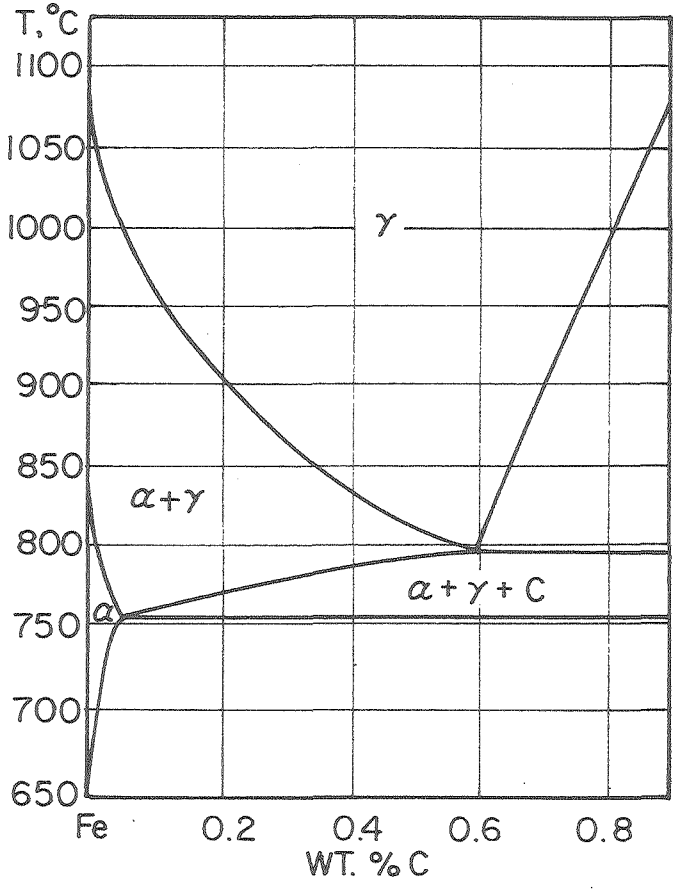

XBL 761-6344

Figure 54

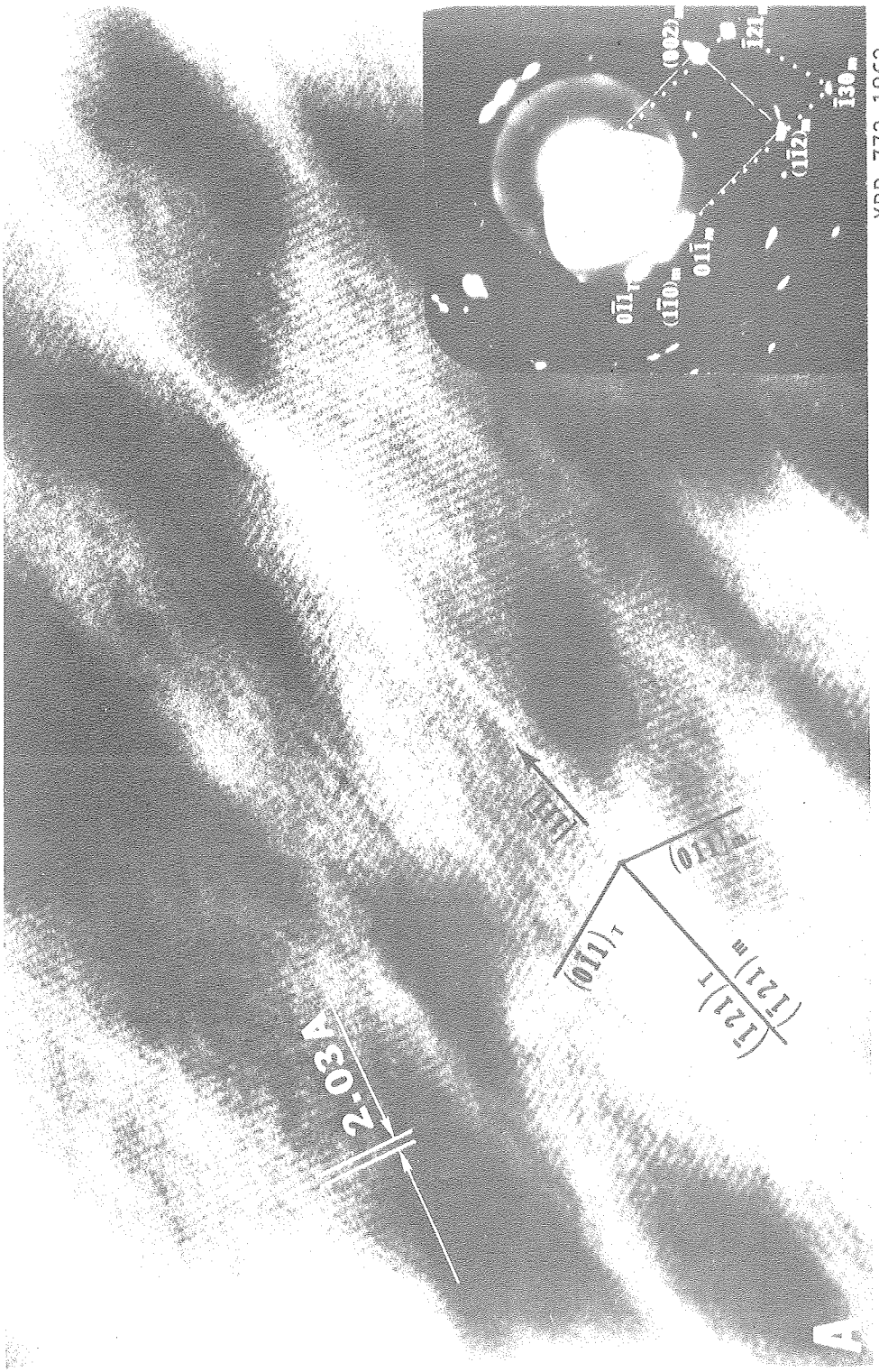
2.03Å
(011)T
(1̄21)T
(1̄21)T
(1̄10)T
(1̄11)T
(1̄10)
(011)
(112)
(002)
(1̄21)
(130)
XBB 773-1863

Figure 55 (a)

XBB 773-1867

Figure 55 (b)

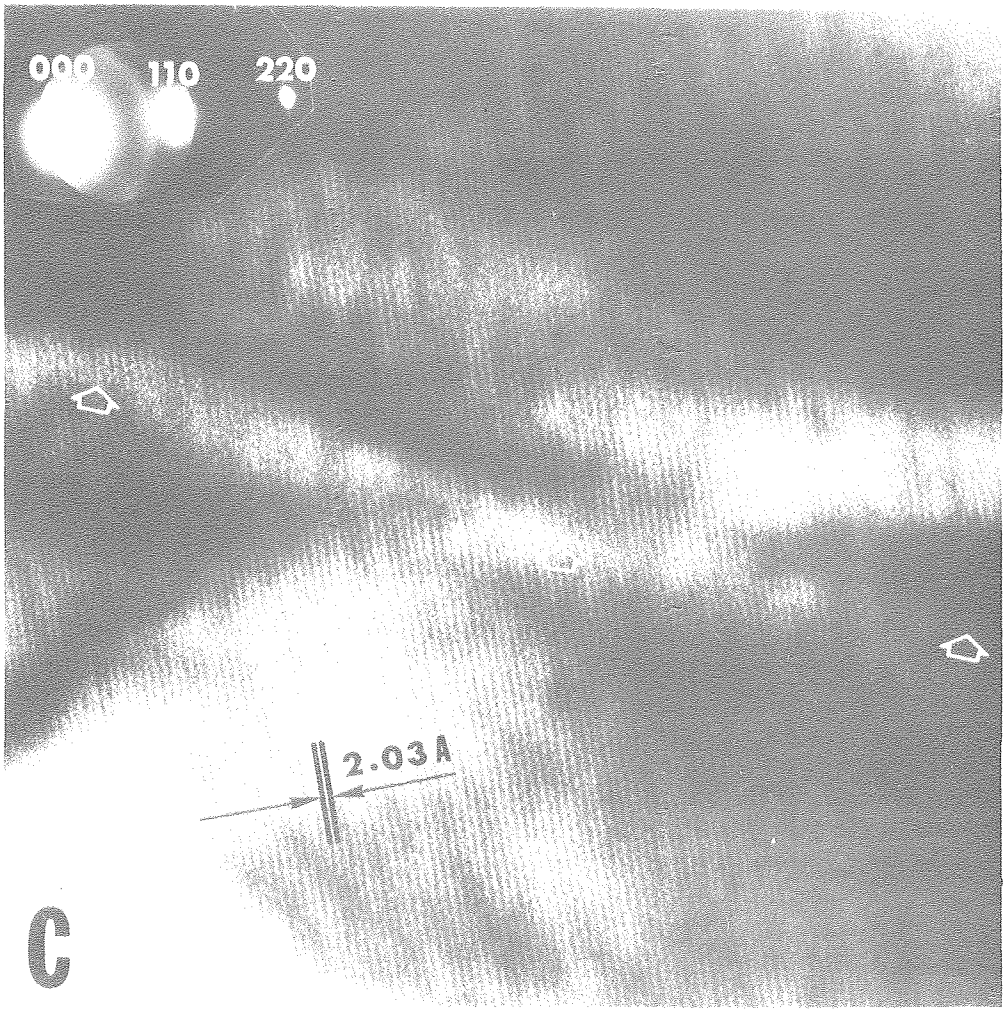

XBB 773-1864

Figure 55 (c)

XBB 778-7544

Figure 56

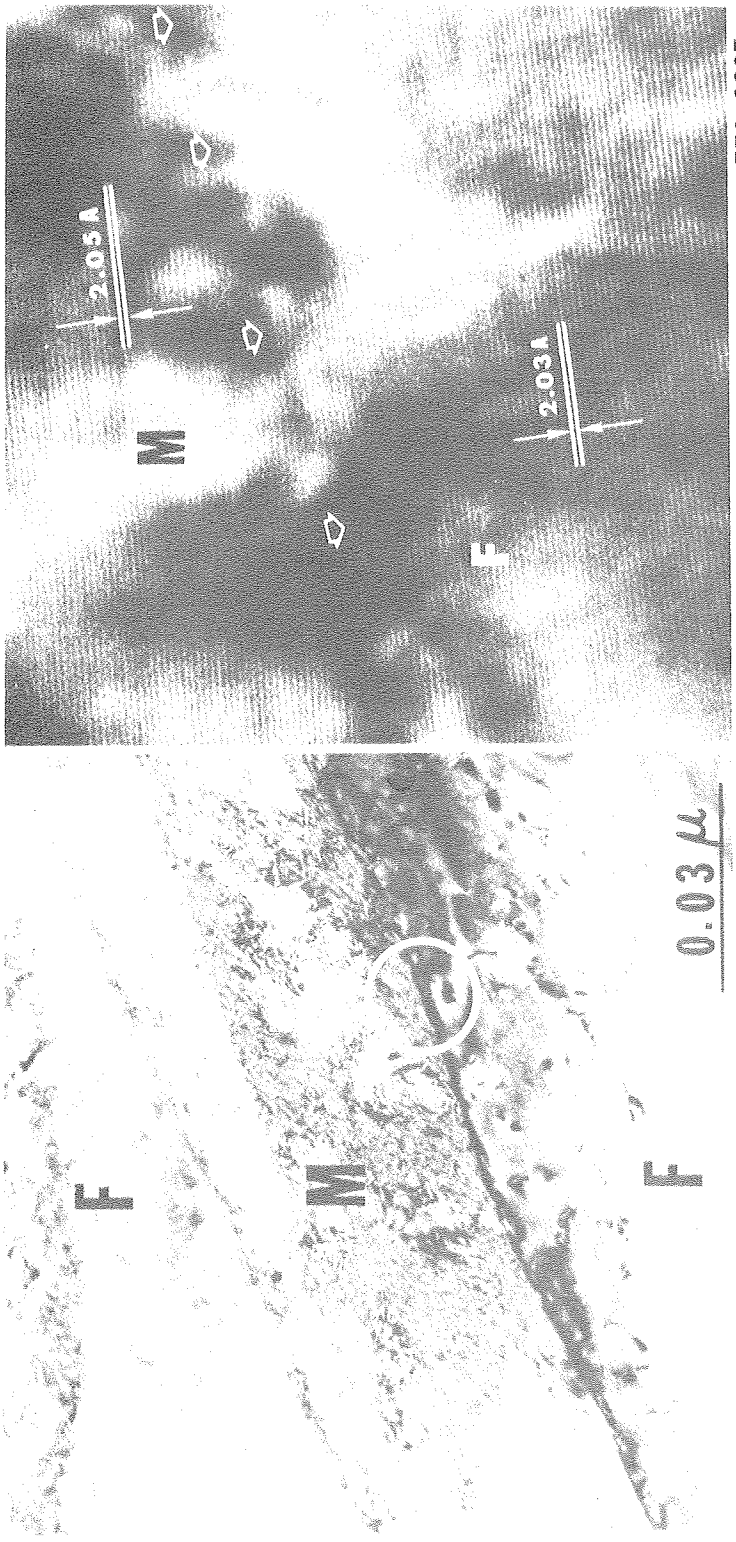

Figure 57

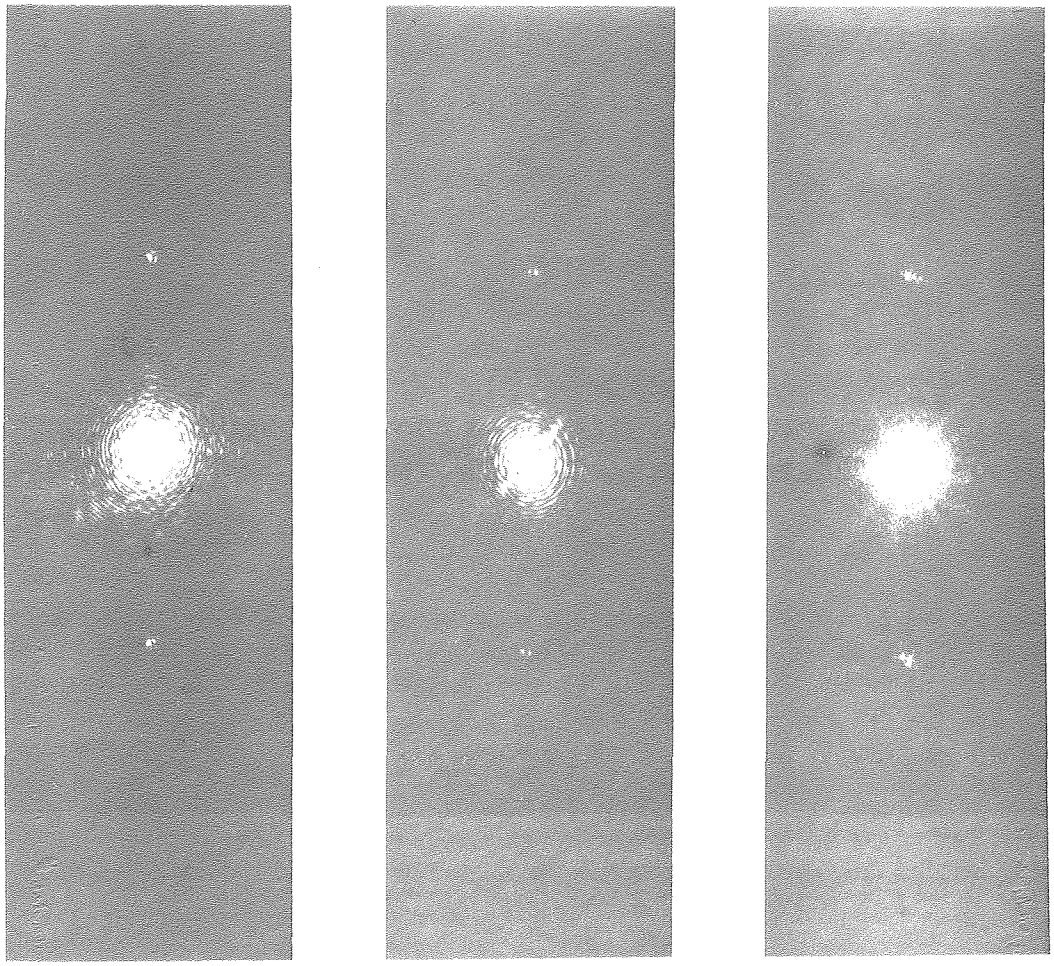

XBB 773-2298

Figure 58

This report was done with support from the United States Energy Research and Development Administration. Any conclusions or opinions expressed in this report represent solely those of the author(s) and not necessarily those of The Regents of the University of California, the Lawrence Berkeley Laboratory or the United States Energy Research and Development Administration.